SYNTHESIS AND CHARACTERIZATION OF LONG PERSISTENT PHOSPHORS USING COMBUSTION METHOD

by

Manaka Mmakgabo Colen

Submitted in accordance with the requirements

for the degree of

Magister Scientiae of Science

In the subject

Physics

at the

University of South Africa

Supervisor: Prof B.M Mothudi

Co-supervisor: Prof M.S Dhlamini

2015

DECLARATION

I Mmakgabo Colen Manaka declare that this work hereby submitted to the University of South Africa for the fulfilment of a master's degree in physics has not been previously submitted at the University of South Africa or any other University.

I also declare that the work contained in this thesis is my own except where references are duly made.

…… ……

Signature Date

(Mr. MC Manaka)

DEDICATION

This work is dedicated to my parents Lesiba Elias Manaka and Mokgaetji Johanna Manaka

ACKNOWLEDGEMENTS

- Above all, I forward my gratitude to my God, for all the strength he provided me throughout the duration of this work.
- I am very thankful for the exceptional supervision and support I got from my supervisor Prof B.M Mothudi. I also thank him for helping me arrange this work's chapters. If it was not of him, this work would not have been a success.
- My very thankful expression also goes to my co-supervisor Prof M.S Dhlamini for his suggestions in this work and in manuscripts. Most importantly, I would like to thank him for making it possible for me to be able to perform the XRD and SEM measurements at CSIR.
- I am very grateful to Unisa Student Funding for funding my studies.
- My thanks also go to all staff members of the Physics Department for their support and encouragements.
- I would like to also acknowledge all the suggestions that contributed to the success of this work from my fellow researchers.
- I also thank Prof Chithambo and his students for introducing me to the TL system and helping me with the TL measurements at the Rhodes University.
- I am very grateful for all the suggestions from Luyanda Noto from the University of The Free State on how to work with very small doping concentrations.
- I am very grateful to my parents, brothers and sisters for the encouragement and moral support they gave me throughout this work.

Summary

In this work, alkaline earth aluminate phosphors doped with rare-earth ions and manganese were synthesized using combustion method. Several characterization techniques were used to study the structural and luminescent properties of the as-synthesized phosphors, namely X-ray diffraction (XRD), Scanning Electron Microscopy (SEM), X-ray energy Dispersive Spectroscopy (EDS), Ultraviolet-Visible (UV-Vis) Spectroscopy, Photoluminescence (PL), and Thermoluminescence (TL). The structural properties were studied by collecting the XRD patterns of the samples using an X'Pert PRO PANalytical diffractometer with CuKα at λ = 0.15405 nm. The particle morphologies of the as-synthesized powder phosphors were investigated using a JEOL JSM-7500F field-emission scanning electron microscope (FE-SEM). The optical properties of the phosphors were studied using Perkin-Elmer Lambda 750s UV-Vis spectrometer, Jobin Yvon/SPEX FluoroLog spectrofluorometer (Model FL-1040) and Riso TL/OSL reader (Model DA-20).

The as-prepared $SrAl_2O_4:Eu^{2+}$; $SrAl_2O_4:Dy^{3+}$; $SrAl_2O_4:Mn^{2+}$; phosphors were synthesized at an initiating temperature of 600 ^oC. The XRD patterns were consistent with the low temperature monoclinic structure of $SrAl_2O_4$ for all the as-synthesized phosphor powders. SEM measurements showed nano-rod like particles. The $SrAl_2O_4:Eu^{2+}$; $SrAl_2O_4:Dy^{3+}$; $SrAl_2O_4:Mn^{2+}$ samples were excited using a 450 W Xenon light source at 364 nm, 390 nm, and 426 nm respectively. A broad blue emission peak at 500 nm shown by the $SrAl_2O_4:Eu^{2+}$ sample is attributed to the $4f^6 5d^1 \rightarrow 4f^7$ transition of the Eu^{2+} ion. Also, the red sharp emission lines due to the 4f-4f transition of the Eu^{3+} were observed.

$SrAl_2O_4:Dy^{3+}$ samples exhibited blue, green, and red emissions which can be atributed to the $^4F_{9/2} \rightarrow {}^6H_{15/2}$, $^4F_{9/2} \rightarrow {}^6H_{13/2}$, and $^4F_{9/2} \rightarrow {}^6H_{11/2}$ transitions of Dy^{3+} ions respectively. The two broad emissions (green at 513 nm and red at 650 nm) shown by $Sr_{0.98}Al_2O_4:Mn^{2+}{}_{0.02}$ sample can be atributed to the $^4T_1(^4G) \rightarrow {}^6A_1(^6S)$ transition of the Mn^{2+} ion in the sample.

The $SrAl_2O_4:Eu^{2+}$, Dy^{3+}; $SrAl_2O_4:Eu^{2+}$, Mn^{2+}; $SrAl_2O_4:Dy^{3+}$, Mn^{2+}; and $SrAl_2O_4:Eu^{2+},Mn^{2+}$, Dy^{3+} phosphors were synthesized by combustion method at an initiating temperature of 600 ^oC. The blue emissions were observed in all the samples except $SrAl_2O_4:Eu^{2+},Mn^{2+}$, Dy^{3+} sample. The $SrAl_2O_4:Eu^{2+},Mn^{2+}$, Dy^{3+} phosphor showed the longest afterglow intensity.

The $BaAl_2O_4$ doped with Eu^{2+}, Mn^{2+} and Dy^{3+} phosphors synthesized at an initiating temperature of 600 ^oC using combustion method. The XRD patterns confirmed the hexagonal structure of $BaAl_2O_4$ in all the as-synthesized samples. A broad blue emission of the $BaAl_2O_4:Eu^{2+}$ sample at 490 nm is attributed to the $4f^6 5d^1 \rightarrow 4f^7$ transition of the Eu^{2+} ion in the sample. A red emission peak observed at 611 nm is due to the 4f - 4f transition of un-reduced Eu^{3+} ions during the combustion reaction. A blue emission at 482 nm, a green emission at 575 nm, and a red emission at 663 nm of the $BaAl_2O_4:Dy^{3+}$ sample can be associated with $^4F_{9/2} \rightarrow {}^6H_{15/2}$, $^4F_{9/2} \rightarrow {}^6H_{13/2}$, and $^4F_{9/2} \rightarrow {}^6H_{11/2}$ transitions of the Dy^{3+} ions respectively. The green emission peaks exhibited by $BaAl_2O_4:Mn^{2+}$ sample at 512 nm is due to the $^4T_1(^4G) \rightarrow {}^6A_1(^6S)$ transitions of the Mn^{2+} ions.

Barium aluminate phosphors doped with different concentrations of Dy^{3+} ion were synthesized by combustion method at an initiating temperature of 600 ^oC. The XRD patterns confirmed the hexagonal structure of $BaAl_2O_4$. The emission peaks observed at 482 nm, 575 nm, and 663 nm are due to $^4F_{9/2} \rightarrow {}^6H_{15/2}$, $^4F_{9/2} \rightarrow {}^6H_{13/2}$ and $^4F_{9/2} \rightarrow {}^6H_{11/2}$ transitions of Dy^{3+} ion respectively. The PL measurements also confirmed the quenching of luminescence at higher concentrations of the Dy^{3+} ion. The UV-Vis measurements has confirmed the increase in the band-gap of the $BaAl_2O_4$ sample followed by a decrease and an increase again as doping concentration of the Dy^{3+} increased.

The X-ray diffraction patterns of the $Ca_{0.97}M_{0.3}Al_2O_4:Eu^{2+}$, Dy^{3+} (M = Ba, Mg, and Sr) powder samples prepared by combustion method confirms the monoclinic structure of $CaAl_2O_4$ in all samples. A broad emission peak at 490 nm for both Ba^{2+} and Mg^{2+} substituted samples and the

one for Sr^{2+} substituted sample at 485nm are attributed to the $4f^{6}5d^{1} \rightarrow 4f^{7}$ transition of the Eu^{2+}. The decay curves confirmed that the Mg^{2+} substituted sample has a longer persistence (phosphorescence) than all the other samples.

KEYWORDS

- Combustion Method
- Photoluminescence
- Phosphorescence
- Long-Afterglow
- Rare earth ions
- Alkaline Earth Aluminates

ACRONYMS

- XRD – X-Ray Diffraction
- SEM- Scanning Electron Microscopy
- UV-VIS- Ultraviolet-Visible
- PL – Photoluminescence
- TL-Thermoluminescence
- EDS – Energy Dispersive Spectroscopy

CONTENTS

LIST OF FIGURES

CHAPTER 1

Introduction

1.1. Overview

There are several semiconductor materials that exhibit an interesting phenomenon known as luminescence, which refers to the release of energy in the form of light. This process takes place after their electronic states have been disturbed by the energy of light of specific wavelength [1]. The type of luminescence exhibited by these semiconductor materials is usually named according to the form of energy used to disturb (excite) their electronic states prior to the exhibition of luminescence. These types of luminescence are discussed in detail in Chapter 2.

In this study our main focus will be on specific semiconductor materials called phosphors. It is mainly made up of a host matrix and impurities that act as activators [2]. A phosphor typically absorbs energy from one part of the electromagnetic spectrum and converts it to another part of the spectrum, and this type of absorption can be attributed to impurities intentionally incorporated into the matrix and the defects induced during the synthesis process.

An example of such a phosphor is $CaAl_2O_4:Eu^{3+}$, Na^{+} material that absorbs in the UV region and emit in the visible region of the electromagnetic spectrum [3]. When a phosphor is irradiated with UV light, some of the electrons from lower energy states will be excited into higher energy states. When these electrons relax back to the lower energy states, energy in the form of light is released as fluorescence or phosphorescence. Phosphorescence persists for a longer time and materials that exhibit this type of luminescence have been used in various applications such as signage in watches, emergency signs, displays in the dark and so on [4].

In addition, the long persistent blue and red emitting nanophosphors have been used for greenhouse application. In this application, the red and the blue nanophosphors are incorporated in thin films to absorb ultraviolet and green light from the sun and convert it into blue and red

light. Both blue and red colours are efficiently absorbed by chlorophyll in plants and this will speed-up the growth for plants [5].

The commercially available green emitting phosphors such as $SrAl_2O_4:Eu^{2+}$, Dy^{3+} and a blue emitting $CaAl_2O_4:Eu^{2+}$, Nd^{3+} phosphors are some examples of the long persistent phosphors [6].The Eu^{2+} ions present in these phosphors will act as the luminescent centers and the Dy^{3+} ions will create hole traps, which are responsible for the prolonged duration of phosphorescence. The Phosphorescence mechanism will be discussed in detail in Chapter 2. These are aluminate phosphors, and are preferred by many researchers over sulphide based phosphors such as ZnS owing to the interesting features such as high brightness, chemical stability, and they do not pose danger to the environment [7]. Due to these interesting properties i.e. structural, electronic, and optical properties of crystalline materials at nanoscale, various synthesis techniques such as solid state reaction, sol-gel, co-precipitation method and many more have been developed and used to synthesize nanomaterials. In this study, the combustion method was used to synthesize alkaline earth aluminate phosphors.

1.2. Statement of the problem

In recent years, several materials have been studied for practical applications such as light emitting devices, display devices etc. Display devices play a significant role in improving the communication of information [8]. For instance, in electronic devices such as TV sets and computers, the information is stored in tapes and chips, and this information cannot be seen by naked eye on these storage devices. Now to access information stored on these devices, a display device is deployed and acts as an interface between electronic devices and the human [8]. After the invention of cathode ray tubes (CRTs) by Karl Ferdinand Braun in 1897 [8], which became a typical display devices, the development of Flat Display Panels (FDPs) started due to an inevitable drawback that the CRTs exhibit smeared images [8]. However, phosphors such as ZnS:Ag:Cl, ZnS:Cu:Al, $Y_2O_2S:Eu$, etc. [8], were ideal in fabrication of phosphor screens due to their high brightness intensity. However, these types of materials show chemical instability and their luminescence intensity tend to decrease in the presence of oxygen [9].

Rare earth doped alkaline earth aluminates such as $SrAl_2O_4:Eu^{2+},Dy^{3+}$ and $CaAl_2O_4:Eu^{2+},Nd^{3+}$ are well known for their interesting properties such as long persistent luminescence, high brightness, environmental friendliness, and chemical stability [10,11], which makes these types of materials the best substitutes for sulphide based phosphors for the abovementioned practical applications. Structural, morphological, and optical properties of various rare earth doped alkaline earth aluminate phosphors will be investigated. Photoluminescence and thermoluminescence studies will be carried in order to understand the role dopants and co-dopants in the host nanocrystals. Several parameters such as concentration of the dopants and impurity phases will be investigated on how they influence band gap of the host structure.

1.3. Aims and objectives of the study

i. To study the structural and luminescent properties of rare earth ion and manganese doped alkaline earth aluminate powder phosphors synthesized by combustion method.
ii. To study the role of Mn^{2+} ion on the afterglow of $SrAl_2O_4:Eu^{2+}$, Mn^{2+}; $SrAl_2O_4:Mn^{2+}$, Dy^{3+}; and $SrAl_2O_4:Eu^{2+}$, Mn^{2+}, Dy^{3+} powder phosphors.
iii. To investigate the influence of the host matrices on the luminescent properties of Eu^{2+}, Eu^{3+}, Dy^{3+}, and Mn^{2+} doped alkaline earth aluminates.
iv. To study the luminescent properties of properties of $BaAl_2O_4$ phosphor powder doped with different concentration of Dy^{3+}.
v. To investigate the role of lattice distortion on the luminescent properties of the $(Ca_{(1-x)}M_{0.3})_{0.97}Al_2O_4:Eu^{2+}{}_{0.01},Dy^{3+}{}_{0.02}$ (M = Ba^{2+}, Mg^{2+}, and Sr^{2+}) powder phosphors.

1.4. Layout

Chapter 1 briefly outlines the aims and objectives of this study

Chapter 2 presents brief background information on the luminescence properties of Eu^{2+}, Mn^{2+}, Eu^{3+} and Dy^{3+} doped alkaline earth aluminates. Comprehensive information on energy transfer from a donor ion to an acceptor ion is also presented in this chapter.

Chapter 3 summarizes all techniques i.e. synthesis and characterization techniques used in this work.

Chapter 4 provides a detailed discussion of photoluminescence properties of Eu^{2+}; Dy^{3+} and Mn^{2+} ions in $SrAl_2O_4$ phosphors prepared by combustion method. The effect of co-doping these ions on their luminescence properties is discussed in details in this chapter.

Chapter 5 presents photoluminescence properties of Eu^{2+}; Dy^{3+} and Mn^{2+} ions in $BaAl_2O_4$ phosphors prepared by combustion method.

The effects of Dy^{3+} concentration on the photoluminescence properties of $SrAl_2O_4$: Dy^{3+} phosphor are discussed in Chapter 6.

A detailed discussion about the photoluminescence properties and the distortion of the $CaAl_2O_4$:Eu^{2+}, Dy^{3+} host matrix when the Ca^{2+} ions are being replaced by Ba^{2+}, Mg^{2+}, and Sr^{2+} is given in Chapter 7.

Chapter 8 is about the summary of the dissertation, conclusions and possible future studies.

References

1. R. Holze, Surface and Interface Analysis: An Electrochemists Toolbox, Springer, Heidelburg, 2008, pp 47
2. Phosphor Handbook: Second Edition, W. M. Yen, S. Shionoya, H. Yamamoto, CRC Press, USA, 2007, pp 4
3. R. J. Wiglusz, T. Grzyb, A. Lukowiak, A. Bednarkiewicz, S. Lis, W. Strek, *J. Lumin.* **133** (2013) 102-109
4. U. Happek, S. Okamoto, J. Collins, B. Di Bartolo, K. C. Mishra, X. J. Wang, H. Yamamoto, Physics and Chemistry of Luminescent Materials, including the 4th Symposium on Persistent Phosphors, The Electrochemical Society, 2009, pp 25
5. J. Weidner, Persistent Phosphors 3, The Electrochemical Society, New Jersey, 2008, pp 19
6. U. Happek, S. Okamoto, J. Collins, B. Di Bartolo, K. C. Mishra, X. J. Wang, H. Yamamoto, Physics and Chemistry of Luminescent Materials, including the 4^{th} Symposium on Persistent Phosphors, The Electronic Society, USA, 2009, pp 25
7. W. M. Yen, S. Shionoya, H. Yamamoto, Practical Applications of Phosphors, CRC Press, USA, 2010, pp 470
8. L. Ozawa, Cathodoluminescence and Photoluminescence: theory and practical Applications, CRC Press, 2010, pp 1-4
9. B. M. Mothudi, PhD Dissertation, University of the Free State, South Africa, 2009.
10. X. Li, Y. Qu, X. Xie, Z. Wang, R. Li, *Matt. Lett.* **60** (2006) 3673–3677
11. W. Jia, H. Yuan, L. Lu, H. Liu, W. M. Yen, *J. Cryst. Growth.* **200** (1999) 179-184

CHAPTER 2

Luminescence Properties of Phosphors

2.1. Background of Phosphors

Phosphor is a Greek word, which means light bearer and it is a common term which refers to the light emitting materials [1]. Generally, these materials absorb photons of a particular energy and emit photons with a different energy [2]. Phosphors can be classified into two groups depending on how they convert one type of energy into another. The first group is the up-conversion phosphors, which absorb the low energy wavelength and convert it to a higher energy wavelength [3]. An example of such conversion occurs when a phosphor absorbs the energy in the near-infrared region and later emits it in the visible region of the spectrum [3]. The second group is the down-conversion phosphors, which absorbs the energy at higher energy wavelength and emits at lower energy wavelength [3].

Phosphors are primarily inorganic materials, mostly with white body colour and consist of crystalline host matrices in which small amounts of certain impurities are intentionally incorporated [4]. In order to avoid concentration quenching, these impurities (activators) are usually introduced into crystalline host matrix at very low concentrations. [5].In most cases, at very high concentrations, a certain proportion of activators tend to aggregate and change from activators to killers and quench the luminescence [6]. These intentionally incorporated impurities are of two types namely; activators and co-activators.

The activators are usually responsible for the observed luminescence and the co-activators in phosphors are usually introduced when absorption of excitation energy by activators is too weak.

When this is the case, the incorporation of co-activators (donors) into a phosphor matrix efficiently absorbs the excitation energy and later transfers that energy to the activators (acceptors) and enhances the luminescence of the activator [7]. The mechanism of energy transfer from co-activators to activators can be explained using the Foster theory, also known as the fluorescence resonance energy transfer (FRET) depicted in Figure 2.1.

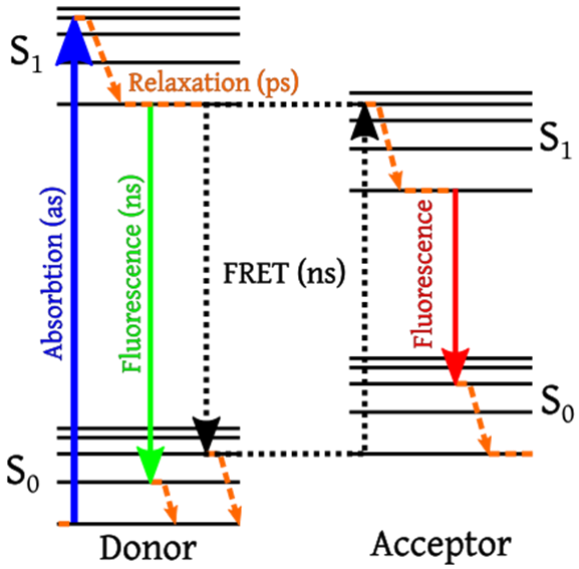

Figure 2.1: Schematic representation of the fluorescence energy transfer between a co-activator and activator ions [8].

When a phosphor containing both the activator and the co-activator is excited, a co-activator absorbs energy and later undergo internal conversion to reach the vibrational ground level of the first excited state [9]. If there is an overlap between the emission spectrum of the co-activator and the excitation spectrum of the activator, then efficient energy transfer from the co-activator to the activator will occur, and as a result enhancing the luminescence of the activator [9].

Phosphor materials can be excited by an external source of energy such as the ultraviolet light. Generally, the absorption of such energy may take place either on the host lattice or on the impurities (activator ions) [2]. When the incident energy is greater than the band-gap energy (E_g) of the host matrix, absorption of this energy by the host is possible. If there are impurity ions in the lattice, the energy absorbed can be transferred to the impurity ions and this process is known as indirect excitation or sensitization [10, 11]. On the other hand, if the incident energy is less

than the energy of the band-gap of the host matrix, then the host matrix is transparent to the incident energy, i.e. does not absorb this incident energy. The impurity ions in the host matrix can however absorb this energy, and the process will be referred to as direct excitation [10, 11]. Mostly by choosing an appropriate activator ion, one may vary the emission colours without changing the host matrix in which the impurity ions are incorporated [2].There are several methods that can be used to synthesize phosphors, e.g. solid state method, combustion method, sol-gel method etc. In most cases during these synthesis processes, some imperfections/(defects) tend to form in the crystal lattice of a phosphor. Some of these imperfections are intrinsic and inevitable, and some are extrinsic.

2.2. Intrinsic Defects

In a crystalline solid, a regular repetition of atoms exists throughout the lattice. A disturbance of this regularity creates defects known as intrinsic or native defects [12]. There are different types of intrinsic defects that may occur in the lattice.

2.2.1. Point Defects

During crystallization, packing of atoms might not be perfect and this may result in the defects known as point defects [12]. Vibrations of atoms at higher temperatures may also lead to these types of defects/(imperfections). Various types of point defects that occur in a crystalline solid are discussed below.

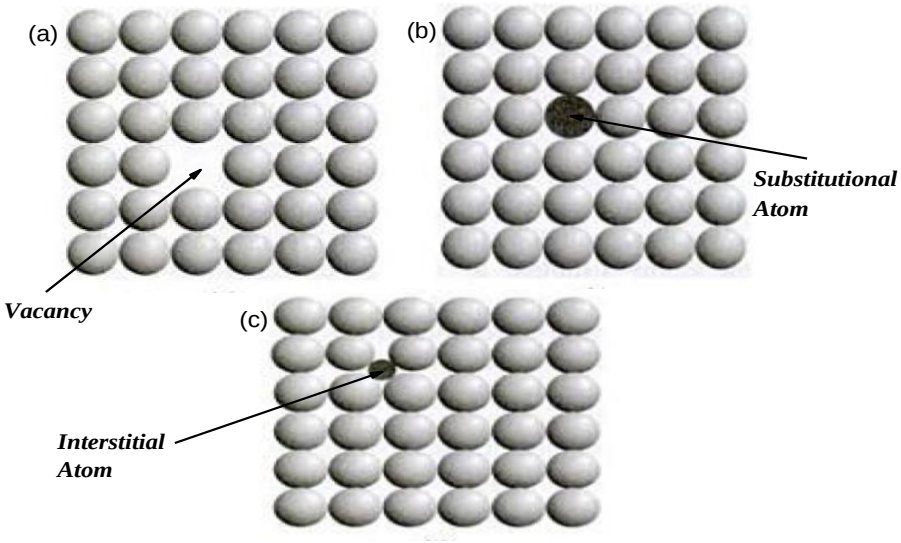

Figure 2.2: Images illustrating a vacancy (a), a substitutional atom (b), and an interstitial atom (c) in a crystalline solid [12].

Figure 2.2 shows the vacancy, substitutional, and interstitial types of point defects respectively. The vacancy shown on Figure 2.2(a) is formed due to the absence of one or more atoms from their normal positions [12]. The absence of a single atom from its normal position will lead to the formation of a single vacancy and di-vacancies form due to the absence of two atoms from their normal positions and so on [13].

Another type of point defects may occur when the impurity atom resides in a place that was supposed to be filled up by a parent atom as depicted in figure 2.2(b), and it is known as substitutional defects [12]. In this case, the impurity atom does not necessarily have to be of the same size as the parent atom i.e. the impurity atom may be bigger, or smaller in size compared to the parent atom [12]. Figure 2.2(c) also shows another type of defects, where an extra atom occupies the interstitial sites in the crystal, and this may lead to the formation of defects commonly known as interstitial defects [12].

Point defects do not have to be single. In other words a complex of two or more point defects merged together in a lattice is also possible, and these types of point defects are referred to as a cluster defects [14]. For example three vacancies can combine to form a tri-vacancy cluster defect, two interstitials can join to form di-interstitial cluster, and a vacancy can combine with an interstitial to form a vacancy-interstitial pair [14].

2.2.2. Linear Defects

Linear defects usually occur due to the structural disturbance of a crystal lattice expected to be of one dimension [13]. These types of defects may be created during crystal growth or as a result of mechanical deformation. There are two types of linear defects, disclinations and dislocations. Disclinations take place when the line defect is due to rotational displacements [13]. In this type of defect, rotation symmetry is violated. These are line defects associated with translational displacement of atoms. These are the more common line defects. There are two types of dislocations; namely edge dislocation and screw dislocation. Edge dislocation is a type of dislocation that is created when an extra part of a plane is introduced in the crystal, as illustrated in Figure 2.3 [15].

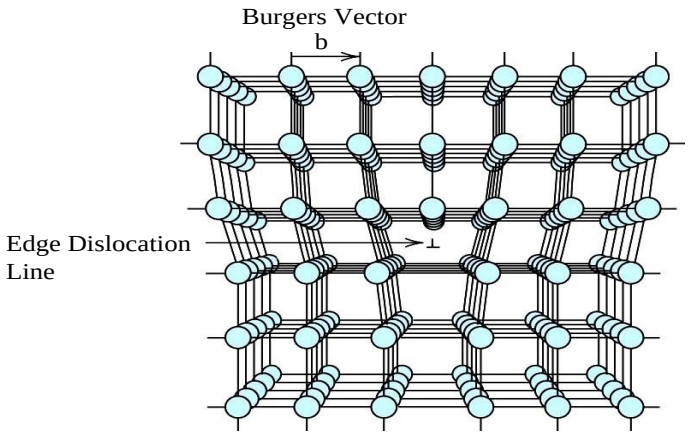

Figure 2.3: Edge dislocation in crystalline solid [16].

Screw dislocation is a type of dislocation in which the Burgers's vector is parallel to the dislocation line as depicted in figure 2.4. Application of shear stress on two sides of the crystal can result in screw dislocation [17].

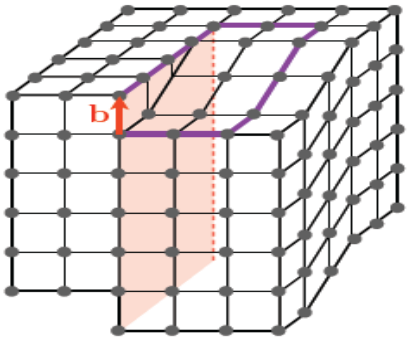

Figure 2.4: The screw dislocation in a crystal with Burgers Vector (b), dislocation line (dashed line), and slip plane (shaded area) [18].

2.3. Extrinsic Defects

Extrinsic defects in a crystal lattice are also possible. These are types of defects that can be introduced either intentionally or unintentionally. Intentionally these defects may be introduced through doping or ion implantation [14]. Usually, impurities are deliberately incorporated into the semiconductors in order to improve their physical, electrical, and optical properties [13]. These imperfections create localized energy levels within the band gap of the semiconductor materials and physical properties of semiconductors such as optical absorption, luminescence, electric conductivity and many more are related to both these levels and the band gap of the semiconductor materials [19]. The band-gap of various materials will be discussed in detail in the next section. Two types of band gaps for semiconductor materials are discussed below.

2.4. The Band-gap of a material

The band-gap of a semiconductor or an insulator is the energy difference between the maximum valence band and the minimum conduction band of the material. It is through these bands that a phosphor gives out energy as luminescence which will be discussed in details in the next section. The band-gap of a semiconductor can be narrow or wide [20]. The band-gap of a semiconductor can be either direct or indirect [21]. A direct band-gap semiconductor such as gallium arsenide is the one in which the lowest energy of the conduction band occurs at the same value of the wave vector K as the highest energy of the valence band [22], this phenomenon is clearly illustrated in Figure 2.5.

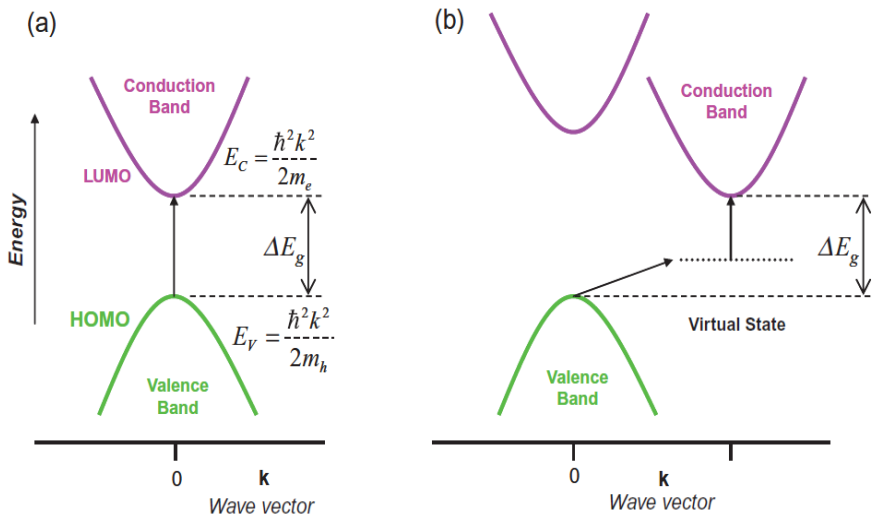

Figure 2.5: A diagram showing a direct band gap semiconductor (a) and an indirect band gap (b) semiconductor [22].

This suggests that only a photon of energy $\boldsymbol{E_c - E_v = \Delta E_g}$ is required in order for an electron to be excited from valence band $\boldsymbol{E_v}$ to conduction band E_c. When an electron falls back to its ground state, a photon with energy $\Delta\mathbf{E_g}$ will be emitted [23]. An indirect band gap semiconductor material such as silicon is the one in which the K value corresponding to the

highest energy of the valence band is different from that of the lowest energy of the conduction band [22] as shown in Figure 2.5(b).

In the indirect band-gap semiconductor, the excitation of the electron from the valence band to the conduction band requires not only the absorption of a photon, but also the absorption of a phonon, and because of this, the generation and recombination of charge carriers are less probable [23].

2.5. Luminescence

Luminescence is the emission of light from materials such as phosphors. This phenomenon occurs when electrons from higher energy states recombine with the holes in the lower energy states in a material, after being excited [24]. The energy of the emitted luminescence is lower than that of the excitation wavelength, which complies with Stokes's law, [25]. There are several ways of exciting a luminescent material and the types of luminescence are named based on the source of excitation as shown in table 2.1. However, only photoluminescence (fluorescence and phosphorescence) and thermoluminescence are discussed in this study.

Table 2.1: Different types of luminescence and their methods of excitation [26]

Method of excitation	Types of luminescence
Photons	Photoluminescence
Electric Field	Electroluminescence
Chemical energy	Chemiluminescence
Electrons	Cathodoluminescence
Sound Waves	Sonoluminescence
Higher Energy Particles	Radioluminescence
Mechanical Energy	Triboluminescence
Biochemical Energy	Bioluminescence
Photons	Thermoluminescence

2.5.1. Fluorescence

Fluorescence is the emission of a photon by a molecule when it relaxes from the lowest vibrational level of its excited singlet state to the highest vibrational level of its ground state [27]. Usually, a molecule absorbs a photon and goes to the highest vibrational levels of the excited singlet state as shown in figure 2.6. It then relaxes back to the lowest vibration level of this state. A subsequent relaxation to the highest vibrational level of the ground state emits a photon with energy lower than that of the absorbed photon [10]

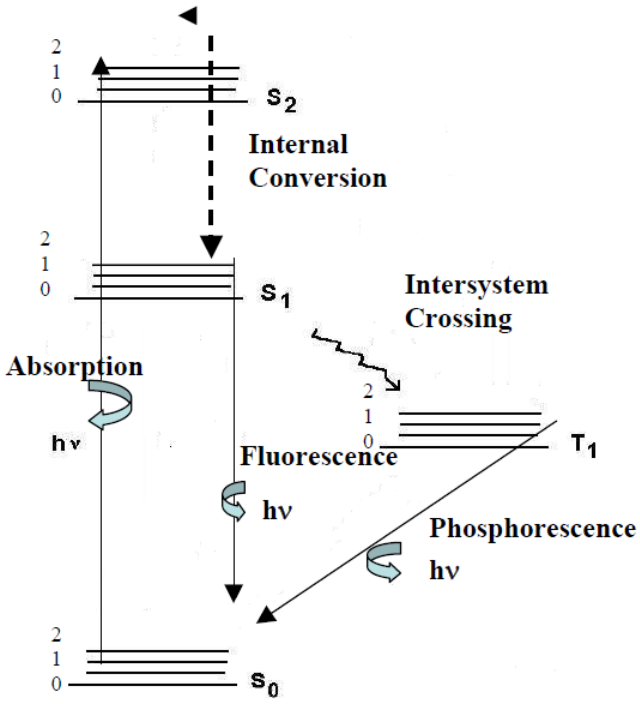

Figure 2.6: Jablonski Diagram showing Fluorescence and Phosphorescence Processes in a phosphor material [28].

2.5.2. Phosphorescence

Phosphorescence is then a delayed emission of light by a molecule, which results from the electronic transition from the lowest triplet state of the molecule to the ground state. The molecule absorbs a photon and goes to the highest vibrational levels of the excited singlet state as shown in Figure 2.6. Its relaxation to the lowest vibrational level of this state is followed by intersystem crossing to the triplet state as shown in Figure 2.6 [10]. The subsequent relaxation from lowest vibrational level of the lowest triplet state to the highest vibrational level of the ground state gives out a photon with energy lower than the absorbed one referred to as phosphorescence [10].

2.5.3. Thermoluminescence (TL)

Thermoluminescence is a type of luminescence in which an emission of visible light from a semiconductor or insulator is perceived when it is heated, due to the previous absorption of energy from irradiation [29]. This type of luminescence is only exhibited by insulators and semiconductors [24]. Figure 2.7 clearly illustrates a simple model of thermoluminescence mechanism known as a One Trap One Recombination Centre (OTOR).

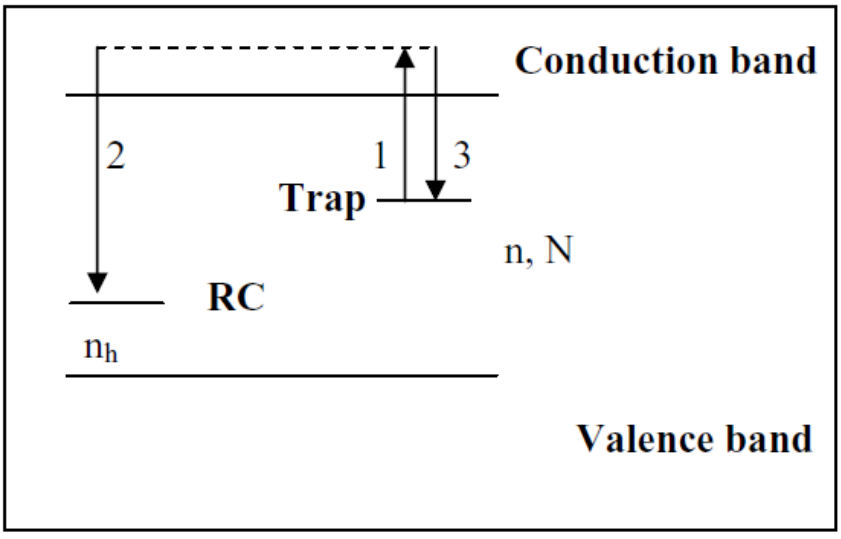

Figure 2.7: A simple two-level model illustrating the thermoluminescence mechanism [29].

In this model N represents the total concentration of traps, n the concentration of filled traps, and n_h the concentration of trapped holes in the recombination centre (RC). During the TL experiments, a sample is usually exposed to some form of excitation energy. This promotes electrons into the conduction band of a material. The promoted electrons later drop into localized metastable states called traps [29]. Heating the material at linear rate from room temperature to higher temperature, usually 500 ^{o}C, the electrons in traps absorb thermal energy, and then move into the conduction band as illustrated by transition 1 in Figure 2.7. The electrons in the conduction band can either recombine with holes in the recombination centre (transition 2), or they can be re-trapped into the electron trap (transition 3). When recombination of electrons in the conduction band and holes in the recombination centre occur, light of certain intensity according to equation 2.1 will be observed [29].

$$I(t) = -\frac{dn_h}{dt} \qquad (2.1)$$

Where I is the intensity of the emitted light, n_h is the concentration of trapped holes, t is time and the minus sign indicates the decrease of n_h with time. In thermoluminescence experiments, a glow curve of a sample can be determined from a graph of the intensity of light emitted versus the sample temperature. It is important that heating temperature be kept below that of initiating visible incandescence [24]. In most cases during TL experiments, the sample is heated using a linear heating rate according to equation 2.2

$$\beta = \frac{dT}{dt} \qquad (2.2)$$

Where β is the heating rate (^{o}Cs^{-1}), T is the sample temperature (^{o}C), and t is time (s). The temperature at maximum intensity T_m can be influenced by the heating rate, by shifting towards higher values as β increases as shown in Figure 2.8 [29].

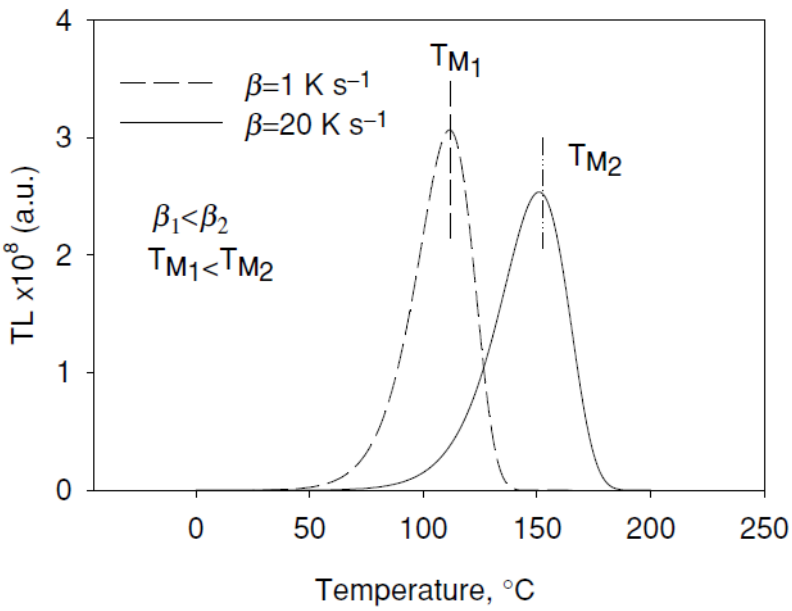

Figure 2.8: The change of temperature at maximum intensity T_m with heating rate [29].

Thermoluminescence is a special technique compared to other types of luminescence in that, once the material is heated to exhibit thermoluminescence, it cannot be made thermoluminescent again by simply cooling the samples and re-heating them [24]. The samples must be re-exposed to some excitation source before heating. This suggests that heating the sample simply triggers the release of the energy previously stored in the material through irradiation by excitation source [24].

In general, the main objective of measuring and analysing a TL glow curve is to acquire more information about a number of parameters that can be used to describe TL process in a phosphor material namely; the activation energy E, the frequency factor (S), the capture cross-section, and concentrations of the traps and recombination centres [29].

However, the information about these parameters can be determined by using the order of kinetics (b), followed by the TL glow curve. Once the order of kinetics is known, it is now possible to determine the exponential equation that governs the TL process and therefore other parameters can then be determined [24]. One way of evaluating the order of kinetics is by observing the behaviour of T_m as the concentration of trapped electrons change. If during TL measurement the temperature T_m at maximum TL intensity does not depend on the initial

concentration of trapped electrons as shown in Figure 2.9, then that TL glow curve is following the first order of kinetics [24].

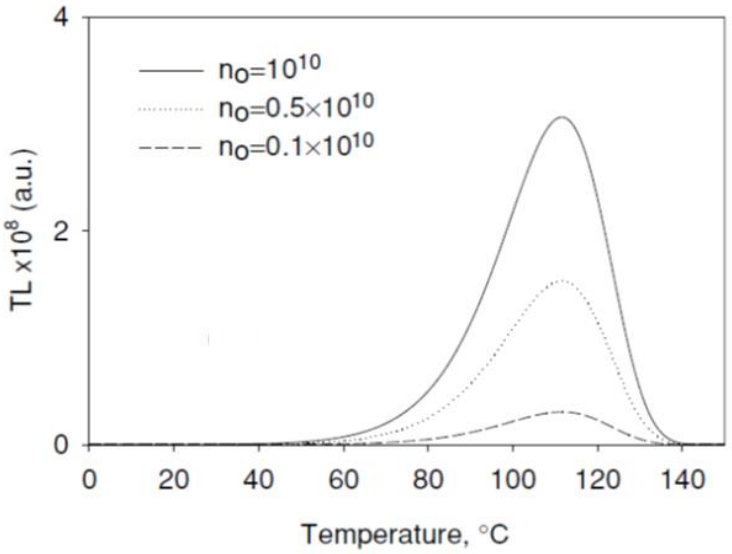

Figure 2.9: First order TL glow peaks with T_m independent of initial concentration of trapped electrons [29].

The TL process of such curves is governed by the first order equation 2.3 [29].

$$I(t) = -\frac{dn}{dt} = nSe^{-E/KT} \qquad (2.3)$$

Where *T* is the absolute temperature, *E* is the activation energy, *n* is the concentration of trapped electrons at time *t*, *S* is the pre-exponential frequency factor, and *K* is the Boltzmann's constant. If the temperature at maximum intensity depends on the initial concentration, and shifts to higher temperatures, as the concentration of trapped electrons drops as shown in Figure 2.10, then TL curve is following a second order kinetics [29].

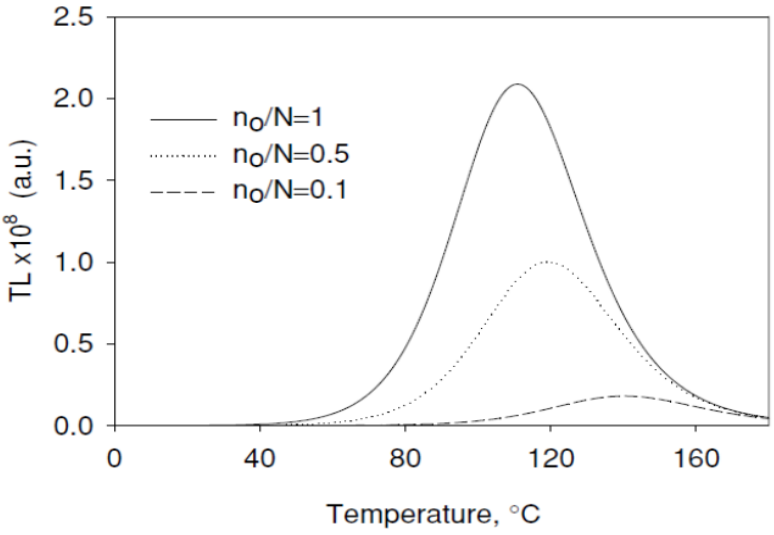

Figure 2.10: Second order TL picks with T_m depending on the initial concentration of trapped electrons [29].

The TL process of such curves is governed by a second order equation 2.4.

$$I(t) = -\frac{dn}{dt} = \frac{n^2}{N} Se^{-\frac{E}{KT}} \qquad (2.4)$$

Where T is the absolute temperature, E is the activation energy, N is the total concentration of traps n is the concentration of trapped electrons at time t, S is the pre-exponential frequency factor, and K the Boltzmann's constant. A second order kinetics occurs due to the emission of light delayed by the re-trapping process of the electrons in the traps and this phenomenon is usually observed on the descending part of the TL glow curve [29].

2.6. Experimental Procedure of Thermoluminescence

Thermoluminescence takes place when a previously ionized sample emits visible light when heated. The thermoluminescence phenomenon can only be exhibited by an insulator or a semiconductor [30, 31]. Generally, a sample is exposed to the ionizing radiation at low temperature for a certain period of time. Absorption of this energy creates electrons in the electron traps and holes in hole traps in the forbidden gap of the sample; this is usually called

trap filling. The sample is then heated, usually at a constant rate to release electrons from traps into the conduction band. The recombination of these electrons with holes in hole traps or in the valence band emits energy in the form of visible light [32, 33]. While heating of the sample is on, the light emitted by the sample is recorded and the result is a curve of light intensity as a function of temperature referred to as a glow curve [33].

The glow curve of a particular phosphor can take any form depending on various factors that are discussed below. From the geometry of a glow curve, it is possible to acquire information about the kinetic parameters such as trap depth (E), frequency factor (S), and the kinetic order (b). For example, in contrast to the second order TL glow curve, the first order TL glow curve is asymmetrical [33]. However, the symmetric nature of the second order TL glow curve does not always mean that the thermoluminescence process involved is of second order process, instead this symmetry may mean that several first order processes may have been superimposed during the temperature scan of the sample [33].

2.7. The Trap Depth in Semiconductors (Defect Levels)

Analysis of a glow curve normally yields three parameters namely, the activation energy, the electron trap and trap depth. The activation energy also known as trap depth E, is basically an extent to which a defect or a metastable level is from either the top of the valence band or from the bottom of the conduction band of a phosphor [34,35]. Electron traps are usually near the bottom of the conduction band, and hole traps are near the top of the valence band. Some traps known as luminescence centres can also be found near the middle of the band gap of a semiconductor [35]. Generally, trap depths are measured from trap levels to either the conduction or the valence band. For instance the depth of an electron trap is measured from the trap level itself to the bottom of the conduction band, and that of a hole trap is measured from the trap level itself to the top of the valence band [35].

Traps are either deep or shallow. Deep traps are usually associated with extrinsic defects and shallow traps are associated with intrinsic defects [36]. Shallow traps are traps with small ionization energies (± 0.4 eV) [37]; therefore the charge carriers trapped in these traps reside in them for a relatively short period of time [38, 36]. On the glow curve, lower temperature TL peaks are believed to be due the shallow traps [40]. On the other hand, deep traps normally hold

charge carriers in them for a longer time and a higher ionization energy is required to free these charge carriers for luminescence to occur, therefore these traps are responsible for high temperature peaks on the glow curve [40].

The interaction between electrons in deep traps and the surrounding lattice is strong such that non-radiative recombination occurs via these trap levels and reduces the luminescence efficiency of the emitting centre [12]. Typically, electrons tend to lose their absorbed energy as heat by phonons emission. Alternatively, these electrons may transfer their energy to the impurities and if these processes occur faster than radiative processes, very small amount of light will be emitted and luminescence efficiency lowers [12].

2.8. The role of the Excitation Source

The initial treatment of phosphor samples is very important during thermoluminescence measurements. For instance, it is not possible to observe thermoluminescence phenomenon (glow curve), without first exciting the materials by bombarding them with some form of energy (excitation energy) such as UV, beta, Alpha and gamma rays [24]. Quite a number of features of the observed glow curve such as the intensity of the measured peaks depend on this initial treatment.

The shape of the glow curve also depends on the type of excitation and the dose. When the dose is increased gradually, different peaks may in different ways depend on the dose, which basically makes the shape of the glow curve to be excitation dose dependent [24]. Filling of traps also changes with the change in the type of radiation but the nature of the traps remain unchanged under the influence of radiation [17].

2.9. The Effects of Excitation Time

Essentially, it is impractical to perceive thermoluminescence by simply heating a phosphor sample without exposing it to some form of irradiation. Basically this irradiation is for exciting and transferring electrons from the ground state into the traps within the forbidden gap of the host material, so that these electrons can later be thermally stimulated via the conduction band back to the lower energy levels [33].

However, it was recently reported that the glow curve intensity increases as a function of exposure time [33]. The longer the excitation time chosen, the higher the intensity of thermoluminescence signal. In addition, when the temperature at maximum thermoluminescence intensity T_m for a particular TL experiment remains unchanged regardless of the variation of exposure time, the glow curve of that particular sample is believed to follow a first order kinetics [29].

All types of luminescence discussed in the preceding sections take place due to electrons moving from higher energy states to lower energy states. It is therefore necessary to when investigating the extrinsic defects (impurities ions) in semiconductor materials to associate peaks on the luminescence spectra with transitions inside the impurity ions. For instance, the red emissions in the $Na_3Gd(PO4)_2:Eu^{3+}$ phosphor are associated to the F-F transitions of the Eu^{3+} ion in the $Na_3Gd(PO4)_2$ host lattice [39]. Transitions of dopant ions used in this work are discussed below.

2.10. The *4f - 4f* Intra-configurational Transitions of Eu^{3+} Ion

The emission spectrum of Eu^{3+} usually consists of narrow and line bands in the red region of the spectrum. The narrow nature of these bands can be attributed to their insensitivity to the surrounding chemical environment. Most of these lines belong to the transitions of $^5D_0$ level to the ^7F_j (j = 0, 1, 2, 3, 4, 5, 6) levels as shown in figure 2.11.

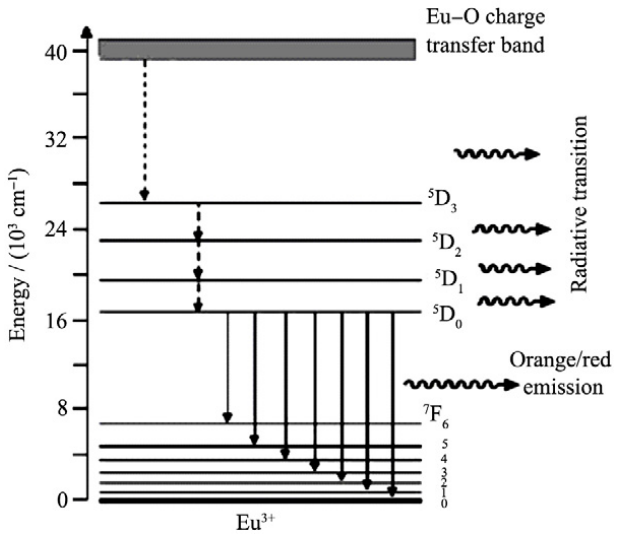

Figure 2.11: Electronic energy level diagram of Eu^{3+} ion [40].

The f-f transitions are parity forbidden according to Laporte's parity selection rule. Nevertheless, these transitions become partially allowed under the influence of the surrounding crystal field, due to the admixing of electronic states of opposite parity into the $4f^n$ configuration, and are therefore referred to as induced or forced electric dipole transitions [41]. Some of these induced electric dipole transitions are highly sensitive to the environment surrounding the Eu^{3+} ion, and are referred to as hyper-sensitive transitions [35]. Usually, the red colour is obtained through these hyper-sensitive transitions in Eu^{3+} ion, i.e. $^5D_0$ - $4F^n$ electric dipole transition [42]. The splitting of emission transition lines yields crystal field splitting of the ^7F_j levels. This can be attributed to the $^5D_0$ not being split by the crystal field (because j = 0) [43].

2.11. The *5d*^{1} - *4f* Transitions of Eu^{2+} Ion

The incorporation of Eu^{2+} ion into different host matrices produces a wide range of emission and absorption bands. The Eu^{2+} ion is usually composed of broad absorption and emission spectra that can be attributed to a transition between $^8S_{7/2}$ and the crystal field components of the $4f^6 5d^1$ configuration [44]. Unlike the *4f* orbital, the 5d orbital is not shielded by $5s^2 5p^6$ and therefore it is susceptible to the crystal field, and depending on the intensity of the crystal field, the $4f^6 5d^1$ configuration can lie either on top or below the $4f^7$ excited state ($^6P_{7/2}$) [44]. In the

case where $4f^6 5d^1$ is located above the $4f^7$ excited state, narrow emission lines can be observed [44]. Figure 2.12 shows how the crystal field splits the $4f^6 5d^1$ configuration of the Eu^{2+} ion and how it affects its luminescence properties.

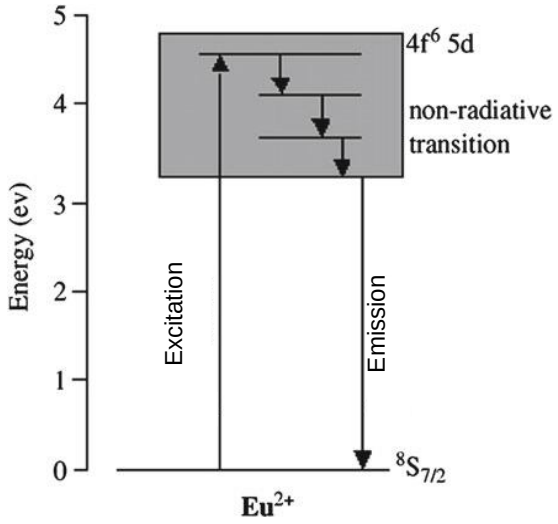

Figure 2.12: Electronic energy level diagram of Eu^{2+} ion [45].

The emission of the absorbed energy can be either a narrow line emission that can be attributed to $^6P_{7/2} \rightarrow {}^8S_{7/2}$ transition in the UV region, or a broad band emission due to $4f^6 5d^1 \rightarrow {}^8S_{7/2}$ transitions [46].

2.12. The *4f-4f* Electronic Transitions of Dy^{3+} Ion

Apart from weak emission lines in the red region of the visible spectrum due to $^4F_{9/2} \rightarrow {}^6H_{11/2}$ transition, Dy^{3+} is also well known to have narrow emission lines on the blue, as well as on the yellow region of the spectrum [47,48]. The blue emission lines can be attributed to $^4F_{9/2} \rightarrow {}^6H_{15/2}$ transition and the yellow lines is due to $^4F_{9/2} \rightarrow {}^6H_{13/2}$ transition. These transitions are shown in figure 2.12.

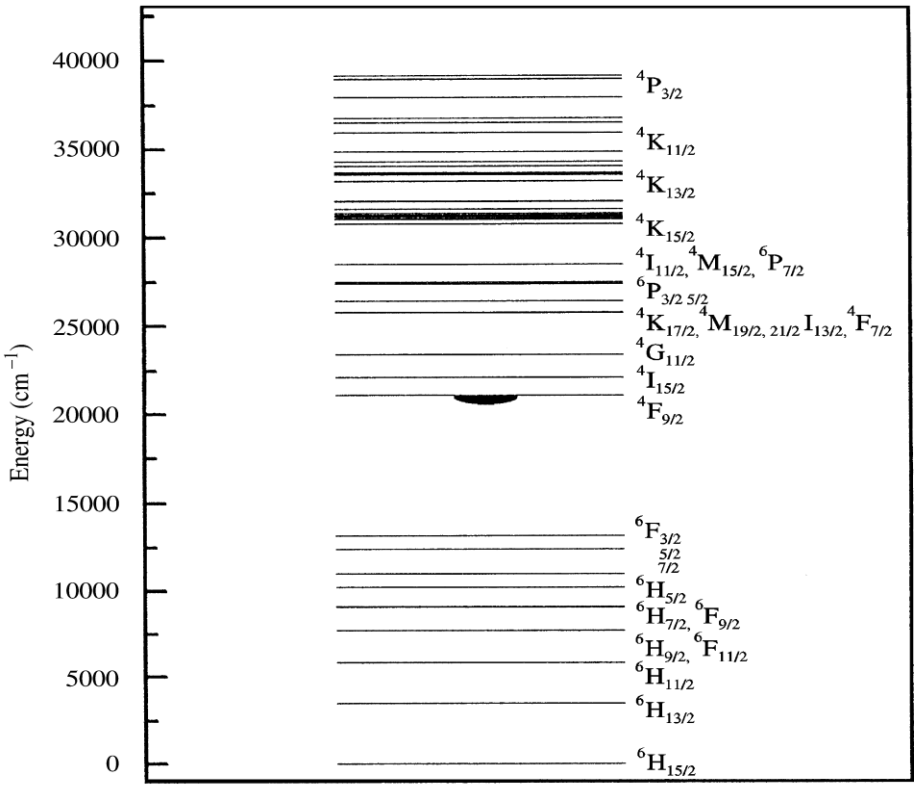

Figure 2.13: Electronic energy level diagram of the Dy^{3+} ion [49].

2.13. Electronic Transitions of Mn^{2+} Ion

Mn^{2+} is known to have emissions that can be influenced by the crystal field ranging from green to orange-red regions of the visible spectrum due to the $^4T_1(^4G) \rightarrow {}^6A_1(^6S)$ transition [43], which suggests that the emission color of the Mn^{2+} ion is influenced by the environment surrounding it. When Mn^{2+} is octahedrally coordinated, the effect of crystal field is strong and the $^4T_1(^4G) \rightarrow {}^6A_1(^6S)$ transition tends to give a red or orange emission. In contrast, when Mn^{2+} is tetrahedrally coordinated, the $^4T_1(^4G) \rightarrow {}^6A_1(^6S)$ green emission can be observed [46,50]. This type of behaviour widens the applications of Mn^{2+} doped materials in fluorescent lamps, cathode ray tubes, and white light emitting diodes [49]. Figure 2.13 shows the schematic diagram of Mn^{2+} energy levels and electronic transitions taking place in the d orbital of Mn^{2+}.

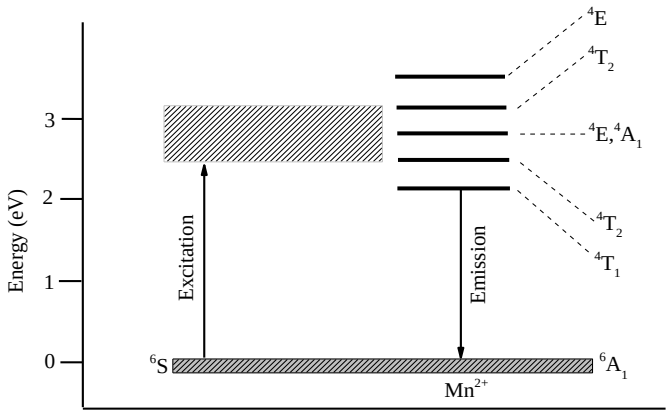

Figure 2.14: A schematic diagram of Mn^{2+}energy levels [45].

During excitation, electrons will enter the conduction band of the host material and the lowest excited state $^6T_1$ leaving behind holes in the valence band and the ground state $^6A_1$ of Mn^{2+}. The subsequent recombination of these electrons with holes in the ground state of Mn^{2+} may result in photoluminescence.

References

1. W. M. Yen, M. J. Weber, Phosphor Handbook, Composition, Preparation and Optical Properties, CRC Press , Boca Raton, 2004, pp8
2. 1. L. Ozawa, Cathodoluminescence and Photoluminescence: theory and practical Applications, CRC Press, 2010, pp 1-4
3. Richard J. D. Tilley, Defects in Solids, John Wiley & Sons, 2008, pp 420-422
4. W. M. Yen, Phosphor Handbook, CRC Press, 1998, pp 4
5. B. G. Yacobi, D. B. Holt, Cathodoluminescence Microscopy of Inorganic Solids, Springer, 1990, pp 21
6. B. kazan, ADV electronics electron physics, Academic Press, 1990, pp 283
7. Mihail Nazarov, Do Young Noh, New Generation of Europium- and Terbium-Activated Phosphors: From Syntheses to Applications, CRC Press, 2011, pp 16-17
8. http://en.wikipedia.org/wiki/F%C3%B6rster_resonance_energy_transfer/04/05/2014/17:36
9. M. Sauer, J. Hofkens, J. Enderlein, Handbook of Fluorescence Spectroscopy and Imaging: From Ensemble to Single Molecules, John Wiley & Sons, 2010, pp 6.
10. W. M. Yen, S. Shionoya,H. Yamamoto, Fundamentals of Phosphors, Taylor and Francis Group, 2007,pp 6-21
11. K. A. Gscheidner, J. C. G. Bunzli, V. K. Pecharsky, Handbook on the Physics and Chemistry of Rare Earths: Optical Spectroscopy, Elsevier, 2007, pp 228
12. E. Nakazawa, Phosphor Handbook, Second Edition, Fundamental of phosphors,Taylor & Francis Group,LLC., pp48
13. Elliot, The Physics of and Chemistry of Solids, England, 1998, pp145
14. E. G. Seebauer, M. C. Kratzer, Charged Semiconductor Defects: Structure, Thermodynamics and Diffusion, Springer-Verlag London Limited, 2008, pp5
15. J. P. Mercier, G. Zambelli, W. Kurz, Introduction to Material Science, Elsevier, Paris, 2002, pp 158
16. http://academic.uprm.edu/pcaceres/Courses/MatEng3045/EME3-2.pdf, 19/05/2014
17. M. S. Vijaya, G. Rangarajan, Materials Science, Tata McGraw-Hill, New Delhi, 2003, pp 95
18. http://www.me.umn.edu/~dtraian/Thesis_Evgenia.pdf, 19/05/2014
19. M. C. Tamargo, II-VI Semiconductor Materials and their Applications, CRC Press, 2002, pp124
20. S. J. Pearton, Processing of Wide Band Gap Semiconductors, Noyes Publications, USA, 200, pp 393
21. V.S. Bagad, Optical Fiber Communications, Technical publications Pune, India, 2009, pp 3-7
22. A. Kitai, Luminescent Materials and Applications, John Wiley & Sons, 2008, pp 32
23. S. Nakamura, S. F. Chichibu, Introduction to Nitride Semiconductor, Blue Lasers, And Light Emitting Diodes, Taylor & Francis, London, 2000, pp 4
24. S. W. S Mckeever, Thermoluminescence of Solids, Cambridge University Press, USA, 1985, pp 2-27

25. I. Pelant, J. Valenta, Luminescence Spectroscopy of Semiconductors, Oxford University press, UK, 2012, pp 142
26. S. Parveen, M. S. Aslam, L. Hu, G. Xu, Electrogenerated Chemiluminescence: Protocols and Applications, Springer Science & Business Media, New York, 2013, pp2.
27. http://www.physik.unibas.ch/Praktikum/VPII/Fluoreszenz/Fluorescence_and_Phosphorescence.pdf, 04/05/2014
28. http://scholarworks.uno.edu/cgi/viewcontent.cgi?article=1175&context=td**,** 06/05/2014
29. Pagonis, G. Kitis, C. Furetta, Numerical and Practical Exercises in Thermoluminescence, Springer, USA, 2006, pp 18-34
30. F. Trager, Springer Handbook of Lasers and Optics, Springer, New York, 2007, pp 622
31. A. J. J. Bos, Journal of *Radiat. Meas.***41** (2007) 45-56
32. J. M. Ducruet, I. Vass, *Photosynth. Res.* **101**(2009) 195-204
33. S. S. Pitale , S. K. Sharma, R.N. Dubey, M.S. Qureshi, M.M. Malik, *Chalcog. Lett.* **3** (2013) 121-129
34. K. W. Böer, Survey of Semiconductor Physics: Barriers, Junctions, Surfaces, and Devices, Van Nostrand Reinhold, 1992, pp 535
35. C. Furetta,Handbook of Thermoluminescence, World Scientific, USA, 2010, pp 1-538
36. N. I. Ostapenko, V. I. Sugakov, M. T. Shpak, Spectroscopy of Defects in Organic Crystals, Kluwer Academic Publishers,1993, pp204
37. K. Van den Eeckhout, P. F. Smet, D. Poelman, Materials. **3** (2010), 2536-2566
38. V. I. Mikla, V. V Mikla, Trap level Spectroscopy in Amorphous Semiconductors, Elsevier, 2010, USA, pp3
39. T.Chengaiah, B.C. Jamalaiah, L.Rama Moorthy, Spectrochimica Acta Part A: Molecular and Biomolecular Spectroscopy, 2014, 495-500
40. K. N. Shinde, S. J. Dhoble, A. Kumar, *J.Rare Earths.* **29** (2011), 527-535
41. Pekka. H, Harri. H, Lanthanide Luminescence: Photophysical, Analytical and Biological Aspects, Springer, New York, 2011, pp 10 – 11
42. J. C. Krupa,N. A. Kulagin, Physics of Laser Crystals, Kluwer Academic Publishers, USA, 2003, pp 25
43. M. Gaft, R. Reisfeld, G. Panczer, Modern Luminescence of Minerals and Meterials, Springer, Verlag Berlin Heidelberg, 2005, pp 144-200.
44. G. Blasse, Journal of Physica status solidi (b),vol.55, pp 131-134
45. K. N. Shinde, S. J. Dhoble, H. C. Swart, K. Park, Phosphate Phosphors for Solid-State Lighting, Springer, Heidelburg, 2012 pp 99-157
46. Trager, Springer Handbook of Lasers and Optics, Springer, New York, 2007, pp 622
47. J. Lsommerdijk, A.C Van Amstel, F.M.J.H. Hoex-Strik, *J. lumin.* **11** (1976) 433-436
48. G. S. R. Raju, J. Y. Park, H. C. Jung, B. K. Moon, J. H. Jeong, *J. Curr. App. Phys.* **9** (2009) 92-95
49. N Xei, J. Liu, Y Huang, S Kim, H. J. Seo, *J.Ceram Internat*, **38** (2012)1489-1495
50. H. Choi, C. Kim, C. Pyun, S. Kim, *J. Lumin.* **82** (1999) 25-32

CHAPTER 3

Experimental Research Techniques

3.1. Introduction

This chapter presents a brief description of the synthesis method and the non-destructive characterization techniques, used in this study. Combustion method was used to synthesize the alkaline earth aluminate phosphor powders. The X-ray diffraction (XRD) and the scanning electron microscope (SEM) were used to study the crystalline structure and the particle morphology of the powder phosphors respectively. FluoroLog-3 PL, UV-Vis and Thermoluminescence systems were used to investigate various luminescence properties of the samples.

3.2. Synthesis

3.2.1. Combustion Method

Combustion method is a rapid exothermic and auto-propagating reaction process used to synthesize materials up to nanoscale level [1]. There are lots of ceramic powders at nanoscale that have been synthesized by combustion method and most of them have been applied in various industries. For instance, ceramic oxide such as MAl_2O_4 (M = Sr, Ba, Mg, etc.) can be prepared by mixing metal nitrates (oxidizer) in aqueous solution with urea ($NH_2CO(NH_2)$ or glycerine ($C_2H_5NO_2$) as fuel, as well as the reducing and complexing agent of the metal ion in the solution [1]. The nitrates precursors are then mixed thoroughly to obtain a homogeneous solution and put into the furnace that is usually set to temperatures lower than the phase transition of the target materials, typically around 500 ^oC [2]. After three to five minutes, the mixture boils, decomposes, dehydrates, and rapture into a flame that lasts for 15 seconds [3] and forms a foamy crystalline powder which occupies the whole volume of reaction container [4].

Figure 3.1 clearly shows all the steps and processes involved immediately after the reactants have been introduced into a muffle furnace, maintained at a certain temperature.

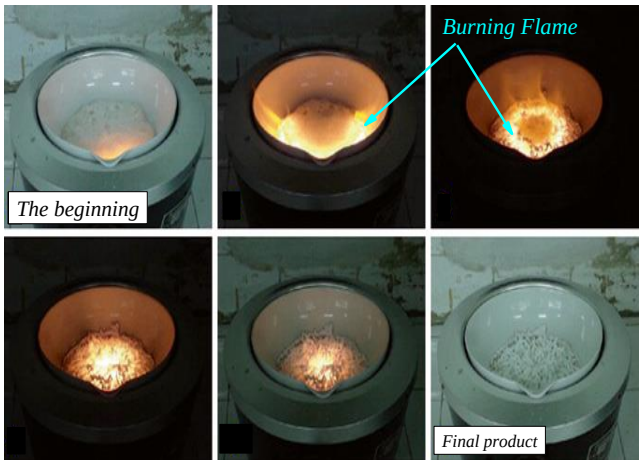

Figure 3.1 A typical synthesis process of ceramic oxide powders by combustion method [1].

Some by-products such as N_2, CO_2 and H_2O escape from the reaction mixture during the process [2]. The escaping of these gases removes heat from the reaction providing ideal environment for the formation of fine crystallite size powders, and this makes combustion method even more preferable in the production of ceramic oxide powders [1]. When the gases escape, large clusters are broken, creating pores between particles which enhance more heat release from the reaction mixture and this obstructs the growth of the particles [1], resulting in small particles with increased surface area of the ceramic oxide powders [2]. Both the crystallinity and the surface area of the powder may be influenced by the ignition temperature. For instance, the heating rate of the reactants depends on the furnace temperature [1]. When the temperature is too high, the reaction mixture boils rapidly, increasing the chances of residual water at the time of ignition which will lower the flame temperature. These conditions will negatively affect the crystallinity of the product [2]. Conversely, when the furnace temperature is very low, the gases will escape from the reaction mixture at a very low rate and this will make it impossible for combustion process to take place [1].

During the reaction process, high reaction temperature is generated from within the reaction itself, which can volatilize impurities that have low boiling point and result in the formation of more pure products, which adds to other advantages of the combustion method [4]. Another advantage of combustion method is brought by its simplicity, and low processing costs. Also, it is possible to achieve fine, homogeneous, and highly crystalline as-prepared powders via this synthetic technique [1, 5].

3.3. Characterization Techniques

3.3.1. Scanning Electron Microscope (SEM)

Scanning Electron Microscope is a versatile technique used to examine and analyse the microstructure morphology of various materials [6]. This technique consists of four basic components, namely the electron gun, the specimen stage, electron beam scanning coils and signal detector. The schematic diagram of SEM in Figure 3.2 clearly shows all the key components of the system.

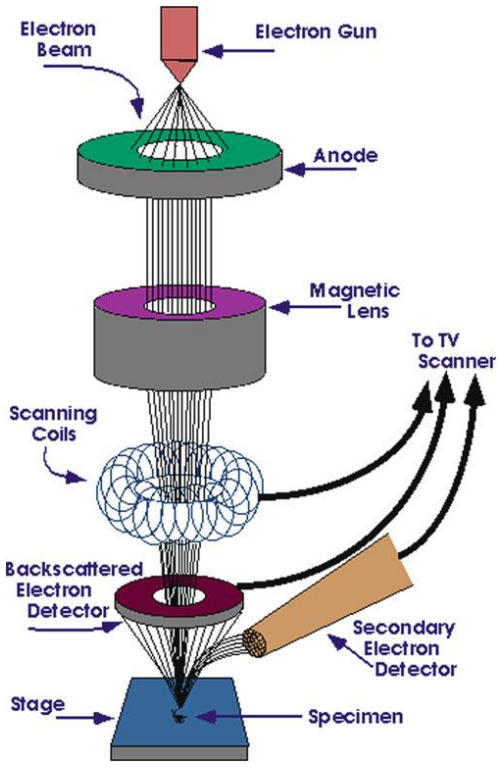

Figure 3.2: A schematic Diagram of Scanning Electron Microscope showing the path of the electron beam from the electron gun to the specimen and all the basic components [4].

During the experiment, a beam of high energy electrons generated by electron sources, usually tungsten filament cathode or lanthanum hexaboride (LaB_6) inside the gun is focussed onto the specimen to be scanned across the sample as shown in Figure 3.3 [4].

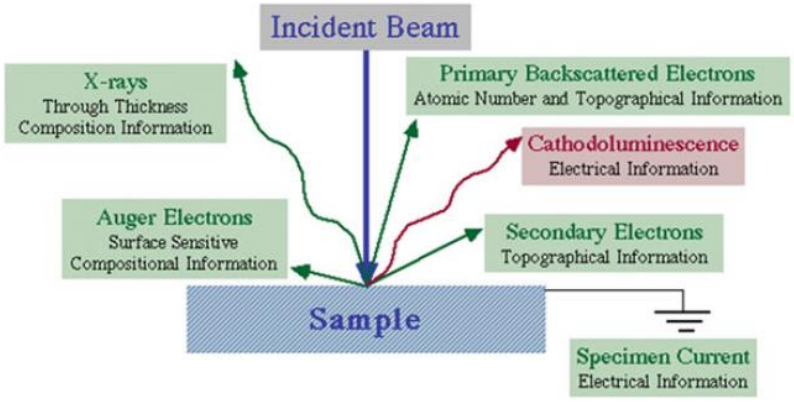

Figure 3.3: A schematic illustration of Sample-Surface interaction to produce different signals for surface analysis [4].

This high energy beam interacts with the surface of the sample. This sample-surface interaction then results in a number of signals escaping the surface of the sample, namely low energy secondary electrons, back-scattered electrons, Cathodoluminescence, transmitted electrons, and characteristic x-ray emission [4]. These signals have information about the surface topography and characteristic features of the sample and this information can be collected using the appropriate detectors. For example, the secondary electrons are usually collected by a scintillation-photomultiplier system [7].

In principle, there are three ways of imaging the surface of the sample during SEM measurements, namely by detection of secondary electrons, backscattered electrons, and characteristic X-rays [4]. Secondary electrons are primarily used to visualise the texture and roughness of the sample surface. Backscattered electrons are detected to provide both compositional and topographic information about the sample, and the characteristic X-rays and Auger electrons are both detected to provide chemical information about the sample. The transmitted electrons provide elemental information and distribution when coupled with X-ray microanalysis [8].

3.3.2. X- Ray Diffraction

X-ray diffraction is a technique used to identify the crystalline phases, to determine phase composition and to estimate the particle size of materials. The crystalline materials can be powders, ceramics, polymers and metals [9]. X-ray diffractometer consists of three basic components namely, X-ray source, goniometer and X-ray detector. The device used to position the sample and the detector is usually a goniometer [10]. X-rays are produced in the X-ray tube consisting of two metal electrodes, cathode and anode. Usually, a cathode filament is heated and electrons are produced and accelerated by a highly negative potential on the cathode to the target anode at ground potential. The most common targets used are Cu, Mo, W, Cr and Co. When the accelerated electron has enough energy to knock out an electron in the inner-shell of the target material, the atom will be excited with a hole left in the electron shell. If this hole is occupied by an electron from the outer shell, characteristic X-ray spectra having different components will be produced [11].

Mostly, important components for diffraction studies are k_α and k_β, and the most commonly used component from the x-ray tube is the k_α component which has a wavelength of 1.5418Å when a Cu is used as a target anode [12]. For most diffraction studies, a monochromatic X-ray beam is required and this requirement can be achieved by filtering out unwanted X-ray lines with the use of a foil or a crystal monochromator [12]. In a typical XRD set-up, the x-rays exiting the window of the X-ray tube are collimated by the collimating slits and directed onto the sample as shown in Figure 3.4.

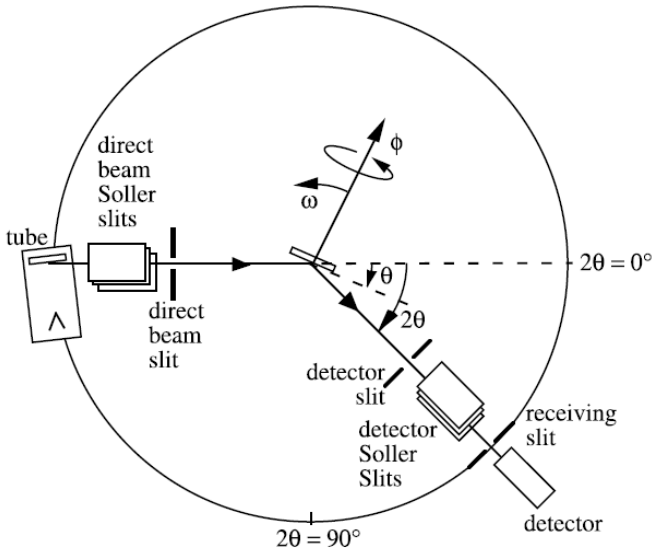

Figure 3.4: A schematic illustration of X-ray Spectrometer [13].

As the sample is rotated at angle θ, while the detector moves along a focussing circle at an angle 2θ, the intensity of the reflected X-rays are recorded by the detector. When the X-ray beam strikes the sample at a geometry that satisfies Bragg's Law in equation 3.1, constructive interference will occur and a diffraction peak will be recorded by the detector and the crystalline phase of the material can be identified from the diffraction pattern [14, 15, 16]. Bragg's Law is applied to explain the interference of the beam during the experiment according to equation 3.1. The resulting diffraction pattern is used to identify the sample's crystalline phases and to measure its structural properties, the size and orientation of the crystallites [17].

$$n\lambda = 2d\sin\theta \qquad (3.1)$$

Where d is the spacing between atomic planes in the crystalline phase, λ is the wavelength of the X-rays used, θ is the angle between the incident X-rays and the sample, 2θ is the diffraction angle and n is an integer (1, 2, 3, 4 etc.) which represents the order of diffracted beams.

3.3.3. UV-VIS Spectrophotometer

UV-Vis Spectrophotometer is used to measure transmittance and absorbance of nanomaterials as a function of wavelength of electromagnetic radiation [18]. It consists of an electromagnetic

radiation source, a dispersion source, a sample area, and couple of detectors. There are two light sources that are commonly used in the UV-Vis spectrophotometers namely, deuterium arc lamp, and tungsten-halogen lamp. The tungsten-halogen lamp has an advantage of a longer lifetime over the deuterium arc lamp. However most spectrophotometer used for measurements in the UV-visible range have both types of light sources. In such systems, either a source selector is used to select the appropriate light source or the light from the two sources is mixed to yield a single broadband light source [19].

This technique is based on the measurement of the absorption of light by the sample. Typically, polychromatic light from the source is focussed on the entrance slit of a monochromator. The monochromator then filters this light to produce a monochromatic light as shown in Figure 3.5. This monochromatic light passes through the sample to the detector. If the sample absorbs this light at some wavelength, the light that is transmitted will be reduced. This absorbance of a sample is determined by a comparison between the intensity of light detected without passing through the sample and that detected after passing through the sample. A plot of the transmitted light intensity as a function of wavelength gives the absorption spectrum of the sample [19].

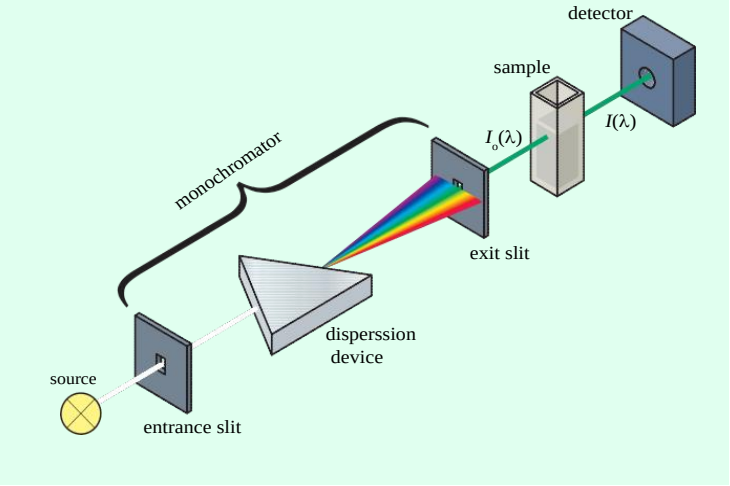

Figure 3.5: Schematic diagram of the key components of a typical UV-Vis spectrometer [19].

The fundamental operating principle of this technique is based on the measurement of absorption of light by the sample as electronic transitions take place in response to the light directed onto

the sample [19]. Using the Beer's equation 3.2, characteristics of the sample such as absorbance can be determined.

$$A = \log \frac{I_o}{I} = \varepsilon lc = \alpha c \qquad (3.2)$$

Where I_o and I are incident light intensity and transmitted light intensity respectively and both of them can be measured experimentally. When I_o and I are known, the absorbance *A* can be determined. ε is the molar absorptivity. If the concentration of the solution sample c and the path length of the sample l are known, the absorption coefficient α can be determined [20].

3.3.4. Photoluminescence Spectroscopy (FluoroLog 3)

FluoroLog 3 is a spectrofluorometer instrument which is used for phosphorescence and fluorescence spectral data acquisitions [21]. The FluoroLog-3 system is equipped with a 450W continuous xenon lamp as an excitation source for fluorescence steady state measurements. It is also equipped just behind the continuous lamp, with a flashing lamp as an excitation source for phosphorescence steady state measurements [21]. Fuorolog-3 system is composed of four basic components namely, the monochromators, sample compartment, detectors, and accessories. The double grating monochromators in the excitation and emission paths are responsible for the system's considerable increase in sensitivity, resolution, and stray-light rejection [21] i.e. light from the gratings in the monochromator due to the monochromator's reflection of light from the source in different overlapping orders [22] as shown in Figure 3.6.

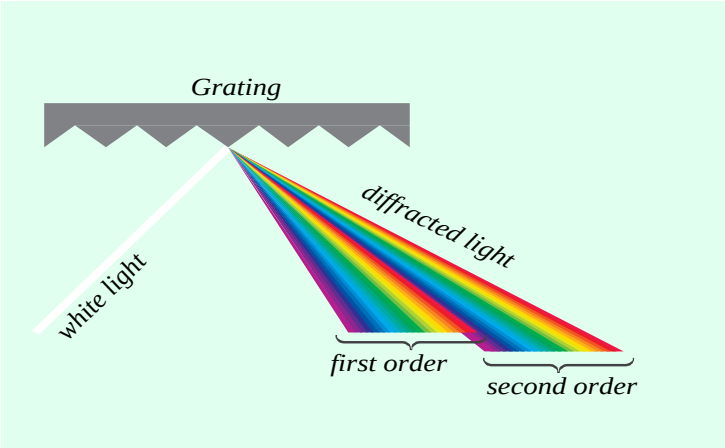

Figure 3.6: A schematic representation of reflection of light by the grating in the monochromator resulting in second order peaks on PL spectra [22].

The sample compartment of the fluorlog-3 is a T-box with two options of emission signal collection namely, the front-face emission collection which is ideally for solid samples, and the right-angle emission collection for solution samples [21]. This system is also equipped with four detectors namely, a silicon photodiode reference detector, the standard R928P photomultiplier tube, the InGaAS detector, and lastly the PbS detector [21]. A silicon photodiode reference detector monitors the xenon lamp and compensate for changes in the xenon lamp output. A R928P photomultiplier tube is used for steady state and lifetime measurements, and it is sensitive from ultraviolet (UV) to the visible region of the electromagnetic spectrum i.e. 190 nm to 860 nm. The InGaAS detector is used for steady state acquisition in the near-Infrared (IR) region of the spectrum. This type of detector shows sensitivity in the 800 nm to 100 nm range but with a noisy signal. When cooled with liquid nitrogen, this detector shows a good sensitivity from 800 nm to 1550 nm with less noise from the background. The PbS detector is also for steady state measurements in the IR region of the electromagnetic spectrum i.e. 1000 nm to 3000 nm [21].

In this study, the FluoroLog-3 spectrophotometer was used to investigate the photoluminescence properties of the prepared phosphor materials. During steady state photoluminescence experiments, the xenon lamp light source produces polychromatic light beam, which is then

filtered in the excitation monochromator as shown in Figure 3.7. A single wavelength of light from the excitation monochromator reaches the sample in the sample compartment. The interaction between the sample and the incident radiation produces a signal, which is then filtered by the emission monochromator before it reaches the photomultiplier detector. By recording a change in intensity with the variation of excitation or emission wavelength, excitation or emission spectrum can be produced [21].

However, the system is not limited to steady state measurements; instead it can also do lifetime measurements i.e. short lifetime and long lifetime measurements. For short lifetime measurements, the system is operated in time-correlated Single Photon Counting (TCSPC) mode [23]. In contrary to steady state mode, the TCSPC mode involves excitation of the samples from the Nano-LEDs controlled from the Data station software, while the decay curve is being collected [23]. The acquired decay curve is fitted and analysed using the decay analysis software. Also, the Data station controls the delta led's during up-conversion measurements [21]. For long lifetime measurements, the samples are excited from the continuous xenon lamp for a given time, after which the slits on the excitation monochromator close and cease excitation. The luminescence decay curve can then be collected and fitted with analysis software [21]. Information about the signal is transferred to and from the computer via a controller (Spectracq) which is connected to the spectrofluorometer components as shown in Figure 3.7.

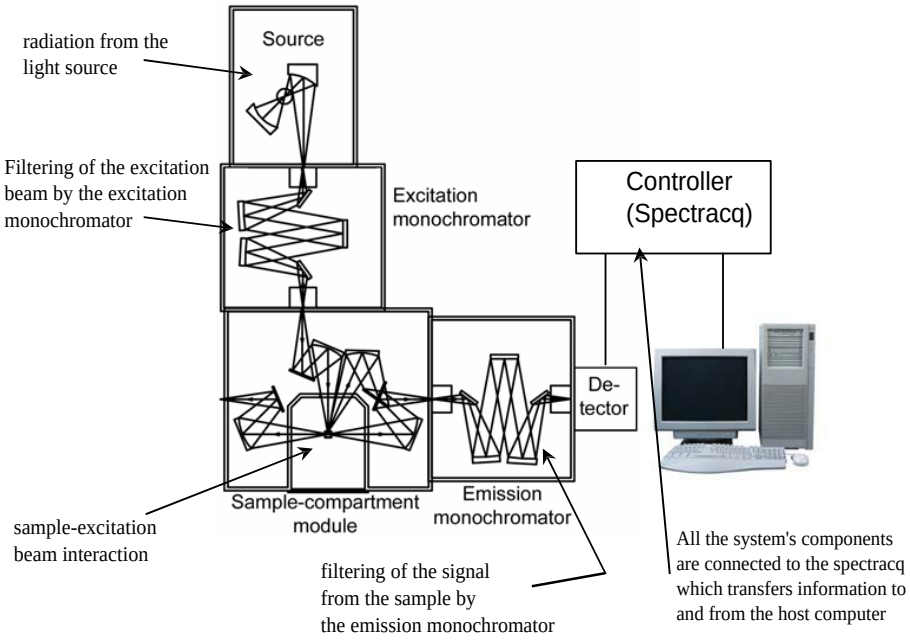

Figure 3.7: A schematic representation of the FluoroLog-3 system showing path of excitation source from the source to the detector [24].

During the experiments, the quality of the collected data is significantly affected by the signal-to-noise (S/N) ratio. For instance the detected emission signal might contain some unwanted signal originating from noise and dark counts [21]. However, the FluoroLog-3 system offers the possibility to improve this ratio for a better data acquisition. Choosing a suitable integration time i.e. the length of time during which photons are counted and averaged can improve the signal-to-noise ratio. Making the integration time longer averages the signal for a longer time, and this produces high quality results. S/N ratio can also be improved by scanning a region several times and average the results. Another way is to adjust the slit widths of the monochromators by changing the band-pass [21].

References

1. http://www.springer.com/978-3-642-41274-5, 14/03/2014
2. C. R. Ronda, T. Welker, Proceedings of The Sixth International Conference on Luminescent Materials, Electrochemical Society,1998, pp 23
3. W. M. Yen, M. J. Weber, Inorganic Phosphors: Compositions, Preparation and Optical Properties, CRC Press, 2004, pp 402
4. K. N. Shinde, S. J. Dhoble, H. C. Swart, K. Park, Phosphate Phosphors For Solid-State Lighting, Springer, Berlin Heidelberg, 2012, pp 77-100
5. A. Lakshmanan ,Luminescence and Display Phosphors: Phenomena and Applications, Nova Publishers, 2008, pp 84
6. Z, Li, Industrial Applications of Electron Microscopy, CRC Press, 2002, pp 1
7. H. Schatten, Scanning Electron Microscopy for the Life Sciences, Cambridge University Press, 2013, pp 2-4
8. W. Zhou, Z. L. Wang, Scanning Microscopy for Nanotechnology: Techniques and Applications, Springer, 2007, pp 2-8
9. E. Lifshin, X-ray Characterization of materials, John Wiley & Sons, 2008, pp 52
10. R. A. Fava, Crystal Structure and Morphology, Academic Press, 1980, pp 61
11. C. Suryanarayana, M. G. Norton, X-ray Diffraction: A practical Approach, Plenum Press, 1998, pp 9
12. J. Drenth, Principles of Protein X-ray Crystallography, Springer, 1999, pp 49
13. C. Suryanarayana, M. G. Norton, X-ray Diffraction: A practical Approach, Plenum Press, 1998, pp 9
14. C. R. Brundle, C. A. Evans, S. Wilson, Encyclopedia of Materials Characterization: Surfaces, Interfaces, Thin Films, Gulf Professional Publishing, 1992, pp 203-204
15. Y. Leng, Materials Characterization: Introduction to Microscopic and Spectroscopic Methods, John Wiley & Sons, 2013, pp 200
16. http://serc.carleton.edu/research_education/geochemsheets/techniques/XRD.html, 30/03/2014
17. C. R. Brundle, C. A. Evans, Jr., S. Wilson, Encyclopedia of Materials Characterization, Butterworth-Heinemann, 1992, pp 198
18. E. Le Ru, P. Etchegoin, Principles of Surface-Enhanced Raman Spectroscopy, Elsevier, Netherlands, 2008, pp 59
19. T, Owen, Fundamentals of Modern UV-visible Spectroscopy, Agilent Technologies, Germany, 2000, pp 40-68
20. http://media.rsc.org/Modern%20chemical%20techniques/MCT4%20UV%20and%20visible%20spec.pdf, 18/05/2014
21. FluoroLog-3 Spectrofluorometer: operational manual Part Number J81014 rev.D
22. Tonny Owen, Fundamentals of UV-Visible spectroscopy, Agilent technologies, 2000, pp 33

23. FluoroLog-3 Spectrofluorometer: User's Guide Part Number J81119 ver.E
24. http://philipyip.files.wordpress.com/2013/08/FluoroLog-3-manual.pdf, 18/05/2014

CHAPTER 4

Synthesis and characterization of $SrAl_2O_4$ doped with with Eu^{2+}, Dy^{3+} and $MnMn^{2+}$ ions phosphors prepared by combustion method.

4.1. Introduction

Currently the investigation of various phosphor materials is mainly based on how improve the efficiency of several devices. Examples of these devices are Plasma Display Panels (PDPs), Cathode Ray Tube (CRT), Liquid Crystal Display, Light Emitting Diodes (LED) TVs etc. [1]. Phosphors are currently plays a vital role in in the quality of images on digital screens. The research on how to improve these devices is mainly focused on the luminescence color, increased phosphor screen luminescence and longer operational time [2]. This can be achieved by making a good choice of dopants and host lattices when synthesizing phosphors to be used on these devices .Applications of several phosphor materials such as ZnS:Ag:Cl (blue), ZnS:Eu:Cl (green), and Y_2O_2S:Eu (red) have already been reported [2]. However, sulphide phosphors have some drawbacks; long persistent luminescence is impossible due to their narrow band gaps compared to other hosts such as aluminates [3]. Generally, for long persistent luminescence to occur, the requirement is the formation of deep traps within the forbidden gap of the host material. This formation of deep traps is not possible in narrow band gap materials. Sulphide based phosphors also have a drawback of chemical instability [3].

Alkaline earth aluminate hosts are known to have wide band gaps (around 6eV). The charge compensation taking place within the band gap could lead to the formation of deep traps [3]. In addition, when alkaline aluminate hosts are doped with rare earth ions, the brighter and longer persistent luminescence characteristics in the visible region of the spectrum are usually observed [4], and this is what makes these kinds of materials potential candidates for applications mentioned above. Their radiation-less nature and chemical stable host lattice are some of the key

properties of achieving brighter and longer lasting luminescence when doped with lanthanides. [5].

On the other hand, Mn^{2+} ions have shown interesting emissions in the visible region of the spectrum. The only disadvantage is its low emission intensity in various host materials, and this limits practical applications of Mn^{2+} doped materials [4]. The low intensity is due to parity and spin forbidden nature of the $d \rightarrow d$ transition [4]. However, the Mn^{2+} is known to be a good activator as well as a good sensitizer when co-doped with other elements [4]. In this study we investigate the structural and luminescence studies of $SrAl_2O_4:Eu^{2+}$, $SrAl_2O_4:Dy^{3+}$, $SrAl_2O_4:Mn^{2+}$; $SrAl_2O_4:Eu^{2+}$, Dy^{3+}; $SrAl_2O_4:Eu^{2+}$, Mn^{2+}; $SrAl_2O_4:Mn^{2+}$, Dy^{3+} and $SrAl_2O_4:Eu^{2+}$, Mn^{2+}, Dy^{3+} phosphors, as well as how to improve long persistent luminescence of the $SrAl_2O_4:Eu^{2+},Dy^{3+}$ phosphor by incorporating Mn^{2+} ion.

4.2. Experimental Procedure

4.2.1. Synthesis

All the samples used in this study were prepared by combustion method. The appropriate nitrates ($Sr(NO_3)_2$, $Al(NO_3)_3$, $Dy(NO_3)_3$, $Eu(NO_3)_3$, and $Mn(NO_3)_2$ all in analytical purity of 99.9% were used as starting materials and urea (CH_4N_2O) was added into the mixtures as a reducer and a flux. The mixtures were milled in crucibles until homogeneous mixtures were obtained. The crucibles containing the mixtures were placed into a furnace to calcine the mixture in air at 600 ^oC for 5 minutes. White ashes for samples without Mn^{2+}, and brownish ashes for Mn^{2+} containing samples were obtained. All the samples were then further milled in agate mortar to obtain homogeneous final powder phosphors.

4.2.2. Characterization

$SrAl_2O_4:Eu^{2+}$, $SrAl_2O_4:Dy^{3+}$, $SrAl_2O_4:Mn^{2+}$; $SrAl_2O_4:Eu^{2+}$, Dy^{3+}; $SrAl_2O_4:Eu^{2+}$, Mn^{2+}; $SrAl_2O_4:Mn^{2+}$, Dy^{3+} and $SrAl_2O_4:Eu^{2+}$, Mn^{2+}, Dy^{3+} phosphors were synthesized by combustion method in a muffle furnace at an initiating temperature of 600 ^oC. The phase and crystallinity of the samples were investigated using an X'Pert PRO PANalytical diffractometer with CuKα at λ = 0.15405 nm. The particle morphologies of the powders were investigated using a JEOL JSM-

7500F field-emission scanning electron microscope (FE-SEM). The photoluminescence (PL) spectra were recorded at room temperature using a Jobin Yvon/SPEX Fluorolog spectrofluorometer (Model FL-1057) equipped with a 450 W Xenon light source, double excitation and emission monochromators, and R928 PMT detector. TL spectra were recorded using a Riso TL/OSL reader (Model DA-20).

4.3. Results and discussions

4.3.1. Surface Morphology

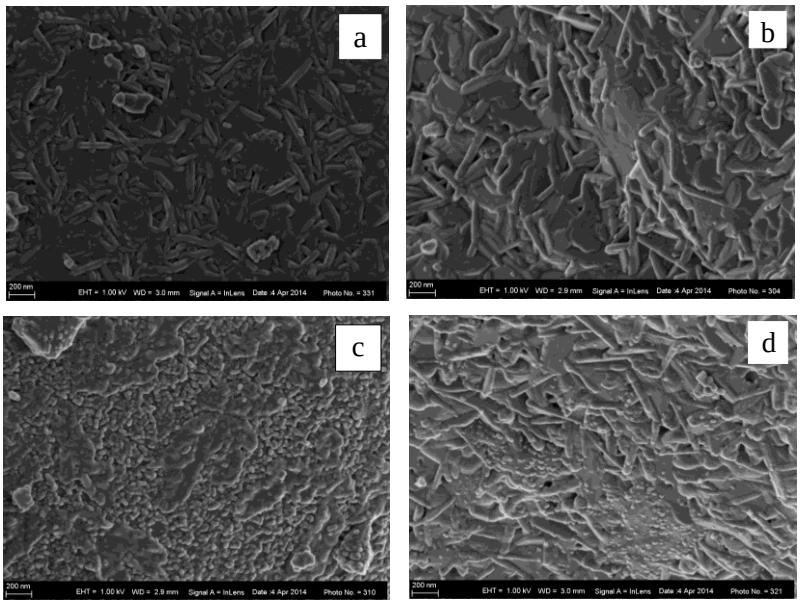

Figure 4.1: SEM images of the as-synthesised (a) $SrAl_2O_4$, (b) $SrAl_2O_4:Eu^{2+}$, (c) $SrAl_2O_4:Dy^{3+}$, and (d) $SrAl_2O_4:Mn^{2+}$ phosphors**.**

Figure 4.1 shows SEM micrographs of the as-synthesized $SrAl_2O_4$, $SrAl_2O_4:Eu^{2+}$, $SrAl_2O_4:Dy^{3+}$, and $SrAl_2O_4:Mn^{2+}$ phosphors taken at a magnification of X 50 000. The SEM micrographs revealed irregular shaped particle structures. The pores and cracks observed in some of the images can be attributed to escaping gases during combustion process.

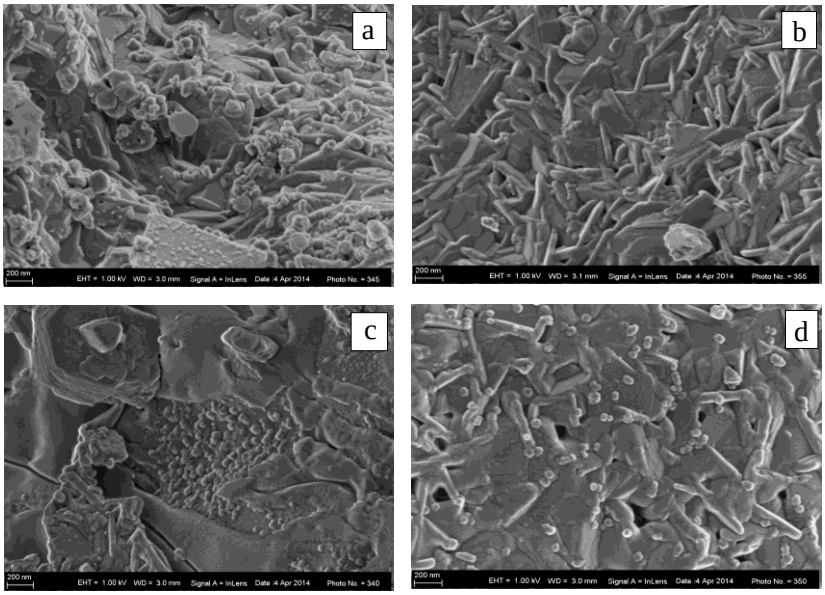

Figure 4.2: SEM images of the as-synthesised (a) $SrAl_2O_4:Eu^{2+}$, Dy^{3+} ,(b) $SrAl_2O_4:Eu^{2+}$, Mn^{2+},(c) $SrAl_2O_4:Dy^{3+}$, Mn^{2+}, (d) $SrAl_2O_4:Eu^{2+}$,Mn^{2+}, Dy^{3+}phosphors.

Figure 4.2 shows SEM micrographs of the as-synthesized $SrAl_2O_4:Eu^{2+}$, Dy^{3+}, $SrAl_2O_4:Eu^{2+}$, Mn^{2+}, $SrAl_2O_4:Dy^{3+}$, Mn^{2+} , and $SrAl_2O_4:Eu^{2+}$,Mn^{2+}, Dy^{3+} phosphors taken at a magnification of X 100 000. All samples exhibit irregular shaped structures. The pores and cracks are due to escaping gases during combustion, which favors conditions for the formation of nano-crystalline materials [6], namely sintering of the phosphor is avoided due to the dispersion of heat by escaping gases during combustion [6].

4.3.2. Structural Properties

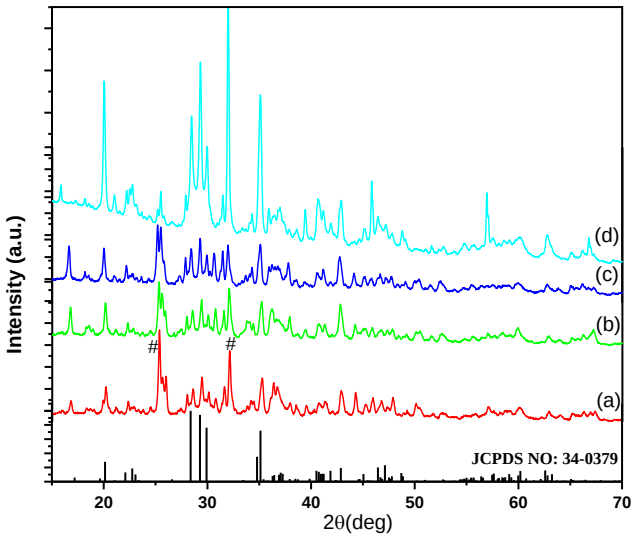

Figure 4.3: X-ray diffraction (XRD) patterns of the as-prepared phosphors (a) $SrAl_2O_4:Eu^{2+}$, (b) $SrAl_2O_4:Mn^{2+}$, (c) $SrAl_2O_4:Dy^{3+}$ and (d) $SrAl_2O_4:Dy^{3+}$ annealed at 1200 ^oC for 2 hours .

Figure 4.3 shows the crystal structure of the as-prepared $SrAl_2O_4:Eu^{2+}$, $SrAl_2O_4:Mn^{2+}$, $SrAl_2O_4:Dy^{3+}$, and the annealed $SrAl_2O_4:Dy^{3+}$ phosphors prepared by combustion method. All the main peaks reflect typical XRD patterns of the α (monoclinic) phase of $SrAl_2O_4$ according to the JCPDS card number 34-0379, except the diffraction peaks marked with a hash that did not match with the α monoclinic phase of $SrAl_2O_4$. The XRD results of the as-perepared smples doped with Eu^{2+}, Dy^{3+}, and Mn^{2+} shows similar results,which implies that the dopants has no effect on the phase composition. Since all these peaks still appear even after annealing, they are not associated with the excess of urea in these samples.

The impurity phases observed in all the samples are related to $Sr_3Al_2O_6$ impurity phases , and similar results have been reported in the literature [7,8]. The results suggest that some of the precursors did not react completely to form crystalline phases of $SrAl_2O_4$ phosphors. A closer observation also confirms a small shift of the diffraction peaks. Eu^{2+} and Dy^{3+} doping induce peak shift towards lower 2θ angles while Mn^{2+} doping shifts peaks towards higher angles. The peak shifts are attributed to the strains induced when Sr^{2+} is substituted by Mn^{2+}, Eu^{2+} and Dy^{3+}

during doping of the $SrAl_2O_4$ lattice [9]. Due to its small ionic radii compared to Sr^{2+} (0.112 nm), Mn^{2+} (0.080 nm) induces a lattice shrinkage when occupying the Sr^{2+} sites during substituting, hence a shift towards higher angles [9]. Eu^{2+} (0.130 nm) and Dy^{3+} (0.117 nm) have larger ionic radii relative to Sr^{2+}. When the two rare earths substitute Sr^{2+}, a lattice expansion is induced, hence a shift of the peaks towards lower 2θ angles. The average crystallite size was estimated using equation 4.1 known as Scherrer's formular [10].

$$D = \frac{k\lambda}{B\cos\theta} \qquad (4.1)$$

Where D is the crystallite size, B is the full width at half maximum height of the diffraction peak; λ is the X-ray wavelength, θ (theta) is the Bragg's angle, k is constant (0.94). The crystallite sizes were estimated to be 31.3 nm, 32.4 nm, 27.7 nm and 19.1 nm for the undoped $SrAl_2O_4$, $SrAl_2O_4$:Eu^{2+}, $SrAl_2O_4$:Dy^{3+} and $SrAl_2O_4$:Mn^{2+} phosphors respectively.

4.3.3. Optical Properties

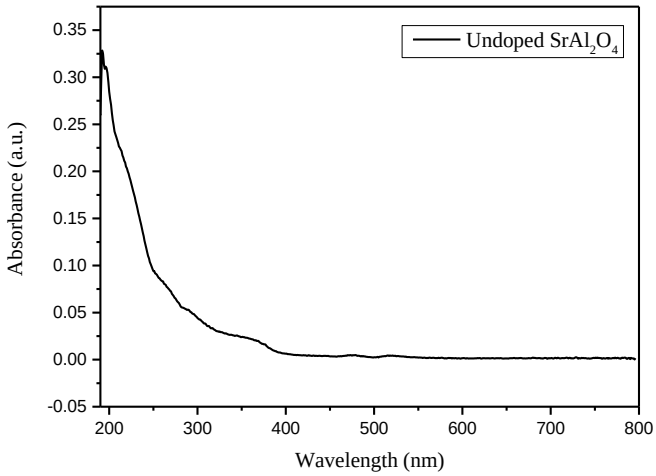

Figure 4.4: UV-Vis Absorption spectrum of un-doped $SrAl_2O_4$ with absorption edge at 210 nm.

Figure 4.4 shows the room temperature absorption spectrum of the un-doped $SrAl_2O_4$ sample. The spectrum shows weak broad bands between 210 nm and 400 nm. These bands may be attributed to structural defects in the $SrAl_2O_4$ sample [11]. No absorption bands above 400 nm

were observed. Above this wavelength, the $SrAl_2O_4$ sample is not easy to excite due to the wideness of its band-gap [11]. In this work, the fundamental absorption (valence band to conduction band transition) was observed at 210 nm.

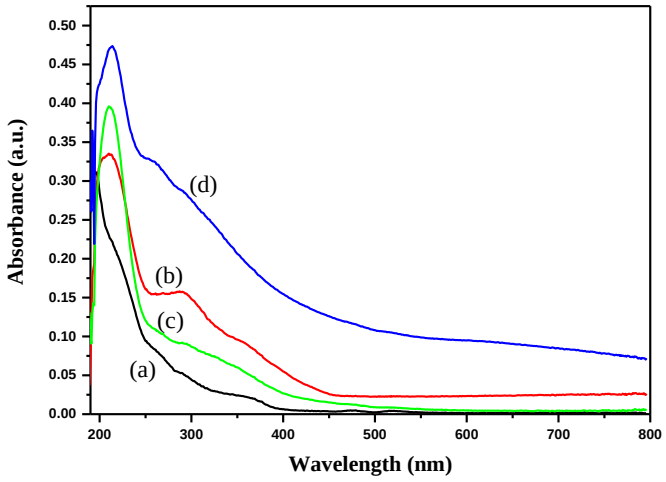

Figure 4.5: UV-Vis Absorption spectra of un-doped (a) $SrAl_2O_4$, (b) $SrAl_2O_4:Eu^{2+}$, (c) $SrAl_2O_4:Dy^{3+}$, and (d) $SrAl_2O_4:Mn^{2+}$ phosphors.

Figure 4.5 shows the absorption spectra of the un-doped $SrAl_2O_4$ phosphor and $SrAl_2O_4$ phosphors doped with Eu^{2+}, Dy^{3+} and Mn^{2+} ions in the spectral region between 180 to 800 nm. Compared to the un-doped $SrAl_2O_4$ phosphor, it was observed that after doping, the absorption edge shifts to longer wavelengths. This actually suggests a decrease in band gap in doped phosphors. The results also show that the absorbance intensities are higher in doped phosphors compared to the undoped $SrAl_2O_4$ phosphor. This could be a result of an increased absorption of photon energy in the longer wavelengths due to a reduced band gap.

The absorption profile of $SrAl_2O_4$: Eu^{2+} also exhibit additional bands between 250 nm to 450 nm, which are attributed to the $4f^6 5d^1 \rightarrow 4f^7$ absorption of the Eu^{2+} ions. The phosphor samples doped with Dy^{3+} and Mn^{2+} ions also have broad bands between 250 nm to 500 nm, but these are weak bands compared to those shown by Eu^{2+} doped sample. The observed weak band

could be related to the forbidden transitions 4f-4f for $SrAl_2O_4$: Dy^{3+} and ${}^4T_1({}^4G) \rightarrow {}^6A_1({}^6S)$ for $SrAl_2O_4$: Mn^{2+} phosphor.

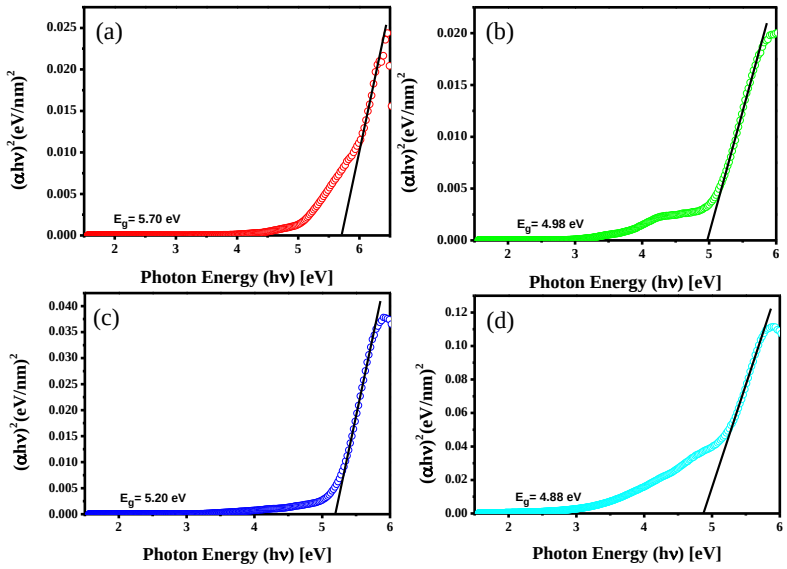

Figure 4.6: Tauc Plots for band gap estimations from the absorption spectra of (a) un-doped $SrAl_2O_4$, (b) $SrAl_2O_4$:Eu^{2+}, (c) $SrAl_2O_4$:Dy^{3+}, and (d) $SrAl_2O_4$:Mn^{2+} phosphors.

The optical energy band gap (E_g) of the un-doped $SrAl_2O_4$ phosphor and the $SrAl_2O_4$ phosphors doped with Eu^{2+}, Dy^{3+} and Mn^{2+} ions were estimated using the Tauc relation [7].

$$(\alpha h\nu)^2 = K^2(h\nu - E_g) \qquad (4.2)$$

Where α is the absorption coefficient, $h\nu$ is the photon energy, K is a constant that depends on the type of transition, E_g is the band gap. The band gap energy is estimated by plotting $(\alpha h\nu)^2$ vs $h\nu$ in the high absorption range followed by the extrapolation of linear region of the plot to $(\alpha h\nu)^2 = 0$ as shown in Figure 4.6. A point where the extrapolation of the linear region of the plot intersects the $h\nu$ axis is taken as the band gap value. The estimated band gap values were found to be 5.70 eV, 4.98 eV, 5.20 eV, and 4.88 eV for the un-doped $SrAl_2O_4$ phosphor, Eu^{2+}

doped phosphor, Dy^{3+} phosphor, and Mn^{2+} doped phosphor respectively. The results clearly, show a decrease in band gap after doping with Eu^{2+}, Dy^{3+} and Mn^{2+}ions.

A decrease in the band gap is attributed to the localized defect levels induced within the band to band gap of the $SrAl_2O_4$ host by doping with Eu^{2+}, Dy^{3+} and Mn^{2+}ions [12]. The difference in the extents to which the bandgap decreases after doping is attributed to the difference in ionic radii of the dopants [13]. When a large ion such as Eu^{2+} (ionic radius = 0.13 nm) substitutes a small ion such as Sr^{2+} (radius = 0.127 nm) in the $SrAl_2O_4$ lattice, lattice expansion is expected due to the difference in their ionic radii. In contrary, the contraction of the lattice is expected when Sr^{2+} is replaced by small ions such as Dy^{3+} (ionic radius = 0.091 nm) and Mn^{2+} (ionic radius = 0.080 nm) [13]. These lattice contraction and expansion have an effect on the band structure of the $SrAl_2O_4$ lattice, and the value of the band gap.

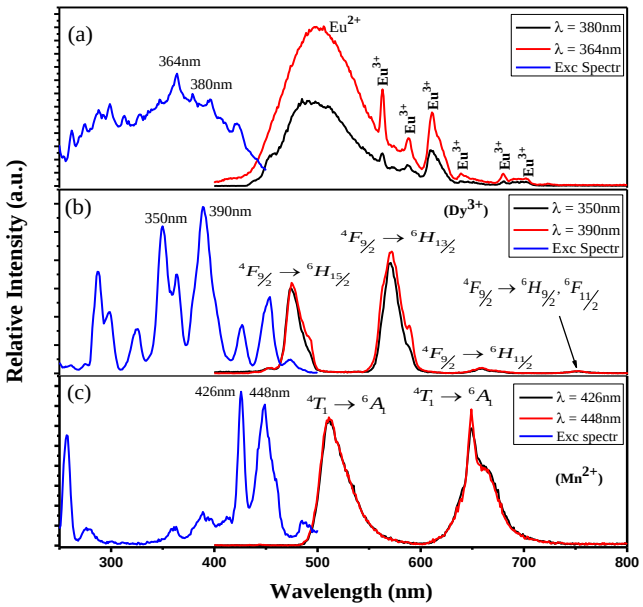

Figure 4.7: Excitation and Emission of the as-prepared $Sr_{0.99}Al_2O_4:Eu^{2+}{}_{0.01}$ (a) and (b), $Sr_{0.98}Al_2O_4:Dy^{3+}{}_{0.02}$ and (c), $Sr_{0.98}Al_2O_4:Mn^{2+}{}_{0.02}$ phosphors prepared by combustion method.

Figure 4.7 shows the photoluminescence excitation (PLE) spectra on the left and photoluminescence emission (PL) spectra on the right of $SrAl_2O_4$ doped with different rare earth ions. A broad blue to green emission band peaking at 500 nm on the emission spectrum of figure

4.7(a) ascribed to the $4f^6 5d^1 \rightarrow 4f^7$ transition of the Eu^{2+} ion was observed [14]. The red sharp emission lines at 563 nm, 588 nm, 611 nm, 680 nm and 702 nm are due to the crystal field-insensitive 4f to 4f transitions of the Eu^{3+} ion that is present in the sample. Eu^{3+} emission lines are assigned to transitions from $^5D_0 \rightarrow {}^7F_J$ (J= 0, 1, 2, 3, 4) [15]. The hypersensitive 611nm emission peak is very intense than the other Eu^{3+} peaks. The hypersensitivity of this peak is attributed to the electric dipole nature of the $^5D_0 \rightarrow {}^7F_2$ transition [16].

Figure 4.7(b) shows the emission and excitation spectra of $Sr_{0.98}Al_2O_4:Dy^{3+}{}_{0.02}$ phosphor prepared by combustion method. The emission spectrum in Figure 4.7(b) consists of two strong emissions peaks, namely: the blue line emission at 475 nm, and the green line emission at 575 nm, together with a weak red emission line at 659 nm. The blue emission line, the yellow intense emission line, and the weak red emission line are assigned to the $^4F_{9/2} \rightarrow {}^6H_{15/2}$, $^4F_{9/2} \rightarrow {}^6H_{13/2}$, and $^4F_{9/2} \rightarrow {}^6H_{11/2}$ transitions of the Dy^{3+} respectively [17]. In addition, the yellow emission line at 575 nm due to the hypersensitive $^4F_{9/2} \rightarrow {}^6H_{13/2}$ transition in the emission spectrum is dominant, as compared to the blue emission line at 475nm due to the crystal field insensitivity of the magnetic dipole $^4F_{9/2} \rightarrow {}^6H_{15/2}$ transition [18]. The dominance of the yellow emission line suggests that the Dy^{3+} ions occupy sites with low symmetry; otherwise the blue emission line would dominate in the emission spectrum [18].

Figure 4.7(c) shows the PL emission and excitation spectrum of $Sr_{0.98}Al_2O_4:Mn^{2+}{}_{0.02}$ phosphor prepared by combustion method. The emission spectrum consists of two broad bands centered at 513 nm and 650 nm. Both green and orange/red emission peaks are assigned to the typical $^4T_1(^4G) \rightarrow {}^6A_1(^6S)$ transition of the Mn^{2+} ion [17]. The two different emissions due to the same transition can be explained by the ability of the Mn^{2+} ion to occupy both tetrahedral and octahedral sites in the host lattice [19]. Tetrahedral sites are characterized by weaker crystal fields i.e. D_q (tetrahedral) = $4/9D_q$ (octahedral) [19], therefore the d orbital of Mn^{2+} ion is split less in tetrahedral sites. This usually results in the energies of all transitions in these sites to rise and show emissions in the short part of the spectrum (513 nm in this work) [20].

In contrast, the d orbital of the Mn^{2+} ion is split more in the octahedral sites and transitions in these sites show emissions in the longer part of the spectrum (650 nm in this work). In addition, a considerable spectral overlap between the $SrAl_2O_4:Eu^{2+}$ emission spectrum and the $SrAl_2O_4:Mn^{2+}$ excitation spectrum was observed which confirms an effective energy transfer from Eu^{2+} to Mn^{2+}.

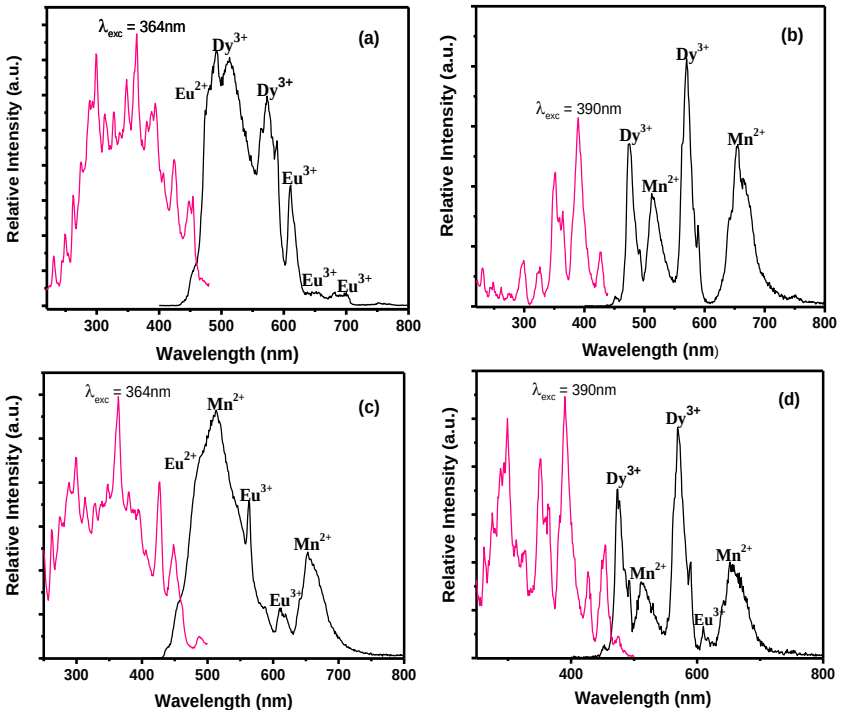

Figure 4.8: PL excitation spectra (red lines) and emission spectra (black lines) of (a): $SrAl_2O_4$: Eu^{2+}, Dy^{3+}; (b): $SrAl_2O_4$: Mn^{2+}, Dy^{3+}; and (c): $SrAl_2O_4$: Eu^{2+}, Mn^{2+}, Dy^{3+} phosphors.

Figure 4.8 shows excitation spectra (red) and the emission spectra (black) of $SrAl_2O_4$: Eu^{2+}, Dy^{3+}; $SrAl_2O_4$: Mn^{2+}, Dy^{3+}; $SrAl_2O_4$: Eu^{2+}, Mn^{2+}; and $SrAl_2O_4$: Eu^{2+}, Mn^{2+}, Dy^{3+}. The sample in Figure 4.8(a) was excited with the highest excitation peak of the excitation spectrum at 364 nm as shown on the left hand side of the figure. The emission spectrum has two sharp peaks at 492 nm and 513 nm. These peaks are attributed to the $^4F_{9/2} \rightarrow {}^6H_{15/2}$ transition of the Dy^{3+} ion due to their sharpness. However, there is also some broadening contribution on these peaks from the

Eu^{2+} ion as shown on the figure. A sharp peak at 575 nm is also observed and this peak is attributed to the $^4F_{9/2} \rightarrow {}^6H_{13/2}$ transition of the Dy^{3+} ion [21]. The remaining sharp lines on the spectrum at 611 nm, 652 nm, 682 nm, and 702 nm are the characteristic emission lines of Eu^{3+} , which are due to the 4f to 4f transitions of the Eu^{3+} [21].

Figure 4.8(b) shows the emission spectrum with its excitation spectrum of $Sr_{0.96}Al_2O_4{:}Mn^{2+}{}_{0.02}, Dy^{3+}{}_{0.02}$ phosphor powder. The sample was excited at 390 nm as shown on the figure. The emission spectrum consists of both Dy^{3+} and Mn^{2+} emissions, with Dy^{3+} emission lines at 475 nm and 570 nm, and Mn^{2+} broad bands at 512 nm and 655 nm. The Dy^{3+} emission lines are ascribed to its 4f to 4f transitions, and the Mn^{2+} bands are attributed to the $^4T_1(^4G) \rightarrow {}^6A_1(^6S)$ transition. The Dy^{3+} peaks are more intense than the Mn^{2+} as shown in the figure.

In Figure 4.8(c), the $Sr_{0.96}Al_2O_4{:}Mn^{2+}{}_{0.02}, Eu^{2+}{}_{0.02}$ sample was excited with 364 nm excitation wavelength. The emission spectrum consists of Eu^{2+}, Eu^{3+}, and Mn^{2+} emission peaks. The broad emission peak at 512 nm is attributed to the $^4T_1(^4G) \rightarrow {}^6A_1(^6S)$ transition of the Mn^{2+} ion [22]. This peak also shows a more broadening in shape compared to the $Sr_{0.98}Al_2O_4{:}Mn^{2+}{}_{0.02}$ sample, and this broadening is due to a contribution from the Eu^{2+} ion. It is worth noting that the broad emission peak of the $SrAl_2O_4$: Eu^{2+} phosphor extends over the blue region of the spectrum,where the $SrAl_2O_4$: Mn^{2+} sample shows a high absorption.

In other words the $SrAl_2O_4$: Eu^{2+} broad emission spectrum ranging from 430 nm to 558 nm overlaps the $SrAl_2O_4$: Mn^{2+} excitation spectrum from 455 nm to 500 nm, therefore part of the Eu^{2+} emission is re-absorbed by the Mn^{2+} ion, which is according to Forster-Dexter theory of non-radiative energy transfer [23], a clear evidence of an efficient energy transfer from the Eu^{2+} ion to the Mn^{2+} ion in the $SrAl_2O_4$: Eu^{2+}, Mn^{2+} powder phosphor, and this energy transfer will be illustrated later in this chapter.

Moreover, the intensity of the yellow-red Mn^{2+} emission peak in Figure 4.8(c) increased considerably compared to the one in the $SrAl_2O_4$: Mn^{2+} phosphor. This can be ascribed to the

spin forbidden absorption transitions in the Mn^{2+} singly doped sample in Figure 4.7 as compared to the $SrAl_2O_4$: Eu^{2+}, Mn^{2+} phosphor with a sensitizing effect from Eu^{2+} ion. The sensitizing effect comes from the matching of the excited states of Mn^{2+} ion with some excited energy levels of the Eu^{2+} ion and this is illustrated as the inverse bottleneck later in this section [22]. Two sharp emission lines at 563 nm and 611 nm together with a shoulder at 588 nm which are ascribed to the 4f to 4f transitions of the Eu^{3+} were also observed in Figure 4.8 (c).

Figure 4.8(d) shows the emission and the excitation spectrum of $Sr_{0.95}Al_2O_4{:}Eu^{2+}{}_{0.01}Mn^{2+}{}_{0.02}, Dy^{3+}{}_{0.02}$ phosphor. The sample was excited at 390 nm wavelength as shown on the excitation spectrum. The emission spectrum consisted of emissions from Dy^{3+}, and Mn^{2+} ions together with the one from small traces of Eu^{3+} which remained when urea converted Eu^{3+} to Eu^{2+} during combustion. The emission bands from the Eu^{2+} ion were not detected in the sample. The reason of not observing any emission from the Eu^{2+} ion could be that, the excitation wavelength (390 nm) used to excite this material does not effectively ionize the Eu^{2+} ions in this material. Another possibility is that Eu^{2+} might be acting as a sensitizer and transferring its energy to the Mn^{2+} in this material, and this is supported by the overlap between the Eu^{2+} emission spectrum and the Mn^{2+} excitation spectrum as discussed latter in this section.

The Dy^{3+} emission lines centered at 475 nm and 575 nm are more intense, while the less intense Mn^{2+} emission bands are observed at 512 nm and 655 nm. Higher intensities of the Dy^{3+} peaks are a result of the excitation wavelength (390 nm) used favouring the Dy^{3+} ions i.e. Dy^{3+} ions are well excited at 390 nm as shown in Figure 4.7. A weak red emission line, ascribed to the transition of the Eu^{3+}, is at 611 nm [20]. The Dy^{3+} and Eu^{3+} emissions are due to the 4f to 4f transitions [21], and the Mn^{2+} emissions are due to the $^4T_1(^4G) \rightarrow {}^6A_1(^6S)$ transition [21]. There was no emission peak shift observed on all the co-doped samples as compared to their corresponding singly doped phosphors, except in the case of Dy^{3+} emission at 575 nm which showed a 5 nm blue shift. This is due to a transition which is very sensitive to the crystal field; therefore the observed blue shift could be a result of a slight change in crystal field due to doping by all three dopants.

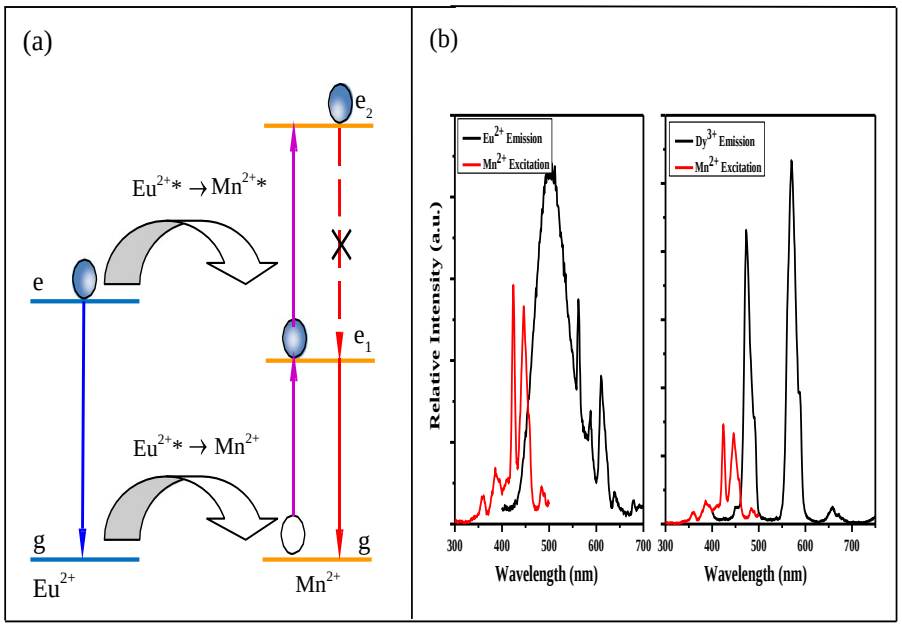

Figure 4.9: Schematic illustration of energy transfer via the inverse bottleneck (a), and via spectral overlap (b). The transition in (a) marked with an "*" is a non-radiative transition [24].

In the "inverse bottleneck" [24] process depicted in Figure 4.9 (a), e, g, Eu^{2+}*, and Mn^{2+}* are excited state, ground state, excited Eu^{2+}, and excited Mn^{2+} respectively. The process first starts by energy transfer from Eu^{2+}* to the ground state (g) of Mn^{2+}. As the material is continuously excited, the population of Mn^{2+}* at e_1 increases, and this excitation can go further to higher excited state e_2, which results in the enhancement of Eu^{2+} to Mn^{2+} energy transfer [24].

Figure 4.9 (b) shows spectral overlaps as evidence of energy transfer from a sensitizer to an activator. According to Forster-Dexter theory of non-radiative energy transfer[23,22], if there is an overlap between the excitation spectrum of an activator and the emission spectrum of the sensitizer, then there exists a non-radiative energy transfer from a sensitizer to an activator.

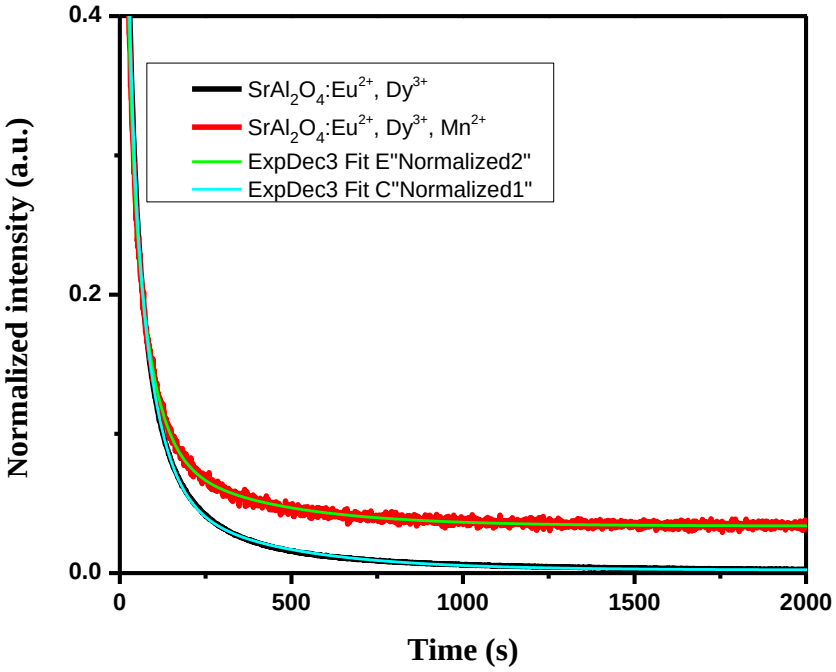

Figure 4.10: Decay curves of $SrAl_2O_4:Eu^{2+}$, Dy^{3+}, $SrAl_2O_4:Mn^{2+}$, Dy^{3+}, $SrAl_2O_4:Eu^{2+},Mn^{2+}$ **,** and $SrAl_2O_4:Eu^{2+},Mn^{2+}$, Dy^{3+} phosphors.

In order to characterize afterglow phosphors, the exponential decays of such materials need to be studied. Typically, when the excitation is ceased, the emission intensity decays rapidly and followed by long time lasting phosphorescence. The decay curves of $SrAl_2O_4:Eu^{2+}$, Dy^{3+} and $SrAl_2O_4:Eu^{2+}$, Dy^{3+}, Mn^{2+} phosphors are shown in Figure 4.10 and the ones for $SrAl_2O_4:Eu^{2+}$, Mn^{2+} and $SrAl_2O_4:Mn^{2+}$, Dy^{3+} are shown in Figure 4.11. The $SrAl_2O_4:Eu^{2+}$, Dy^{3+} and $SrAl_2O_4:Eu^{2+}$, Mn^{2+} samples were irradiated with a 364 nm UV light from a xenon lamb for 5 minutes at room temperature while $SrAl_2O_4:Mn^{2+}$, Dy^{3+} and $SrAl_2O_4:Eu^{2+}$, Dy^{3+}, Mn^{2+} phosphors were irradiated at 390 nm from the same light source for 5 minutes at room temperature. It is clear that phosphors in Figure 4.10 show a long persistence and those in Figure 4.11 show short time persistence.

It has been reported in many Eu^{2+}, Dy^{3+} co-doped phosphors that the Eu^{2+} ion plays a role of a luminescent center and Dy^{3+} ion acts as a trapping center and extends the duration of

phosphorescence [25]. However there are still contradictions [26, 27] about whether the Dy^{3+} ion forms electron-trapped defect in these types of phosphors i.e. an electron moves in the conduction band of the host matrix and later get trapped in the Dy^{3+} energy states or hole-trapped defect i.e. hole transport in the valence band and later gets trapped in the Dy^{3+} energy states. In other words, further studies still need to be done to arrive at the correct long afterglow mechanism in these types of phosphors.

The $SrAl_2O_4:Eu^{2+}$, Dy^{3+}, Mn^{2+} phosphor shows a longer persistence than all the phosphors including the well-known long persistent $SrAl_2O_4:Eu^{2+}$, Dy^{3+} phosphor. This may be due to the introduction of Mn^{2+} ion into the $SrAl_2O_4:Eu^{2+}$, Dy^{3+} phosphor. In the $SrAl_2O_4:Eu^{2+}$, Dy^{3+}, Mn^{2+} phosphor, the Dy^{3+} ion is known to create traps from which energy is transferred to the luminescent centers Eu^{2+} and Mn^{2+} ions [28]. At the same time Mn^{2+} ion receives energy from the Eu^{2+} ion via a persistent energy transfer between the two ions, which results in a longer persistent luminescence in the $SrAl_2O_4:Eu^{2+}$, Dy^{3+}, Mn^{2+} phosphor. Similar observations have been reported by Wang et al. [29] on the $MgSiO_3:Mn^{2+}$, Eu^{2+}, Dy^{3+} material and Gong et al. [30] on the $Sr_{3-x}Mg_{1-y}Si_2O_8:xEu^{2+}$, yMn^{2+}, $_{0.01}Dy^{3+}$ material.

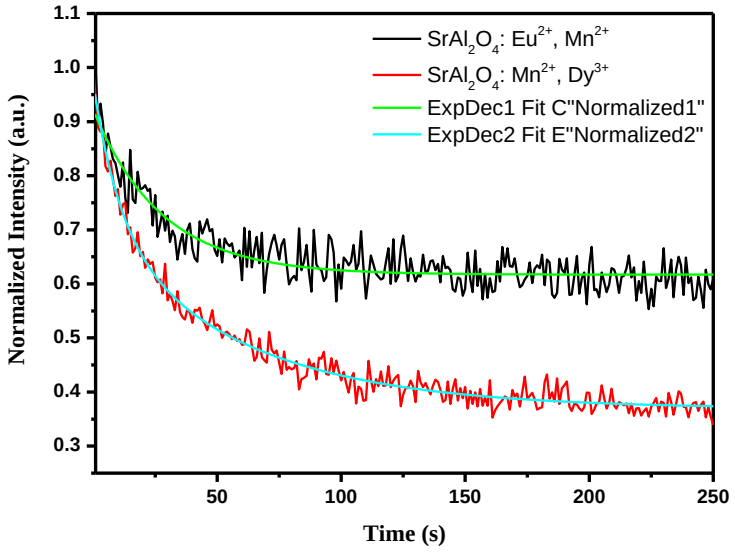

Figure 4.11: Decay curves of $SrAl_2O_4:Mn^{2+}$, Dy^{3+} and $SrAl_2O_4:Eu^{2+}$,Mn^{2+} phosphors.

In Figure 4.11, the persistence of the $SrAl_2O_4:Eu^{2+}$, Mn^{2+} phosphor is longer than that of $SrAl_2O_4:Mn^{2+}$, Dy^{3+} phosphor. In both Eu^{2+}, Mn^{2+} and Dy^{3+}, Mn^{2+} co-doped materials, the Mn^{2+} ion is sensitized by both Eu^{2+} and Dy^{3+} ions. However, the degree of spectral overlap is not the same for both materials as shown in Figure 4.9 (b). It is large between Eu^{2+} (sensitizer) emission spectrum and Mn^{2+} (activator) excitation spectrum compared to the one between Dy^{3+} emission spectrum and Mn^{2+} excitation spectrum. Hence, there exists a more persistent energy transfer [31] from Eu^{2+} to Mn^{2+} than from Dy^{3+} to Mn^{2+} which results in the $SrAl_2O_4:Eu^{2+}$, Mn^{2+} system to have more persistent luminescence than the $SrAl_2O_4:Dy^{3+}$, Mn^{2+} system.

The emission decay curves of all the above phosphors show single exponential decay profiles with the exception of $SrAl_2O_4:Eu^{2+}$, Dy^{3+}. This phosphor shows first a fast decaying process at the beginning and a subsequent slow decaying process, and a similar work was reported in literature [32]. The short time decaying process is a result of the intrinsic lifetime of the Eu^{2+} ion, and the long-time decaying process is due to deep energy centers of Dy^{3+} [33]. Moreover the

decay times of the $SrAl_2O_4:Eu^{2+}$, Mn^{2+},Dy^{3+} and $SrAl_2O_4:Eu^{2+}$, Dy^{3+} phosphors were found by fitting the decay curves with a third order exponential equation 4.4.

$$I = A_1 e^{\frac{-t}{\tau_1}} + A_2 e^{\frac{-t}{\tau_2}} + A_3 e^{\frac{-t}{\tau_3}} \qquad (4.4)$$

Where I is the phosphorescence intensity at any time t after the excitation was ceased, A_1, A_2, A_3 are constants, and τ_1, τ_2, and τ_3 are decay times for the exponential components. The decay parameters of $SrAl_2O_4:Eu^{2+}$, Mn^{2+}, Dy^{3+} and $SrAl_2O_4:Eu^{2+}$, Dy^{3+} phosphors are tabulated in table 4.1.

Table 4.1: Decay parameters of the as-synthesized $SrAl_2O_4:Eu^{2+}$, Dy^{3+} and $SrAl_2O_4:Eu^{2+}$, Mn^{2+}, Dy^{3+} phosphors.

Decay times (s)	***$SrAl_2O_4:Eu^{2+},Dy^{3+}$***	***$SrAl_2O_4:Eu^{2+}, Mn^{2+},Dy^{3+}$***
τ_1	9.22	10.78
τ_2	38.49	42.93
τ_3	218.22	229.57

The decay profiles of $SrAl_2O_4:Eu^{2+}$, Mn^{2+} phosphors was found by fitting the decay curve with a single exponential equation 4.5, and the decay time was found to be $\tau = 17.92$ seconds.

$$I = A_1 e^{\frac{t}{\tau}} \qquad (4.5)$$

The decay curve of $SrAl_2O_4:Mn^{2+}$, Dy^{3+} phosphor was fitted by the second exponential equation 4.6.

$$I = A_1 e^{\frac{-t}{\tau_1}} + A_2 e^{\frac{-t}{\tau_2}} \qquad (4.6)$$

The decay times of this phosphor was found to be $\tau_1 = 6.34$ seconds, and $\tau_2 = 37.33$ seconds.

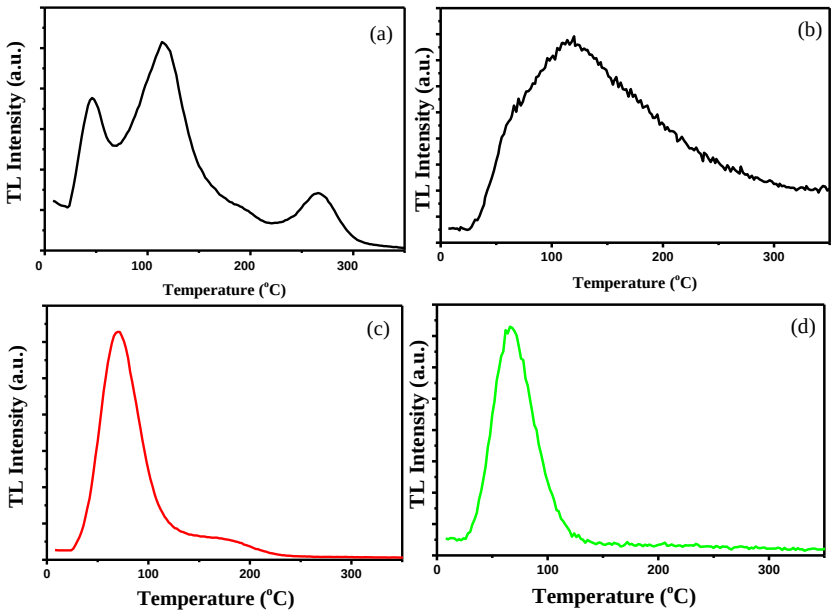

Figure 4.12: Thermoluminescence spectra of (a) undoped $SrAl_2O_4$, (b) $SrAl_2O_4:Eu^{2+}$, (c) $SrAl_2O_4:Dy^{3+}$, (d) $SrAl_2O_4:Mn^{2+}$.

Thermoluminescence (TL) studies were carried out in order to study the traps (electron/hole) properties that are responsible for the persistent luminescence phenomena in the un-doped $SrAl_2O_4$, $SrAl_2O_4:Eu^{2+}$, $SrAl_2O_4:Dy^{3+}$ and $SrAl_2O_4:Mn^{2+}$ phosphors. It is supposed in this work that exposure of these materials to a beta source generates electron-hole pairs. The electrons are believed to be trapped at electron traps close to the conduction band. A subsequent thermal liberation of these electrons into the conduction band is followed by a slow radiative recombination of these electrons with trapped holes at the luminescence centre, resulting in a persistent luminescence [34].

During sample heating, it is also possible for holes in hole traps close to the valence band to be thermally liberated into the valence band. A slow recombination of these holes with electrons in the luminescence centre usually results in a persistent luminescence [34]. TL glow curves of the un-doped $SrAl_2O_4$, $SrAl_2O_4:Eu^{2+}$, $SrAl_2O_4:Dy^{3+}$ and $SrAl_2O_4:Mn^{2+}$ phosphors are shown in Figure 4.13. In order to obtain a well-defined TL signals from these materials, it was necessary to use different parameters. For instance, $SrAl_2O_4$ gives a well-defined spectrum at low dose and low heating rate, while the doped materials respond very poorly under these conditions.

The $SrAl_2O_4$ sample was exposed to a 100 seconds dose from a beta (β) source (0.1028 Gs/s) prior to TL measurements and heated at a linear heating rate of $1^oC/s$. $SrAl_2O_4:Eu^{2+}$, $SrAl_2O_4:Dy^{3+}$ and $SrAl_2O_4:Mn^{2+}$ were given 500 seconds dose from the same source and heated at a linear heating rate of $3\ ^oC/s$. All the TL measurements were performed in the range from room temperature to 500 ^oC. However, the rising part above 350 ^oC, which is due to black body radiation, was omitted during plotting.

The un-doped $SrAl_2O_4$ sample consists of strong low temperature peaks at 46 ^oC and 114 ^oC, and weak bands at 186 ^oC, and 266 ^oC as shown in Figure 4.12 (a). Ayvacikli et al [6] also reported four TL peaks on un-doped $SrAl_2O_4$ phosphor. However, their observed TL peaks were not at the same positions as the ones reported in this work. The difference in peak positions could be attributed to the difference in the synthesis method or particle size. It is known that when there are different glow peaks at different positions, electrons or holes were thermally released from different types of traps, and each with distinct activation energy [35]. The TL peaks in Figure 4.12 (a) could be associated with the intrinsic defects such as Frenkel and Schottky defects in the $SrAl_2O_4$ matrix namely: oxygen vacancy (V_O), strontium vacancy (V_{Sr}), and aluminium vacancy (V_{Al}) [36].

A rather complex broad band that peaked at 120 ^oC was observed in Figure 4.12 (b). The broad nature of this glow curve suggests a possibility that a glow curve consists of closely overlapping TL peaks, which could be due to a continuous distribution of traps in this material [37, 38]. Also, the fact that Figure 4.12 (b) does not consist of a single TL peak could be an indication that different sets of traps are distributed separately and each with a distinct depth in this phosphor [39]. A prominent low temperature peak at 70 ^oC, and a weak peak at 180 ^oC were observed in Figure 4.12 (c). These TL peaks could be an evidence of the existence of shallow and deep traps in the $SrAl_2O_4:Dy^{3+}$ phosphor [40].

A high intensity peak at 70 ^oC suggests that more electrons were promoted into shallow traps than into deep traps in this material during beta irradiation [41]. As depicted in Figure 4.13, thermoluminescence process in the $SrAl_2O_4:Dy^{3+}$ phosphor starts from exposure of this material to a 500 seconds beta dose (path i). A large fraction of this excitation energy is transferred

directly to the emitting centre Dy^{3+}, i.e. electrons migrate through the conduction band directly into excited states of the emitting centre Dy^{3+}, while holes tunnel through the valence band to the ground state of Dy^{3+} (path ii).

It is well known that recombination of these electrons from the conduction band (without getting trapped) with the holes from the valence band at the emitting centre gives out energy as photoluminescence. It is known that Dy^{3+} ions tend to replace Sr^{2+} ions when doping $SrAl_2O_4$ matrix with Dy^{3+} ions due to similarities in ionic radii. Another fraction of excitation energy is stored in this material when some electrons decay from the conduction band into the electron traps (path iii). Heating of the sample liberates these electrons from traps into the conduction band (iv), and this is followed by a recombination of the liberated electrons with holes at emitting centre which gives out energy as thermoluminescence.

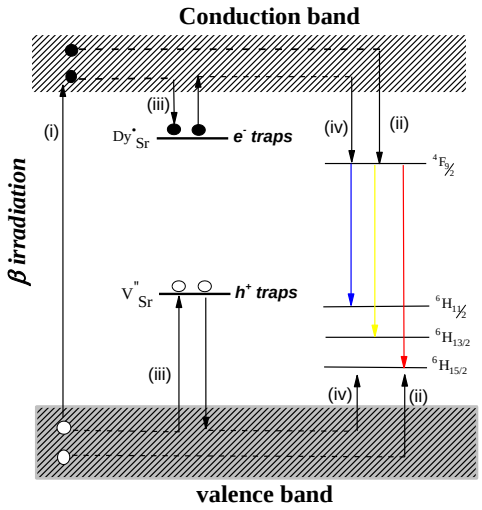

Figure 4.13: A schematic representation of TL mechanism in Dy^{3+} doped $SrAl_2O_4$ [42].

It is clear from Figure 4.12(d) that the as-prepared $SrAl_2O_4:Mn^{2+}$ phosphor exhibited only a single TL peak at 66 ^oC. This indicates that only one type of traps is activated in this phosphor [43]. Haghiri et al. [44] also reported a single TL peak at 150 ^oC on a manganese doped calcium tetraborate. The difference in peak positions could be associated with the difference in host materials as the manganese ion is well known to be very sensitive to the sounding environment.

It should be noted that the un-doped $SrAl_2O_4$ phosphor has four TL peaks, while after Mn^{2+} doping only one peak is observed. This makes it clear that introducing Mn^{2+} ion into the $SrAl_2O_4$ matrix influences the structure of traps in the matrix. Also, energy transfer from the host matrix $SrAl_2O_4$ itself to Mn^{2+} as shown in Figure 4.14 is possible.

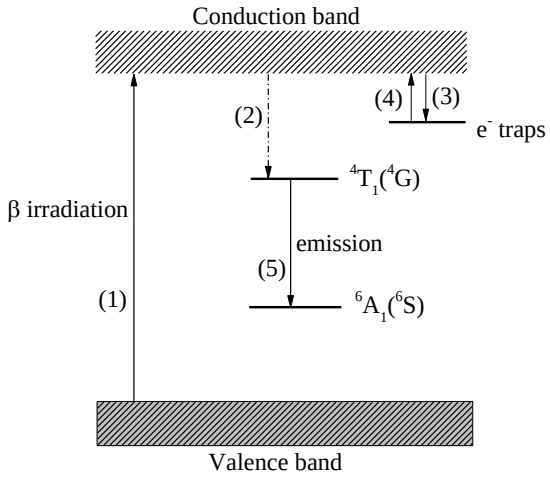

Figure 4.14: The possible mechanism of long lasting phosphorescence in the as-prepared $SrAl_2O_4:Mn^{2+}$ phosphor [45].

Beta irradiation promotes electrons from the valence band to the conduction band (transition 1). This creates free electrons and holes in the host lattice. A fraction of these electrons can decay non-radiatively into the excited states of Mn^{2+} (transition 2).Another fraction of these free electrons in the conduction gets trapped in the electron traps (transition 3). During sample heating, the trapped electrons are liberated into the conduction band (transition 4) where they can drop to the higher energy states of Mn^{2+} (transition 2) and recombine with holes in the lower energy states of Mn^{2+} (transition 5) to give out energy as thermoluminescence.

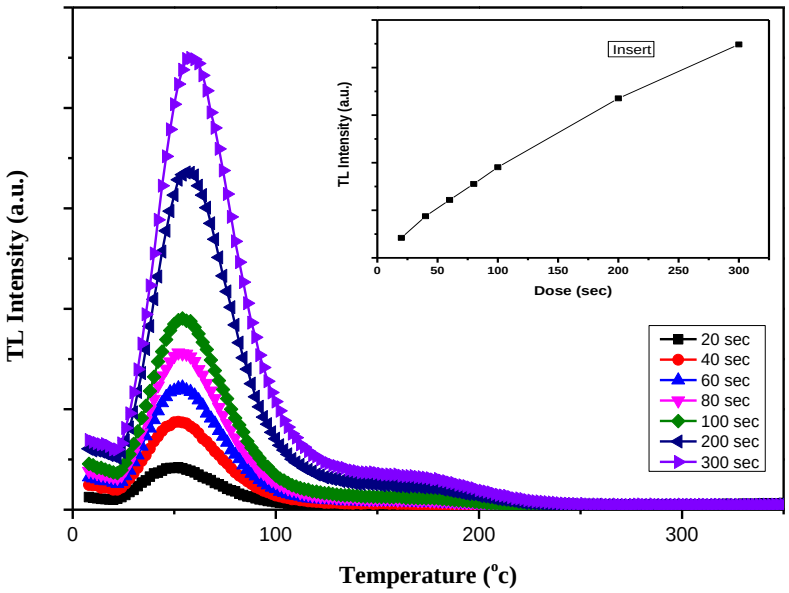

Figure 4.15: TL curves of the as-prepared $SrAl_2O_4:Dy^{3+}$ phosphor showing the effect of dose variation on the TL glow curve.

To study the influence of dose variation on TL glow curve, $SrAl_2O_4:Dy^{3+}$ phosphor was chosen and the glow curves are shown in Figure 4.15. The TL glow curves were recorded at a linear heating rate of 1 $^oC/s$ after exposure to various doses in the range 20 to 300 sec from a beta (β) source (0.1028 Gs/s). The TL intensity increases as the irradiation dose increases as can be seen on the insert of Figure 4.15. This linear response of $SrAl_2O_4:Dy^{3+}$ phosphor to irradiation dose is attributed to the fact that when the irradiation dose is increased, more traps responsible for the observed TL peaks in Figure 4.15 are filled [46]. No obvious changes in shape and peak position were observed. It is therefore deduced from the unchanging nature of the peak position that the TL process follows a first order kinetics [47].

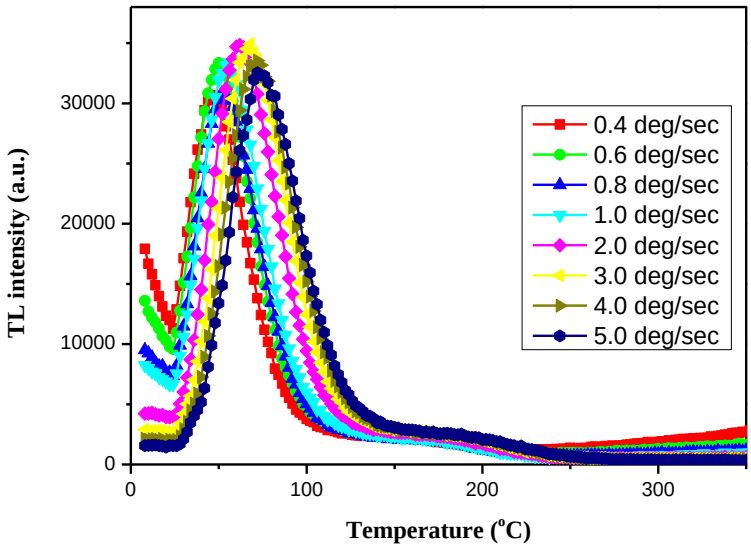

Figure 4.16: TL curves of $SrAl_2O_4:Dy^{3+}$ phosphor showing the effect of heating rate variation on the temperature at maximum intensity (T_m).

In order to understand how varying the heating rates influences the TL glow curves, TL measurements were carried out on the $SrAl_2O_4:Dy^{3+}$ Phosphor at different heating rates while keeping dose at 100 sec. Figure 4.16 presents the resulting TL glow curves. It was observed that TL intensity decreases with the increase in heating rate β, while T_m shifts to higher temperatures. All these observations are associated to thermal quenching [48]. This quenching can be explained by the Mott-Zeitz model [49], in which electrons captured into the excited state of a recombination center are believed to have two possible competing ways to recombine with holes in the ground state of this recombination center, one of which is a direct recombination with the emission of light.

The other route is an indirect thermally assisted transitioning of electrons from the excited state of the recombination center to the ground state by giving up energy to the lattice as phonons instead of emitting light. The probability of this non-radiative process $A_{NR}(s^{-1})$ has according to the Mott-Zeitz model a temperature dependent factor exp $(-W/k_BT)$, where T is the temperature, k_B is the Boltzmann's constant, and W is the activation energy [49]. From this factor it is clear that at higher temperatures the non-radiative probability will increase and consequently decrease the intensity of the TL output signal.

4.4. Conclusion

SEM studies witnessed the existence of irregular crystalline particles. The UV-vis studies show the decrease of the band gap with the incorporation of the rare earth dopants, and a decrease of the band gap after Mn^{2+} incorporation. The photoluminescence (PL) spectra show the typical transitions of Eu^{2+} ($4f^6 5d^1 \rightarrow 4f^7$), Eu^{3+} ($^5D_0 \rightarrow {}^7F_J$), Dy^{3+} ($^4F_{9/2} \rightarrow {}^6H_{15/2}$, $^4F_{9/2} \rightarrow {}^6H_{13/2}$, and $^4F_{9/2} \rightarrow {}^6H_{11/2}$), and Mn^{2+} ($^4T_1(^4G) \rightarrow {}^6A_1(^6S)$) respectively.

The PL spectra also exhibits the increase in Mn^{2+} emission intensity after co-doping the $Sr_{0.98}Al_2O_4:Mn^{2+}{}_{0.02}$ sample with Eu^{2+}, while co-doping with Dy^{3+} decreased the Mn^{2+} emission intensity. The long afterglow of the $Sr_{0.97}Al_2O_4:Eu^{2+}{}_{0.01},Dy^{3+}{}_{0.02}$ phosphor can be ascribed to a Dy^{3+} ion that plays a hole trapping and prolonging the luminescence time. The even longer lasting luminescence of the $Sr_{0.95}Al_2O_4:Eu^{2+}{}_{0.01}Mn^{2+}{}_{0.02},Dy^{3+}{}_{0.02}$ phosphor may be ascribed to the incorporation of Mn^{2+} ion in the phosphor.

References

1. C. R. Ronda, Luminescence: from theory to Applications, John Willey & Sons, 2008, 29-31
2. L. Ozawa, Cathodoluminescence and Photoluminescence: Theories and Practical Applications, CRC Press, 2010, 2-4
3. S. Shionoya, W. M. Yen, H. Yamamoto, Phosphor Handbook, CRC Press, 2012, pp810
4. M. Ayvacıkli, Z.Kotan, E.Ekdal, Y.Karabulut, A.Canimoglu, J.GarciaGuinea, A.Khatab, M.Henini, N.Can, J.Lum. **144** (2013) 128-132
5. C. H. Lu, S. Y. Chen, C. H. Hsu, Materials Science and Engineering B, Elsevier, (2012), 5915-5924
6. M. Ayvacikli, A. Ege, N. Can, *J.Lum.* **131** (2011) 2432-2439
7. X. Qiu a, Y. Xu, X. Qiao, *Mat. Lett.* **61** (2007) 2731-2734
8. B.M. Mothudi, O.M.Ntwaeaborwa, A.Kumar, K.Sohn, H.C.Swart, Physica B, 2012, 1679-1682
9. P. P. Pal, J. Manam, J.Lum. **145** (2014) 340–350
10. C. Manjunatha, D.V. Sunitha, H. Nagabhushana, B.M. Nagabhushana, S.C. Sharma, R.P.S. Chakradhar, Spectrochimica Acta Part A: Molecular and Biomolecular Spectroscopy, 2012, 140-148
11. P.Yang, M. K. Lu, C. F. Song, S. W. Liu, D. Xu, D. R. Yuan, X. F. Cheng, *J.Opt. Matt.* **24** (2003) 575–580
12. Pavana S. V. Mocherla, C. Karthik, R. Ubic, M. S. Ramachandra Rao, C. Sudakar, *J. Appl. Phys. Lett.* **103**, (2013), 022910
13. H. A. Rahnamaye Aliabad, H. Arabshahi, A. Hamel Aliabadi, *Int. J. Phys. Sci* **7(5)** (2012) 696-708
14. H. Song, D. Chen, W. Tang, Y. Peng, *J. Displays.* **29** (2008) 41-44
15. B.M Mothudi, Synthesis and characterization of strontium (Sr), Barium (Ba) and Calcium (Ca) Acuminate phosphors doped with rare earth ions, University of The Free State, 2009, pp 68
16. O.S. Wolfbeis, P. Hanninen, h. Harma, Lanthanide Luminescence: Photophysical, Analytical, And Biological Aspectcs,2011, pp 237
17. K. N. Shinde, S. J. Dhoble, H. C. Swart, K. Park, Phosphate Phosphors For Solid-State Lighting, 2012, pp121-179
18. Y. Tian, B. Chen, B. Tian, R. Hua, J. Sun, L. Cheng, H Zhong, X. Li, J. Zhang, Y. Zheng, T. Yu, L. Huang, Q. Meng, *J. Alloys Compd.* **509** (2011) 6096-6101
19. R. Rotman, Wide-Gap Luminescent Materials: Theory and Applications, Springer, 1997, pp32
20. Z. Jun, W. Yu-Hua, L. Bi-Tao, L. Ji-Di, Chin. Phys. B, 2010, 127809
21. K. N. Shinde, S. J. Dhoble, H. C. Swart, K. Park, Phosphate Phosphors For Solid-State Lighting, 2012, pp121-179

22. Z. He, X. Wang, W. M. Yen, *J. Lumin.* **129** (2007), 381-384
23. Botao Wu 1, 2, Shifeng Zhou 3, Jian Ruan 1, 2, Yanbo Qiao, Danping Chen, Congshan Zhu, Jianrong Qiu, Optics Express, 2008, 1879-1884
24. FengliYang, WeiAn, WeidongZhuang, Guang-ShanTian, Xi-PingJing, *J.lumen.***146** (2014) 269-274
25. Q. Xiao,L. Xiao,Y. Liu , X. Chen,Y. Li, *J.phys. Chem.Solids.* **71** (2010) 1026-1030
26. L. Lin, C. Shi, Z. Wang, W. Zhang, M. Yin, *J.Alloy.Compd*. **466** (2008) 546–550
27. P. Dorenbos, J.Electron. Chem. Society. **152** (2005) 107-110
28. S. Ye, J. Zhang, X. Zhang, X. Wang, *J. Lumin.***122-123** (2007) 914–916
29. X. Wang, D. Jia, W.M. Yen, *J. Lumin.* **102** (2003) 34–37
30. Y. Gong, Y. Wang, X. Xu, Y. Li, S. Xin, L. Shi, *J.Opt.Matt.* **33** (2001) 1781-1785
31. M. Sauer, J. Hofkens, J. Enderlein, Handbook of Fluorescence Spectroscopy and Imaging: From Ensemble to Single Molecules, John Wiley & Sons, 2010, pp 6-4
32. P. Zhang, M. Xu, Z. Zheng, B. Sun, Y. Zhang, *J. Mater. Scie. Eng.* **136** (2007), 159-164
33. N. Xie, J. Liu, Y. Huang, S. Kim, H. J. Seo, *J. Ceram. Internat*. **38** (2012) 1489-1495
34. R. Chen, V. Pagonis, J.L. Lawless, J.Radiat. Meas. **43** (2008) 162-166
35. M. E. Haghiri, E. Saion, W.S. Wan Abdullah, N. Soltani, M. Hashim, M. Navasery, M. A. Shafaei, J. Radiat. Phys. Chem. **90** (2013) 1-5
36. M. V. dos S Rezende,R. M. Araujo, M. E. G. Valerio, R. A. Jackson, J. phys. **249** (2010) 012042
37. C. Furetta, Handbook of Thermoluminescence, World Scientific, USA, 2009, pp133
38. C. Pereyda-Pierre, R. Meléndrez, R. García, M. Pedroza-Montero, M. Barboza-Flores, j.Radiat. Meas. **46** (2011) 1417-1420
39. B. Kore, N.S.Dhoble, S.J.Dhoble, Recent Research in Science and Technology, 2012, 85-86
40. P. Pathak, A. Selot, R. Kurchania, *J.Radiat.Phys.Chem.* **99** (2014) 26-29
41. L.Y. Liu, Y.L. Zhang, J.Q. Hao, C.Y. Li, Q. Tang, C.X. Zhang, Q.Su, *Mat Lett.* **60** (2006) 639-642
42. Y. Huang, Q. Ma, J. Lumin. **160** (2015) 271-275
43. M. Wan, Y. Wang, X. Wang, *J. Lumin.***145** (2014) 914-918
44. M. E. Haghiri, E. Saion, W.S. Wan Abdullah, N. Soltani, M. Hashim, M. Navasery, M. A. Shafaei, J. Radiat. Phys. Chem. **90** (2013) 1-5
45. G. Che, C. Liu, X. Li, Z. Xu, Y. Liu, H. Wang, *J. Phys. Chem. Solids.* **69** (2008) 2091-2095
46. B. Ildusovich Kharisov, O. V. Kharissova, U. O. Mendez, Radiation Synthesis of Materials and Compounds, CRC Press, 2013, pp 159
47. C. M. Sunta, Unraveling Thermoluminescence, Springer, 2014, pp 100

48. J.M. Kalita, G. Wary, *J. Lumin.***146** (2014) 508-511

49. V. Pagonis, C. Ankjærgaard, A.S. Murray, M. Jain, R. Chen, J. Lawless, S. Greilich, *J. Lumin.***130** (2010) 902-909

CHAPTER 5

Luminescence properties of Eu^{2+}, Dy^{3+} and Mn^{2+} ions doped $BaAl_2O_4$ synthesized by combustion method.

5.1. Introduction

Alkaline metal aluminates activated by rare earth ions have drawn a lot of interest of many researchers recently, mainly because of their interesting potential applications and their chemical stability [1]. Among their interesting applications, these materials are also known to have found applications in modern lighting, displays, and optical communications [1]. Owing to the comparable ionic radii of alkaline metals and rare earth ions, the aluminates are found to be good hosts for rare earth ions [1]. $BaAl_2O_4$ is a material that falls under stuffed tridymites class [2], and it has good properties such as high melting point and hydraulic hardening, which resulted in a considerable interest of this material in refractory cement applications [3]. $BaAl_2O_4$ material shows interesting luminescence properties under UV radiation when doped with rare-earth ions. In this work, $BaAl_2O_4$ singly doped with 1 mol% of Eu^{2+}, 2 mol% of Mn^{2+}, and 2 mol% of Dy^{3+} phosphors were synthesized by combustion method at the initiating temperature of 600 ^oC, and photoluminescence and phosphorescence properties were studied.

5.2. Experimental procedure

5.2.1. Synthesis

The nano-crystalline $BaAl_2O_4:Eu^{2+}$, $BaAl_2O_4:Mn^{2+}$ and $BaAl_2O_4:Dy^{3+}$ phosphors were synthesized using combustion method. The appropriate nitrites ($Ba(NO_3)_2$, $Al(NO_3)_3.9H_2O$, $Eu(NO_3)_3$, for $BaAl_2O_4:Eu^{2+}$ preparation, ($Ba(NO_3)_2$, $Al(NO_3)_3.9H_2O$, and $Dy(NO_3)_3$ for $BaAl_2O_4:Dy^{3+}$ preparation, and ($Ba(NO_3)_2$, $Al(NO_3)_3.9H_2O$, and $Mn_2N_6.4H_2O$) for $BaAl_2O_4:Mn^{2+}$ all in analytical purity of 99.9% were used separately as starting materials and

urea (CH_4N_2O) was added into all the three separate mixtures as a reducer and as a flux. The mixtures were separately ground in crucibles until homogeneous mixtures were obtained. The crucibles containing the mixtures were separately put into a furnace to calcine in air at 600 ^oC for 5 minutes. White ashes of $BaAl_2O_4:Eu^{2+}$ and $BaAl_2O_4:Dy^{3+}$phosphors together with a slightly greenish ash of $BaAl_2O_4:Mn^{2+}$ were obtained. All the ashes were then further ground in agate mortar to obtain homogeneous final powder phosphors.

5.2.2. Characterization

The phase and crystallinity of the samples were investigated using an X'Pert PRO PANalytical diffractometer with CuKα at λ = 0.15405 nm. The particle morphologies of the powders were investigated using a JEOL JSM-7500F field-emission scanning electron microscope (FE-SEM). The photoluminescence (PL) spectra were recorded at room temperature using a Jobin Yvon/SPEX FluoroLog spectrofluorometer (Model FL-1057) equipped with a 450 W Xenon light source, double excitation and emission monochromators, and R928 PMT detector.

5.3. Results and Discussions

5.3.1. Surface Morphology

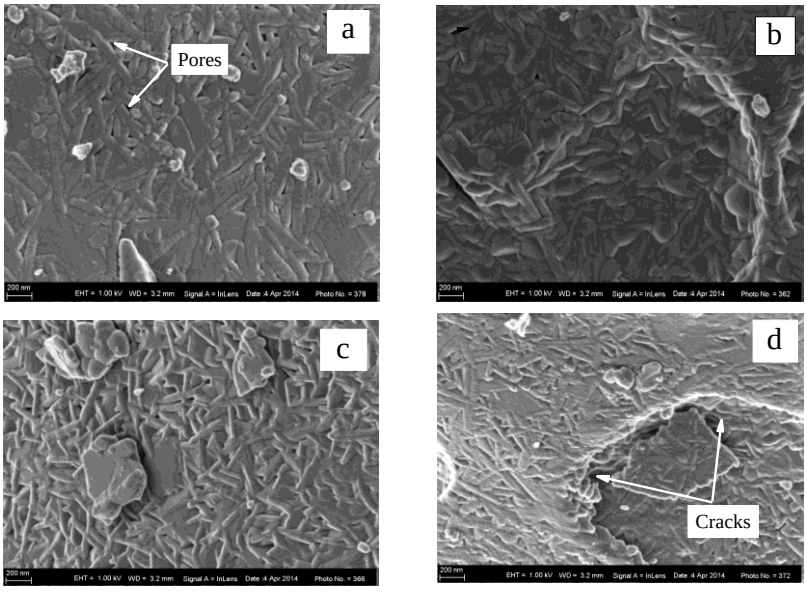

Figure 5.1: SEM micrograph of the as-synthesised (a): $BaAl_2O_4$, (b): $BaAl_2O_4:Eu^{2+}$, (c): $BaAl_2O_4:Dy^{3+}$, (d): $BaAl_2O_4:Mn^{2+}$phosphors.

SEM images of the as-synthesized $BaAl_2O_4$, $BaAl_2O_4:Eu^{2+}$, $BaAl_2O_4:Dy^{3+}$, and $BaAl_2O_4:Mn^{2+}$ phosphors taken at a magnification of X 50 000 are shown in Figure 5.1. The SEM micrographs show irregular shaped particle structures consisting of rod-like particles with some agglomeration. The cracks and pores on the surfaces of the samples are attributed to the gasses escapping during combustion method [4].

5.3.2. Structural properties

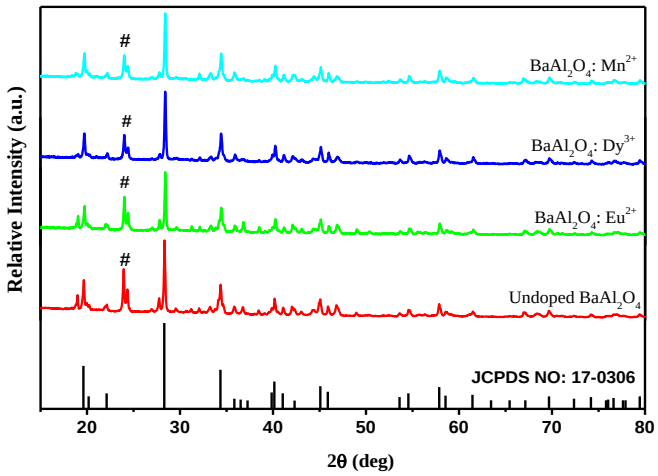

Figure 5.2: Powder X-ray Diffraction patterns (XRD) of (a): un-doped $BaAl_2O_4$, (b) $BaAl_2O_4:Eu^{2+}$, (c): $BaAl_2O_4:Dy^{3+}$, and $BaAl_2O_4:Mn^{2+}$ phosphors prepared by combustion method.

Figure 5.2 shows the powder XRD diffraction patterns of $BaAl_2O_4$ phosphor doped with different dopants. The patterns confirm the hexagonal phase of $BaAl_2O_4$ according to the JCDPS data file no (17-0306), together with the existence of small amount of traces of $BaAl_{12}O_{19}$ impurity phase (marked with a hash) in the material [5]. The impurity phase may be a result of a high temperature that may be attained locally during the combustion synthesis [5]. As can be seen from the figure, there was no observable shift in 2θ positions and the widths of the XRD peaks after the incorporation of different dopants in the $BaAl_2O_4$ matrix. This is most likely to be due to low concentrations of dopant ions.

5.3.3. Photoluminescence properties

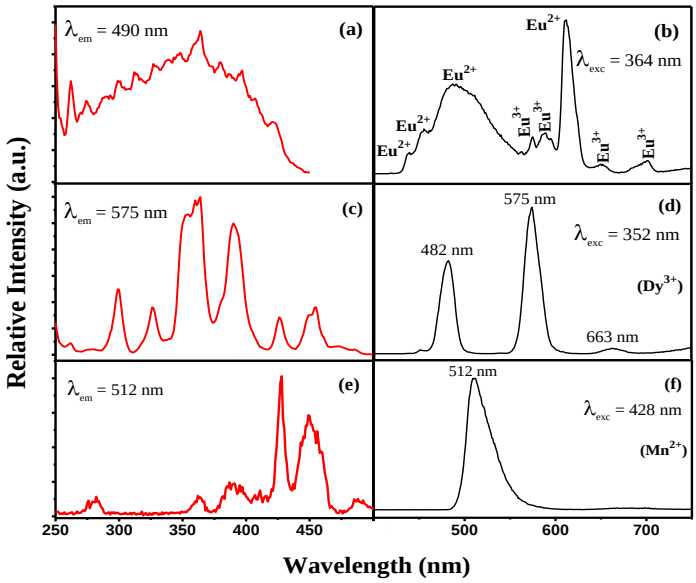

Figure 5.3: The excitation spectra (a), (c), (e) and emission spectra (b), (d), and (f) of Eu^{2+}, Dy^{3+}, and Mn^{2+} doped $BaAl_2O_4$ phosphor respectively.

Figure 5.3 shows the room temperature excitation and emission spectra of $BaAl_2O_4$ phosphor doped with Eu^{2+}, Dy^{3+} and Mn^{2+}. Figure 5.3(a) and (b) respectively represent the excitation and emission spectra of $BaAl_2O_4$:Eu^{2+} phosphor. The excitation spectrum was monitored by a broad band centered at 490 nm which can be attributed to the $4f^6 5d^1 \rightarrow 4f^7$ transition of the Eu^{2+} ion [6]. The emission spectrum in Figure 5.3(b) was collected after excitation of the sample by the highest excitation peak (364 nm) on the excitation spectrum, and the emission spectrum showed the presence of both Eu^{2+} and Eu^{3+} ions in the sample as shown in the figure. The emission peaks of the Eu^{3+} ions attributed to the 4f to 4f transitions were also observed. It is interesting to observe in Figure 5.3 (b) a peak at 611 nm, which is more intense than all other peaks. Peng et al [7] also reported a similar peak and attributed it to the $^5D_0 \rightarrow {}^7F_2$ hypersensitive transition of the Eu^{3+} ion. They also reported that the emission from the $^5D_0 \rightarrow {}^7F_2$ transition becomes more intense in low symmetry sites in a matrix than in high symmetry sites, and therefore the prominent nature of the 611 nm in this case suggests that the Eu^{3+} ions reside in low symmetry sites of barium in the $BaAl_2O_4$ matrix.

Figure 5.3(c) and (d) represent the room temperature excitation and emission spectra of the $BaAl_2O_4$:Dy^{3+} phosphor prepared at an initiating temperature of 600 ^oC. The excitation spectrum was monitored at 575 nm and the sample was excited at 352 nm as shown in the Figure. The emission peaks observed at 482 nm, 575 nm, and 663 nm can be ascribed to the $^4F_{9/2} \rightarrow {}^6H_{15/2}$, $^4F_{9/2} \rightarrow {}^6H_{13/2}$, and $^4F_{9/2} \rightarrow {}^6H_{11/2}$ transitions of the Dy^{3+} ion respectively [8].

Figure 5.3(e) and (f) show the room temperature excitation and emission spectra of $BaAl_2O_4$:Mn^{2+} phosphor respectively. The excitation spectrum was recorded while monitoring the emission at 512 nm and the sample was excited at 428 nm, the highest excitation peak on the excitation spectrum as shown in the figure. The excitation spectrum consists of a weak broadband emission peak centered at 282 nm which can be ascribed to the host lattice absorption, and four other peaks at 361 nm, 383 nm, 425 nm, and 450 nm which can be ascribed to the $^6A_1$-$^4T_1$ (^4P), $^6A_1$-$^4T_2$ (^4D), $^6A_1$-$^4A_1$ (^4G), and $^6A_1$-$^4T_2$ (^4G) transitions respectively [9].

The emission spectrum in Figure 5.3 (f) consists of a single broadband centered at 512 nm. A similar broadband was reported in barium aluminate host in literature [9], and ascribed to a characteristic emission band of the Mn^{2+} ion from the ${}^4T_1({}^4G) \rightarrow {}^6A_1({}^6S)$ transition. When the Mn^{2+} ion is surrounded by a weak crystal field (tetrahedrally coordinated), the d excited state of the Mn^{2+} is weakly split and result in Mn^{2+} emitting on the short part of the spectrum. In contrast, when the field is strong (octahedrally coordinated), the d excited state of the Mn^{2+} ion is more split and Mn^{2+} emits on the long part of the spectrum [9]. The Mn^{2+} ion in $BaAl_2O_4$:Mn^{2+} only showed a green emission which suggests that the Mn^{2+} ion is tetrahedrally coordinated and experiences a weak crystal field in the $BaAl_2O_4$:Mn^{2+} phosphor.

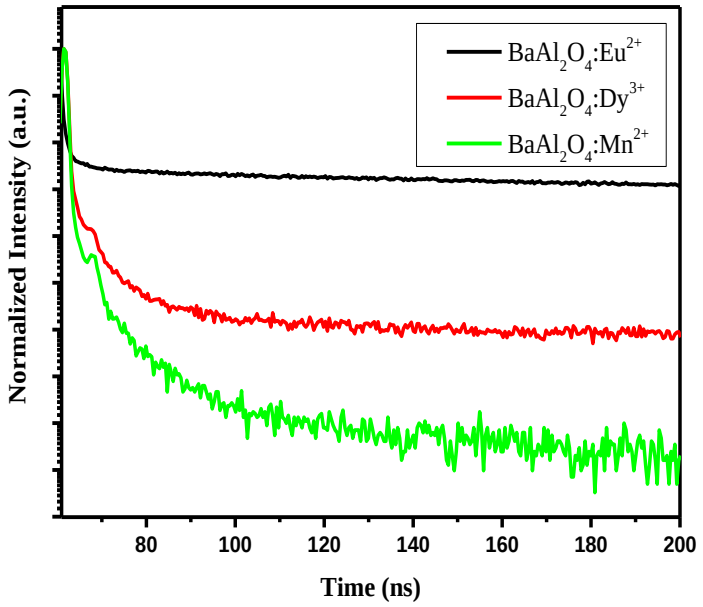

Figure 5.4: Decay curves of the as-prepared $BaAl_2O_4$ phosphors doped with different activator ions.

Figure 5.4 presents the decay curves representing luminescence lifetimes from the transition $4f^6 5d^1 \rightarrow 4f^7$ (490 nm emission peak), the ${}^4F_{9/2} \rightarrow {}^6H_{13/2}$ transition (575 nm emission peak), and the transition ${}^4T_1({}^4G) \rightarrow {}^6A_1({}^6S)$ (512 nm emission peak) of $BaAl_2O_4$: Eu^{2+}, $BaAl_2O_4$: Dy^{3+} and $BaAl_2O_4$: Mn^{2+} phosphors respectively. Both the Eu^{2+} and the Mn^{2+} doped phosphors were irradiated for 5 minutes from a 375 nm Nano-LED, and the Dy^{3+} doped phosphor was irradiated for 5 minutes from a 389 nm Nano-LED. As can be observed from the Figure, the luminescence decay of the Eu^{2+} ion doped sample is slower than the other two samples. The decay curve from

all the samples were best fitted using the five exponentials function in equation 5.1, and the decay parameters after fitting the data are listed in table 5.1.

$$I(t) = A_1 e^{\frac{-t}{\tau_1}} + A_2 e^{\frac{-t}{\tau_2}} + A_3 e^{\frac{-t}{\tau_3}} + A_4 e^{\frac{-t}{\tau_4}} + A_5 e^{\frac{-t}{\tau_5}} \quad (5.1)$$

Where *I (t)* represents the luminescence intensity at time *t* after irradiating the sample, A_1, A_2, A_3, A_4, and A_5 are constants; τ_1, τ_2, τ_3, τ_4, and τ_5 are decay times for the exponential components describing the decay rates for the fast (τ_1 and τ_2), average (τ_3 and τ_4) and slow (τ_5) exponential components. The decay times were found to be of higher values for the $BaAl_2O_4$: Eu^{2+} phosphor, followed by $BaAl_2O_4$: Dy^{3+} and lastly $BaAl_2O_4$: Mn^{2+} phosphor with the lowest values. This could be associated with the differences in trap depths created by Eu^{2+}, Dy^{3+}, and Mn^{2+} in the lattice of the $BaAl_2O_4$ host. The rate of recombination of charge carriers, and hence the decay parameters are significantly affected by the trap depths, i.e. deep traps are associated with long lifetimes and shallow traps are associated with short lifetimes [10]. In this case, it is possible that the traps created by Eu^{2+} doping in the $BaAl_2O_4$ host are deeper, followed by the ones created by Dy^{3+}, and lastly the ones created by Mn^{2+} doping.

Table 5.1: Decay parameters of the as-synthesized $Ba_{0.99}Al_2O_4:Eu^{2+}{}_{0.01}$, $Ba_{0.98}Al_2O_4:Dy^{3+}{}_{0.02}$ and $Ba_{0.98}Al_2O_4$: $Mn^{2+}{}_{0.02}$ phosphors prepared by combustion method.

Decay Times(ns)	***$BaAl_2O_4$: Eu^{2+}***	***$BaAl_2O_4$: Dy^{3+}***	***$BaAl_2O_4$: Mn^{2+}***
τ_1	5.90	0.8	0.30
τ_2	29.40	4.30	1.50
τ_3	118.00	17.10	6.00
τ_4	294.00	42.70	14.90
τ_5	589.00	85.3	29.80

5.4. Conclusion

$BaAl_2O_4:Eu^{2+}$, $BaAl_2O_4$: Dy^{3+} and $BaAl_2O_4:Mn^{2+}$ phosphors were successfully prepared by combustion method at an initiating temperature of 600 ^oC. The main diffraction peaks of the $BaAl_2O_4$ hexagonal phases were observed in all samples. A broad band at 490 nm in the $BaAl_2O_4:Eu^{2+}$ phosphor is ascribed to the compression of the $BaAl_2O_4$ host lattice when the Eu^{2+} ion substitutes the Ba^{2+} ion in the lattice due to the mismatching of the ionic radii between the two ions. All the emission bands in the $BaAl_2O_4$: Dy^{3+} phosphor are from the 4f-4f intra-band transition. The $BaAl_2O_4:Mn^{2+}$ phosphor showed a single emission band at 512 nm, suggesting that an emission from this phosphor is from only one emission center, and the green emission color suggests that the emission is from a Mn^{2+} ion which occupies a site that is considerably larger than its ionic radius in the $BaAl_2O_4$ matrix.

References

1. R.J. Wiglusz, T. Grzyb, *J. Opt. Mater*. **36** (2013) 539-545
2. N. Suriyamurthya, B.S. Panigrahi, *J. Lumin.* **127** (2007) 483-488
3. I. Odler, Special Inorganic Cements, E & FN Spon, USA, 2000, pp 177
4. M. Ayvacıklı, A. Ege, N. Can, *J. Lumin.* **131** (2011) 2432-2439
5. Rodrigues, et al., Physica B (2013), http://dx.doi.org/10.1016/j.physb.2013.11.007
6. W. Chung, H. J. Yu, S. H. Park, B. Chun, J. Kim, S. H. Kim, *J. Cryst. growth.* **326** (2011) 73-76
7. M. Peng, G.Hong, *J. lumen.* **127** (2007) 735-740
8. K. N. Shinde, S. J. Dhoble, H. C. Swart, K. Park, Phosphate Phosphors For Solid-State Lighting, Springer, Berlin Heidelberg, 2012, pp121-179
9. Y. Shi, Y. Wen, M. Que, G. Zhu, Y. Wang, Royal Society of Chemistry, Dalton Trans, 2014, 2418-2423
10. J. J. Lowe, M. J. C. Walker, Reconstructing Quaternary Environments, Routledge, 2014, pp 292

CHAPTER 6

The role of Dy^{3+} concentration on the luminescence and structural properties of $BaAl_2O_4$ phosphors prepared by combustion method.

6.1. Introduction

Trivalent dysprosium activated luminescent materials are generally recognized by having two intense characteristic emission bands around 482 nm (blue) and 575 nm (yellow), as well as a weak red emission at 663 nm. These materials have been studied to a large extend due to their possible applications in the white light emissions, i.e. white light emitting diodes. This possibility is a result of the two dominant bands at 482 nm and 575 nm in the materials containing Dy^{3+} ions [1]. Some advantages of these materials include; longer lifetime, they consume less energy and they are non-toxic (environmentally friendly) [2].

The 482 nm, the 575 nm, and the 663 nm bands result from the $^4F_{9/2} \rightarrow {}^6H_{15/2}$, $^4F_{9/2} \rightarrow {}^6H_{13/2}$, and $^4F_{9/2} \rightarrow {}^6H_{11/2}$ transitions of Dy^{3+} respectively [2]. The two dominant transitions, $^4F_{9/2} \rightarrow {}^6H_{15/2}$, and $^4F_{9/2} \rightarrow {}^6H_{13/2}$ provide the possibility of achieving a near white light by adjusting the yellow to blue (Y/B) emission intensity ratio [2], and this can be achieved by adjusting the yellow emission intensity resulting from the hypersensitive transition $^4F_{9/2} \rightarrow {}^6H_{13/2}$ of Dy^{3+} ion through concentration variation of the Dy^{3+} ions in the host lattice [3]. In addition, various hosts can be studied to adjust the Y/B ratio [3]. Dy^{3+} activated $BaAl_2O_4$ phosphors with different Dy^{3+} concentrations were successfully synthesized by combustion method. The influence of the doping concentration of Dy^{3+} on the host band gap was investigated. The influence of Dy^{3+} concentration on the emission intensity was also investigated.

6.2. Experimental Procedure

6.2.1. Synthesis

Dy^{3+} doped barium aluminate was synthesized using combustion method. The appropriate nitrites $Ba(NO_3)_2$, $Al(NO_3)_3.9H_2O$, and $Dy(NO_3)_3$ all in analytical purity of 99.9% were used as starting materials and urea (CH_4N_2O) was added into the mixtures as a reducer and a flux. The mixture was ground in a crucible until homogeneous mixture was obtained. A crucible containing the mixture was put into a furnace to calcine the mixture in air at 600 ^oC for 5 minutes. A white ash of $BaAl_2O_4$ phosphor was obtained. The white ash was then further ground in agate mortar to obtain a homogeneous final powder phosphor.

6.2.2. Characterization

A white-light-emitting trivalent dysprosium (Dy^{3+}) activated barium aluminate phosphor with different concentrations was synthesized by combustion method in a muffle furnace at an initiating temperature of 600 ^oC. The X-ray diffraction (XRD) patterns of the samples were performed using an X'Pert PRO PANalytical diffractometer with CuKα at λ = 0.15405 nm. The particle morphologies of the powders were investigated using a JEOL JSM-7500F field-emission scanning electron microscope (FE-SEM). The UV-Vis absorption spectra were recorded using Perkin-Elmer Lambda 750s UV-Vis spectrometer. The photoluminescence (PL) spectra were recorded at room temperature using a Jobin Yvon/SPEX Fluorolog spectrofluorometer (Model FL-1057) equipped with a 450 W Xenon light source, double excitation and emission monochromators, and R928 PMT detector. TL spectra were recorded using a Riso TL/OSL reader (Model DA-20).

6.3. Results

6.3.1. Structural properties

Figure 6.1 presents the powder XRD diffraction patterns of $BaAl_2O_4$ phosphor doped with different concentrations of the Dy^{3+} ions. The patterns confirm the hexagonal phase of $BaAl_2O_4$ according to the JCDPS data file no (17-0306), together with some traces of $BaAl_{12}O_{19}$ impurity phase (marked with a hash) in the material. The impurity phase may be a result of a high

temperature that may be attained locally during the combustion synthesis [5]. As can be seen from the figure, there was no observable shift in 2θ positions and the widths of the XRD peaks as the doping concentration was varied.

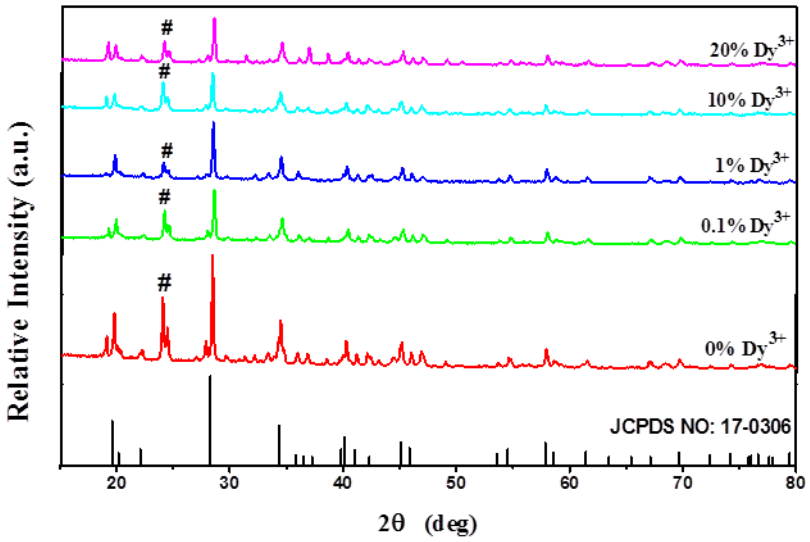

Figure 6.1: **Powder X-ray Diffraction patterns (XRD) of the un-doped $BaAl_2O_4$ phosphor (a), and the $BaAl_2O_4$ phosphor doped with (b): 0.1%, (c): 1%, (d): 10%, and (e): 20% of Dy^{3+} ion respectively.**

6.3.2. Surface morphology

Figure 6.2 shows the SEM images of the un-doped $BaAl_2O_4$ phosphor together with the $BaAl_2O_4$ phosphor doped with various concentrations of Dy^{3+}. All the samples clearly show the rod-shaped particles as the Dy^{3+} doping concentration increases. The pores on the surfaces of the samples are due to the escaping gases during combustion process.

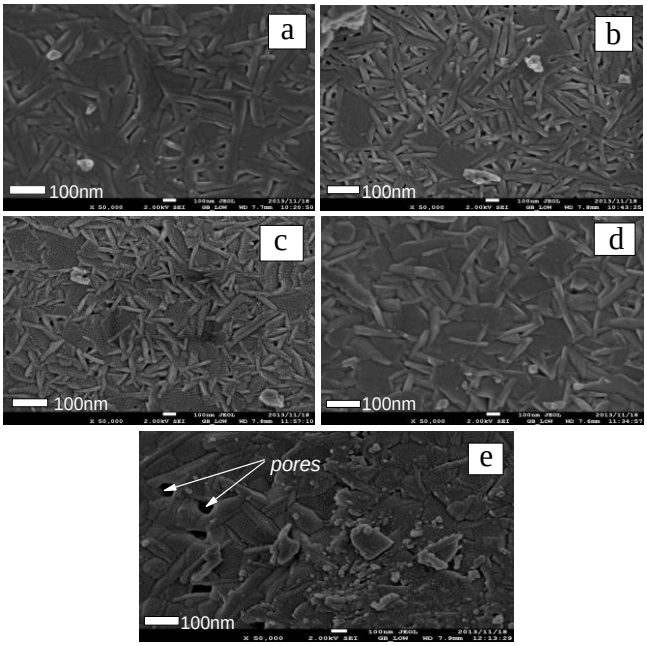

Figure 6.2: SEM images of (a): un-doped $BaAl_2O_4$ phosphor and $BaAl_2O_4$ phosphor doped with (b): 0.1%, (c): 1%, (d):10%, and (e): 20% of Dy^{3+} respectively.

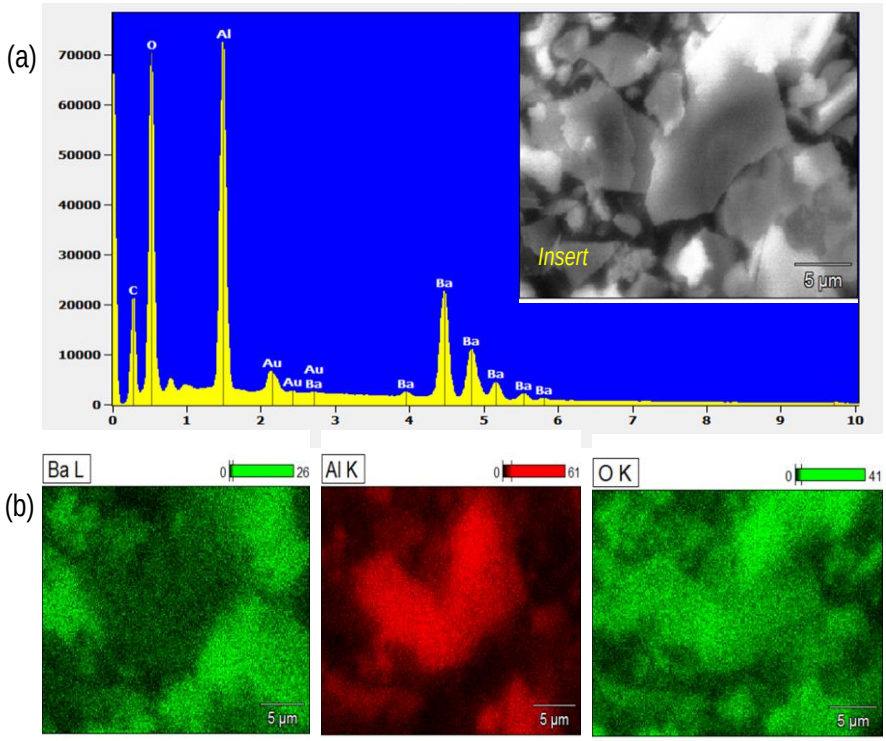

Figure 6.3(a): Energy Dispersive Spectroscopy spectrum (EDS), (b): Scanning Electron Microscopy (SEM) and Energy Dispersive Spectroscopy elemental mapping of the Un-doped $BaAl_2O_4$ phosphor prepared by combustion method.

Figure 6.3 shows the EDS spectrum and the elemental distribution in the $BaAl_2O_4$ phosphor. The insert in (a) shows the SEM image of the area used to conduct elemental mapping of the phosphor. The spectrum reveals the peaks associated with Ba, Al, and O which form the elemental composition of $BaAl_2O_4$. The additional peak associated with Au is due to coating of the sample and that of C appears due to carbon tape used as a substrate. The mapping in (b) also confirms the presence of Ba, Al, and O in the $BaAl_2O_4$ phosphor.

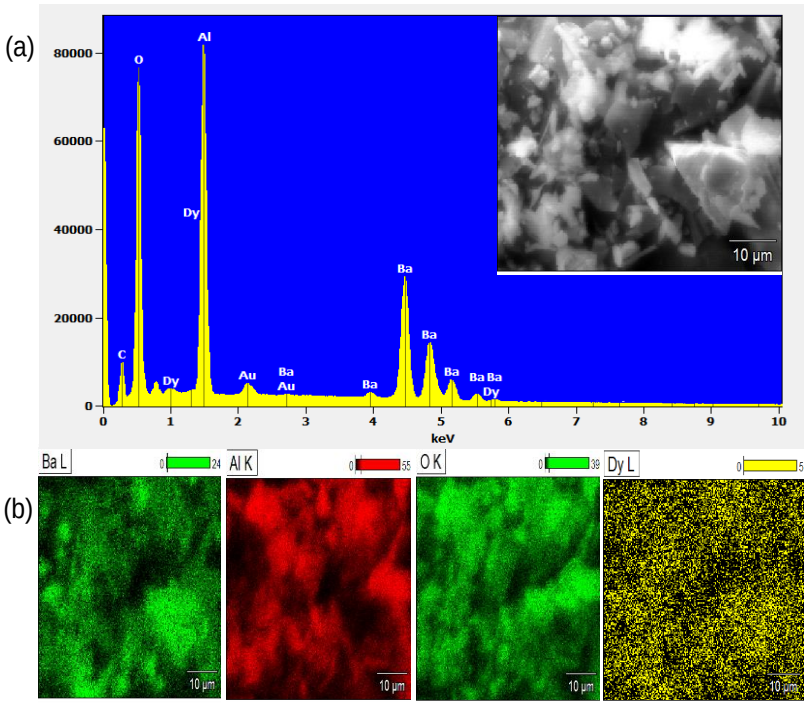

Figure 6.4(a): Energy Dispersive Spectroscopy spectrum (EDS), (b): Scanning Electron Microscopy (SEM) and Energy Dispersive Spectroscopy mapping of $BaAl_2O_4$ phosphor doped with Dy^{3+} ion prepared by combustion method.

Figure 6.4 presents the EDS spectrum and the elemental distribution in the $BaAl_2O_4$:Dy^{3+} phosphor. The insert in (a) shows the SEM image of the area used to conduct elemental mapping of the phosphor. All peaks associated with elements (Ba, Al, O and Dy) in the $BaAl_2O_4$:Dy^{3+} phosphor can be seen in the spectrum. Low intensity peaks of the dopant Dy^{3+} on the EDS spectrum is due to a very low concentration of Dy^{3+} in the $BaAl_2O_4$ phosphor. The additional peak associated with Au is due to coating of the sample and that of C appears due to carbon tape used as a substrate. The mapping in (b) also confirms the presence of Ba, Al, O and Dy in the $BaAl_2O_4$: Dy^{3+} phosphor.

6.3.3 Photoluminescence Properties

Figure 6.5 shows the Photoluminescence (PL) spectra of $BaAl_2O_4$ doped with various concentrations of Dy^{3+} ions. In the figure, the PL spectra consist of three typical emission peaks at 482 nm, 575 nm, and 663 nm which can be ascribed to the $^4F_{9/2} \rightarrow {}^6H_{15/2}$, $^4F_{9/2} \rightarrow {}^6H_{13/2}$, and

$^4F_{9/2} \rightarrow {}^6H_{11/2}$ transitions of Dy^{3+} ion respectively [54]. The results clearly illustrates that the concentration variation does not affect the shapes and the position of the characteristic emission peaks of the Dy^{3+} ions in the samples. The insert of Figure 6.5 shows the dependence of PL intensity on the Dy^{3+} concentration. It can be observed that the PL intensity first reaches a maximum at 0.3 mol% of Dy^{3+} doping concentration, then increase. It reaches a maximum again at 14 mol% and decrease, and finally reaches a maximum at 18 mol%. Beyond 18 mol% the luminescence seemed to have quenched [6].

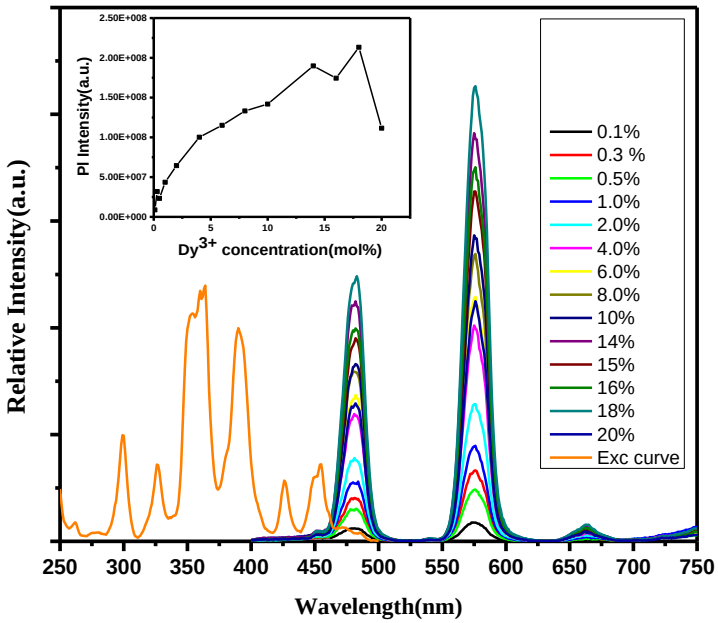

Figure 6.5: Excitation spectrum on the left and Emission spectra on the right of $BaAl_2O_4$ phosphor doped with different Dy^{3+} concentration.

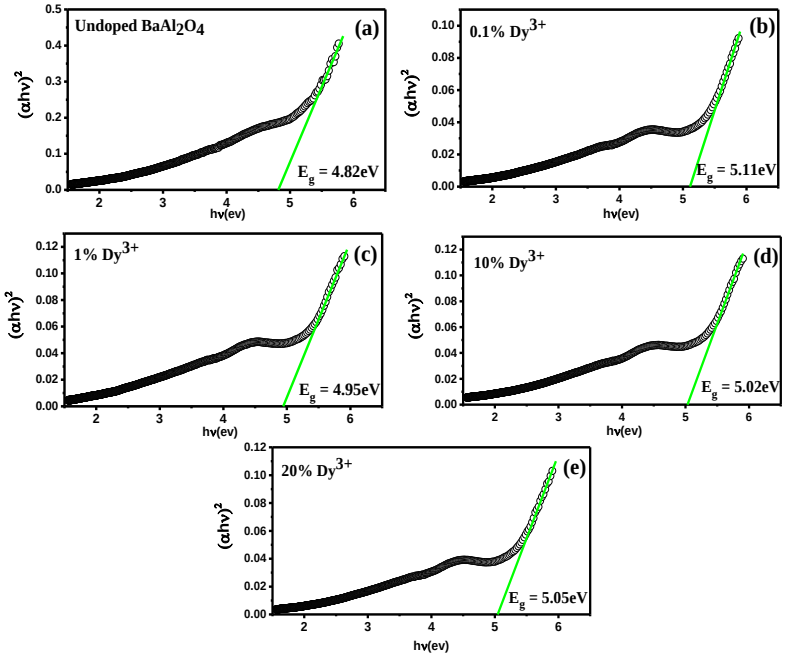

Figure 6.6: Tauc plots for band gap estimations from the absorption spectra of the undoped $BaAl_2O_4$ phosphor (a), and $BaAl_2O_4$ phosphor doped with 0.1% (b), 1% (c), 10% (d), and 20% (e) concentration of Dy^{3+}.

Figure 6.6 shows the band gap estimations of the $BaAl_2O_4$:Dy^{3+} phosphor at varying concentrations of Dy^{3+}. Figure 6.6 also shows the influence of the Dy^{3+} concentration ion as a dopant on the $BaAl_2O_4$ band gap. The band gaps of all powder samples were calculated using the Tauc relation [7], and their values change as shown in Figure 6.6.

$$(\alpha h\nu)^2 = K^2(h\nu - E_g) \qquad (6.1)$$

Where α is the absorption coefficient, $h\nu$ is the photon energy, K is a constant which depends on the type of transition, E_g is the band gap. The band gap of the $BaAl_2O_4$:Dy^{3+} phosphor first increased at low doping concentrations, and then decreased at high doping concentrations. The increase in band gap with the increase in Dy^{3+} concentration may be associated with Burstein-Moss shift [8], which occurs due to the population of states close to the conduction band as Dy^{3+} concentration increases. The Fermi level in a material of such level of doping is pushed into the conduction band and only allowing excitation of electrons into the conduction band, and therefore increasing the band gap of the material. It is also possible that at higher doping

concentrations shallow energy levels are created in the band gap, forming an impurity band just below the conduction band edge [9, 10]. Fusion of the conduction band and the impurity band brings about a phenomenon that tends to shrink the band gap of a semiconductor and this could be a reason for the decrease in band gap of the $BaAl_2O_4:Dy^{3+}$ phosphor as shown in Figure 6.6 at higher doping concentrations [9, 10].

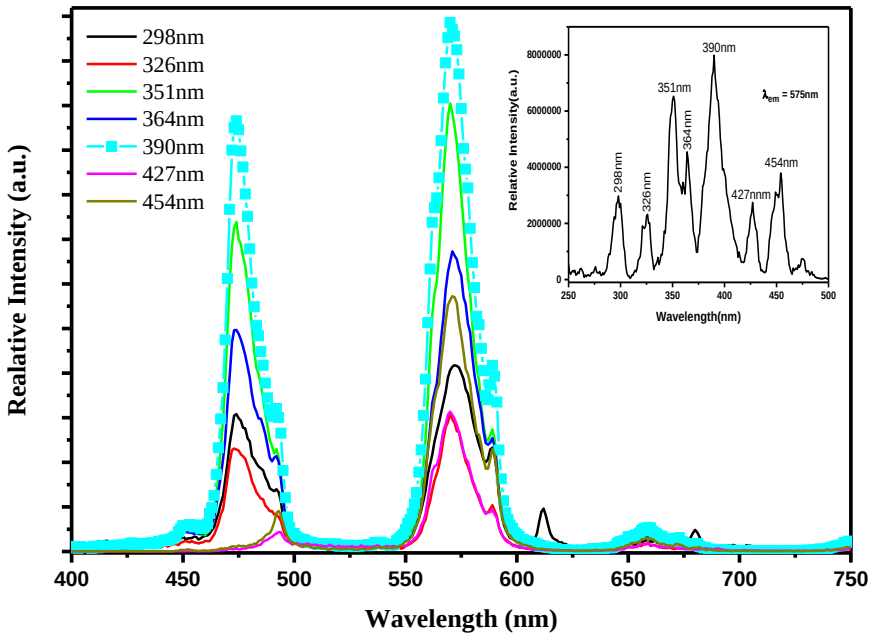

Figure 6.7: Emission spectra under Xenon lamp excitation showing the effect of excitation wavelength on $BaAl_2O_4$ phosphor doped with 2% Dy^{3+}.

Figure 6.7 shows PL emission spectra excited with different excitation wavelengths from 298 nm to 454 nm, and the insert shows the excitation spectrum monitored at 575 nm as shown in the figure. The figure consists of two (blue and yellow) dominant characteristic peaks of the Dy^{3+} ion. It is well known that the blue emission peak at 482 nm belongs to a magnetic dipole $^4F_{9/2} \rightarrow {}^6H_{15/2}$ transition and the yellow one at 575 nm belongs to a forced electric dipole $^4F_{9/2} \rightarrow {}^6H_{13/2}$ transition of the Dy^{3+} ion which is only favorable at low symmetry lattices [5]. It is clear from the figure that the yellow emission peak is more predominant than the blue one under all the excitation wavelengths, and this suggests that the Dy^{3+} ions are located at low symmetry sites within the $BaAl_2O_4$ matrix [11]. It is also worth noting that the emission intensity

under the 390 nm, 351nm, and 364 nm is higher than that under 298 nm, 326 nm 427 nm, and 454 nm. In addition, the emission peaks positions do not change as the excitation wavelength is varied.

Also, the emission peak at 482 nm started to vanish as the excitation wavelength was adjusted to 427 and 454 nm, and only a shoulder at 492 nm was observed on the left hand side of the spectra. It is well known that exposing a material to some excitation source populates the excited states of such a material. It can therefore be suggested in this case that the states responsible for the 482 nm are not populated at 427 and 454 nm excitation wavelengths, which resulted in the disappearance of the emission peak at 482 nm.

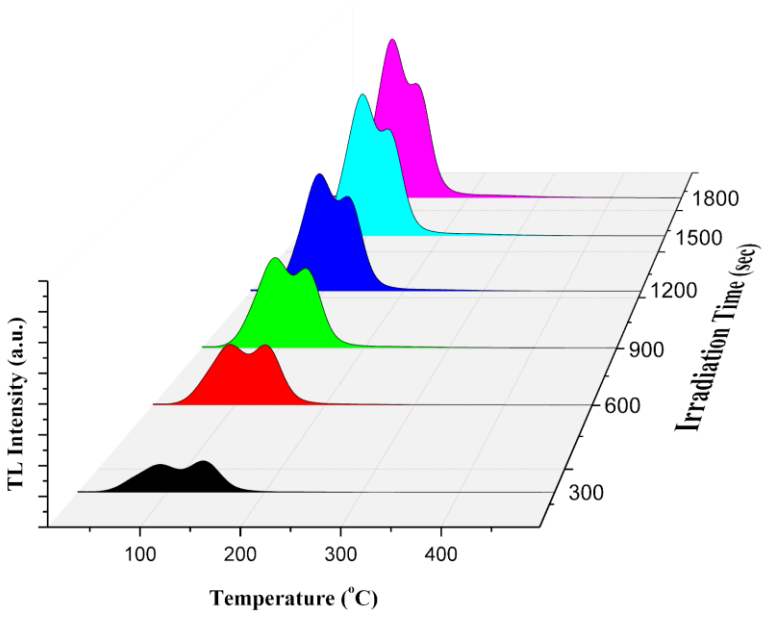

Figure 6.8: Thermoluminescence (TL) curves of $BaAl_2O_4:Dy^{3+}$ phosphor exposed to 0.1028Gy/sec of beta particles irradiation.

To study the effects of irradiation dose on TL glow curve, $BaAl_2O_4:Dy^{3+}$ phosphor was chosen and the glow curves are shown in Figure 6.8. The TL glow curves were recorded at a linear heating rate of $3^oC/s$ after exposure to various doses in the range 300 to 1800 sec from a beta (β) source (0.1028 Gs/s). Two TL peaks were observed at 94 ^oC and 130 ^oC, and no change in position of these peaks was observed, suggesting that the TL process follows a first order kinetics in the $BaAl_2O_4:Dy^{3+}$ phosphor [12].

Also, a change in the TL glow curve shape was observed as the TL intensities of the two peaks increased linearly with dose. In particular, at low doses (300 sec) the peak at 130 ^oC is higher than that at 94 ^oC. At 600 sec dose the two peaks are almost of the same intensity, and at further higher doses the peak at 94 ^oC seemed to intensify even more and suppress the one at 130 ^oC. An increase in TL intensity as the irradiation dose increased was also observed. This linear response of $BaAl_2O_4:Dy^{3+}$ phosphor to irradiation dose is attributed to the fact that when the irradiation dose is increased, more traps responsible for the observed TL peaks in Figure 6.8 are filled [13].

6.4. Conclusion

The variation of Dy^{3+} ion doping concentration showed no noticeable change on the XRD spectra of the phosphors. The PL spectra showed three emission peaks at 482 nm, 575 nm, and 663 nm and the intensity of these peaks increased with the increase of Dy^{3+} ion doping concentration, while showing weak concentration quenching at 0.3 mol%, 14 mol% and 18 mol%. Also, the band gap of $BaAl_2O_4$ phosphor increased at low doping concentrations and decreased at higher Dy^{3+} ion concentration. The variation of excitation wavelength showed higher intensities where the sample is best excited. That is at the highest excitation peaks. It is therefore possible to adjust the luminescence colour by adjusting the excitation wavelength.

References

1. X. Zhang, Z. Lu, F. Meng, L. Hu, X. Xu, J. Lin, C. Tang, *J. Mater. lett.* **79** (2012) 292-295
2. P. You, G. Yin, X. Chen, B. Yue, Z. Huang, X. Liao, Y. Yao, *J. Opt. Mater.* **33** (2011) 1808-1812
3. B. Tian, B. Chen, Y. Tian, J. Sun, X. Li, J. Zhang, H. Zhong, *J. Phys. Chem. Solids.* **73** (2012) 1314-1319
4. Rodrigues, et al., Physica B (2013), http://dx.doi.org/10.1016/j.physb.2013.11.007
5. S.P Puppalwar, S.J Dhoble, A. Kumar, *Ind. j. Pure. App. Phys*. **49** (2011), 239-244
6. B.G. Yacobi, D.B. Holt, Cathodoluminescence Microscopy of Inorganic Solids, Springer, 1990, pp 21
7. E Muhammad Abdul Jamal, D Sakthi Kumar and M R Anantharaman, Bull. Matter. Sci, (2011), pp. 251-259
8. Proceedings of 142nd Annual Meeting & Exhibition, The Minerals, Metals & minerals, 2013, pp. 90-91
9. S. Mondal, S. R. Bhattacharyya and P Mitra, *J. Phys. Ind. Academ. Scie.* **80** (2013) 315-326
10. S. Dhar, Proceedings of the International Conference on Computers and Devices for Communication, Allied Publishers, 1998, pp 494
11. W. Zhao, S. An, B. Fan, S. Li, Y. Dai, *J. lumen.* **132** (2012) 953-956
12. C. M. Sunta, Unraveling Thermoluminescence, Springer, 2014, pp 100
13. B. Ildusovich Kharisov, O. V. Kharissova, U. O. Mendez, Radiation Synthesis of Materials and Compounds, CRC Press, 2013, pp 159

CHAPTER 7

Synthesis and characterization of $CaAl_2O_4$: $Eu^{2+}_{0.01}$, $Dy^{3+}_{0.02}$; $Ca_{1-x}Ba_xAl_2O_4$: $Eu^{2+}_{0.01}$, $Dy^{3+}_{0.02}$; $Ca_{1-x}Mg_xAl_2O_4$: $Eu^{2+}_{0.01}$, $Dy^{3+}_{0.02}$; and $Ca_{1-x}Sr_xAl_2O_4$: $Eu^{2+}_{0.01}$, $Dy^{3+}_{0.02}$ phosphors

7.1. Introduction

Rare earth activated alkaline earth aluminate MAl_2O_4 (M = Ba, Sr, Mg etc.) materials are getting more attention due to their efficient luminescence properties [1]. For instance when these materials are doped with Eu^{2+} ion, they tend to exhibit blue to red emission with high quantum efficiency when excited with UV light [1]. Moreover, the emission of the Eu^{2+} ion from the $4f^6 5d^1 \rightarrow 4f^7$ transition has also gained a lot of interest due to its tuneability from the UV region to the red region of the electromagnetic spectrum [2].

The 5d level in Eu^{2+} can be affected by the environment or the host because the d orbitals will experience the crystal field effects more than the inner 4f orbitals. Therefore the change in the composition of cation or type of the matrix will affect the properties of the phosphors because the crystal field has changed [3]. Furthermore Wu et al. [3] have reported that the photoluminescence properties of the phosphors are influenced by changing the ratios of the cations in the host lattice.

In this chapter, $Ca_{1-x}M_xAl_2O_4 : Eu^{2+}_{0.01}, Dy^{3+}_{0.02}$ (x = 0.3, M = Ba^{2+}, Mg^{2+}, and Sr^{2+}) phosphors are reported and the influence of Ba, Mg, and Sr cations substituting Ca in the host lattice on luminescence properties of $CaAl_2O_4 : Eu^{2+}, Dy^{3+}$ is studied. Furthermore, to investigate how they will affect the crystalline structure and the photoluminescence properties of these materials.

7.2. Experimental procedure

7.2.1 Synthesis

Various compositions of phosphor powders $Ca_{(1-x)}M_xAlO_4 : Eu^{2+}_{0.01}, Dy^{3+}_{0.02} = (x = 0.3, M = Sr, Mg, Ba)$ were prepared by combustion method at an initiating temperature of 600 ^oC. The following precursors: $Ba(NO_3)_3.4H_2O$), $(Sr(NO_3)_3.4H_2O)$, $Mg(NO_3)_3.4H_2O$), $(Al(NO_3)_2.9H_2O)$, $(Eu(NO_3)_3.6H_2O)$, $(Dy(NO_3)_3.5H_2O)$ and urea $(CO(NH_2)_2)$ all in analytical purity were weighed according to the stoichiometry. The precursors were mixed and milled in a mortar using a pestle, and a thick white paste was formed from water of crystallization present in metal nitrates.

All the samples were introduced into a muffle furnace kept 600 ^oC and the entire combustion process was completed in less than 5 minutes.

7.2.2 Characterization

$Ca_{0.95}Al_2O_4 : Eu^{2+}_{0.01}, Dy^{3+}_{0.02}$ and $Ca_{(1-x)}M_xAl_2O_4 : Eu^{2+}_{0.01}, Dy^{3+}_{0.02}$ (x = 0.3, M = Ba^{2+}, Mg^{2+}, and Sr^{2+}) phosphor samples were prepared by combustion method. The X-ray diffraction (XRD) patterns of the samples were performed using X-ray diffraction (XRD, Rigaku SmartLab) using Cu Kα radiation.

The particle morphologies of the powders were investigated using a JEOL JSM-7500F field-emission scanning electron microscope (FE-SEM). The UV-Vis absorption spectra were recorded using Perkin-Elmer Lambda 750s UV-Vis spectrometer. The photoluminescence (PL) spectra were recorded at room temperature using a Jobin Yvon/SPEX FluoroLog spectrofluorometer (Model FL-1057) equipped with a 450 W Xenon light source, double excitation and emission monochromators, and R928 PMT detector.

7.3. Results and Discussions

7.3.1 Structural properties

Figure 7.1 shows the XRD patterns of $Ca_{0.97}Al_2O_4:Eu^{2+}_{0.01},Dy^{3+}_{0.02}$ and $Ca_{(1-x)}M_xAl_2O_4:Eu^{2+}_{0.01},Dy^{3+}_{0.02}$ (M = Ba^{2+}, Mg^{2+}, and Sr^{2+}, x = 0.3) phosphor samples. The XRD patterns in Figure 7.1 (a) to (d) confirm the predominance of typical diffraction peaks of the monoclinic phase structure of $CaAl_2O_4$ according to the JCPDS card no. 23-1036. Diffraction peaks which are marked with a hash (#) are associated to small amount of $CaAl_4O_7$ impurity phase that coexisted with the monoclinic phase in these materials [4,5].

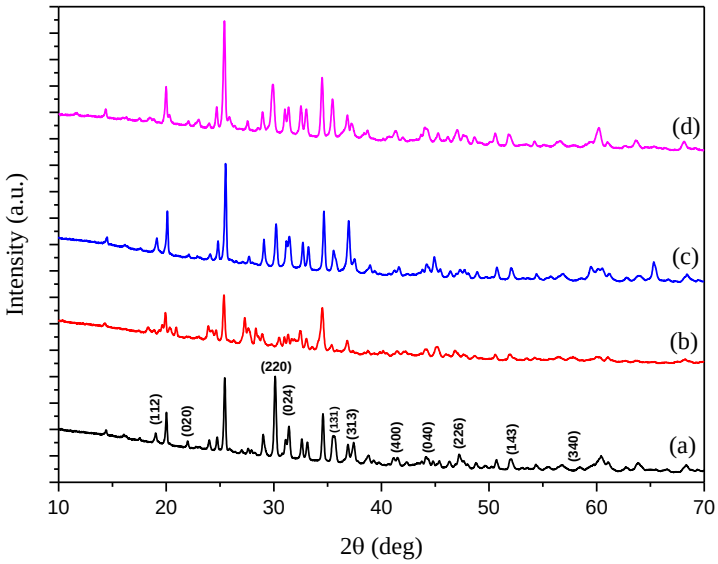

Figure 7.1: Powder X-ray Diffraction patterns (XRD) of (a): $Ca_{0.95}Al_2O_4:Eu^{2+}_{0.01},Dy^{3+}_{0.02}$; (b) $(Ca_{(1-x)}Ba_{0.3})_{0.97}Al_2O_4:Eu^{2+}_{0.01},Dy^{3+}_{0.02}$; (c): $(Ca_{(1-x)}Mg_{0.3})_{0.97}Al_2O_4:Eu^{2+}_{0.01},Dy^{3+}_{0.02}$ and (d): $(Ca_{(1-x)}Sr_{0.3})_{0.97}Al_2O_4:Eu^{2+}_{0.01},Dy^{3+}_{0.02}$ phosphors.

No other phases were detected that could be associated with the substitution of Ca^{2+} by the alkaline earth ions Ba^{2+}, Mg^{2+} and Sr^{2+} in the $CaAl_2O_4$ lattice. Also, a drop in intensity was observed in the Ba^{2+} substituted sample which suggests less crystallinity in this sample. Small shifts of diffraction peaks were also observed. These shifts are attributed to changes in the $CaAl_2O_4$ lattice due to the introduction of alkaline earths of different ionic radii into the lattice. When a large ion Ba^{2+} (radius = 0.134 nm) substitutes a small ion Ca^{2+} (radius = 0.106), lattice expansion occurs which results in a shift of diffraction peaks to lower 2θ angles. Due to the same reason, Sr^{2+} (0.127 nm) substitution also shifts diffraction peaks to the lower angles. On the contrary, substitution of Ca^{2+} by a small ion Mg^{2+} (radius = 0.078 nm) induces a lattice shrinkage and hence a shift of the peaks to higher 2θ angles in this sample.

The average particle sizes D of these four phosphors were estimated using the Scherer's equation 7.1 and their values are tabulated in table 7.1.

$$D = \frac{K\lambda}{\beta Cos\theta} \qquad (7.1)$$

K is a constant (0.9), λ is the X-ray wavelength (0.15405 nm), β is the full width at half maximum (FWHM), and θ is the diffraction angle of the observed diffraction peaks.

Table 7.1: Estimated values of the particle size D of the as-synthesized phosphors

Phosphors	**$CaAl_2O_4:Eu^{2+},Dy^{3+}$**	**$CaBaAl_2O_4:Eu^{2+},Dy^{3+}$**	**$CaMgAl_2O_4:Eu^{2+},Dy^{3+}$**	**$CaSrAl_2O_4:Eu^{2+},Dy^{3+}$**
D(nm)	35.80	16.90	32.30	27.70

Figure 7.2 shows the SEM surface morphology of $CaAl_2O_4:Eu^{2+}_{0.01},Dy^{3+}_{0.02}$ and the $Ca_{1-x}M_xAl_2O_4:Eu^{2+}$, Dy^{3+} (x = 0.3, M = Ba^{2+}, Mg^{2+}, and Sr^{2+}) powder samples. The images in Figure 7.2 were taken at a magnification of X50000. The images reveal the surfaces with voids and pores which are due to the escaping gases during the combustion process. It is noticed that the size as well as the shapes of the powders are not uniform, which may be a result of a varying distribution of temperature and mass flow during the combustion process [6].

7.3.2 Surface morphology

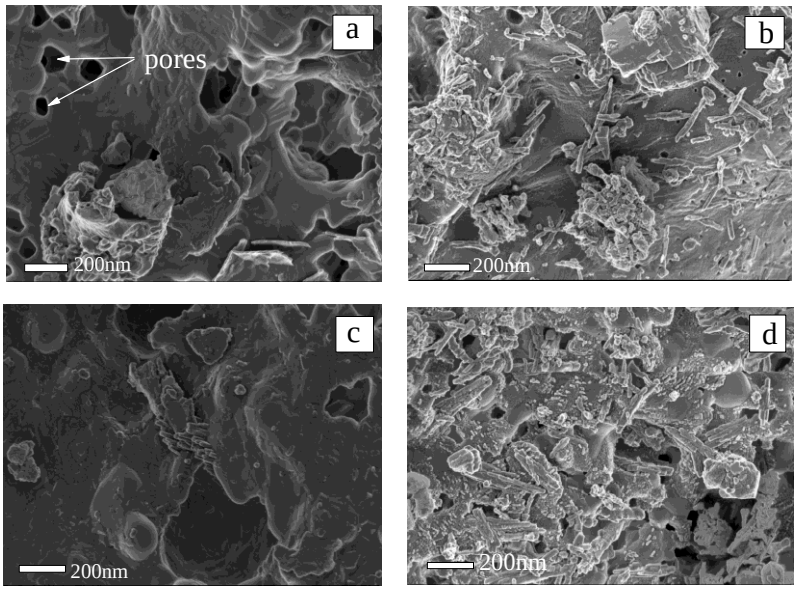

Figure 7.2: Scanning electron microscope (SEM) images of (a): $CaAl_2O_4:Eu^{2+}_{0.01},Dy^{3+}_{0.02}$, (b): $(Ca_{(1-x)}Ba_{x=0.3})_{0.97}Al_2O_4:Eu^{2+}_{0.01},Dy^{3+}_{0.02}$ (c): $(Ca_{(1-x)}Mg_{x=0.3})_{0.97}Al_2O_4:Eu^{2+}_{0.01},Dy^{3+}_{0.02}$ and (d): $(Ca_{(1-x)}Sr_{x=0.3})_{0.97}Al_2O_4:Eu^{2+}_{0.01},Dy^{3+}_{0.02}$ phosphors.

Energy dispersive spectroscopy technique was used to perform the elemental analysis of the $(Ca_{(1-x)}Ba_{x=0.3})_{0.97}Al_2O_4:Eu^{2+}_{0.01},Dy^{3+}_{0.02}$ phosphor. The EDS spectrum and elemental maps are shown in Figure 7.3. It was found that the EDS spectrum consists of peaks associated to Ca, Ba, Al, O, Eu, and Dy, which is a clear confirmation of these elements in the as-prepared $(Ca_{(1-x)}Ba_{x=0.3})_{0.97}Al_2O_4:Eu^{2+}_{0.01},Dy^{3+}_{0.02}$ phosphor. The peaks associated with the dopants (Eu^{2+} and Dy^{3+}) are less intense than those associated with the other elements, and this is attributed to very low concentrations of dopants in $(Ca_{(1-x)}Ba_{x=0.3})_{0.97}Al_2O_4:Eu^{2+}_{0.01},Dy^{3+}_{0.02}$ the phosphor. The mapping shows that all these elements in the $(Ca_{(1-x)}Ba_{x=0.3})_{0.97}Al_2O_4:Eu^{2+}_{0.01},Dy^{3+}_{0.02}$ phosphor are uniformly distributed. The additional peak associated with Au is due to coating of the sample and that of C appears due to carbon tape used as a substrate. The insert in the figure shows the SEM image of the area that was used to conduct the elemental analysis.

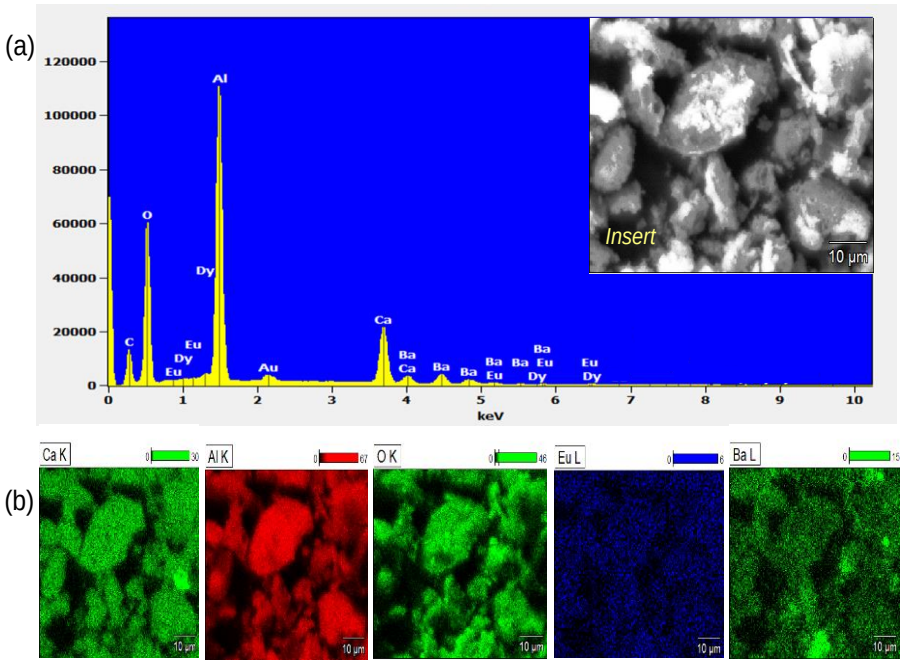

Figure 7.3(a): Scanning electron microscopy (SEM) image and Energy dispersive spectroscopy (EDS) spectrum, (b): Energy dispersive spectroscopy mapping of the as-prepared $(Ca_{(1-x)}Ba_{x=0.3})_{0.97}Al_2O_4:Eu^{2+}{}_{0.01},Dy^{3+}{}_{0.02}$ phosphor.

Figure 7.4 shows the SEM image, EDS spectrum, and EDS mapping used for elemental analysis of the as-prepared $(Ca_{(1-x)}Mg_{x=0.3})_{0.97}Al_2O_4:Eu^{2+}{}_{0.01},Dy^{3+}{}_{0.02}$ phosphor. The EDS spectrum confirms the presence of Ca, Mg, Al, O, Eu, and Dy in the as-prepared $(Ca_{(1-x)}Mg_{x=0.3})_{0.97}Al_2O_4:Eu^{2+}{}_{0.01},Dy^{3+}{}_{0.02}$ phosphor. Also, the mapping shows that all these elements in the $(Ca_{(1-x)}Mg_{x=0.3})_{0.97}Al_2O_4:Eu^{2+}{}_{0.01},Dy^{3+}{}_{0.02}$ phosphor are uniformly distributed. The additional peak associated with Au is due to coating of the sample and that of C appears due to carbon tape used a substrate. The insert in the figure shows a SEM image of the area that was used to conduct the elemental analysis.

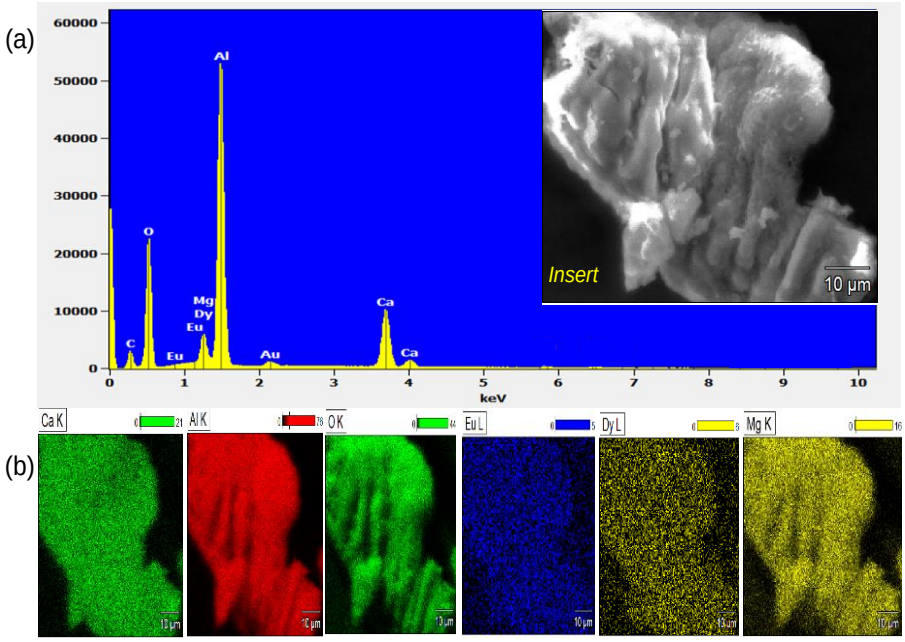

Figure 7.4: SEM image and EDS spectrum (a), EDS elemental mapping (b) of the as-prepared $(Ca_{(1-x)}Mg_{0.3})_{0.97}Al_2O_4:Eu^{2+}{}_{0.01},Dy^{3+}{}_{0.02}$ phosphor.

Figure 7.5 presents the elemental analysis of the as-prepared $(Ca_{(1-x)}Sr_{0.3})_{0.97}Al_2O_4:Eu^{2+}{}_{0.01},Dy^{3+}{}_{0.02}$ phosphor. The EDS spectrum confirms the presence of Ca, Sr, Al, O, Eu and Dy in the as prepared $(Ca_{(1-x)}Sr_{x=0.3})_{0.97}Al_2O_4:Eu^{2+}{}_{0.01},Dy^{3+}{}_{0.02}$ phosphor. Also, the mapping proves a uniform distribution of all these elements in the $(Ca_{(1-x)}Sr_{x=0.3})_{0.97}Al_2O_4:Eu^{2+}{}_{0.01},Dy^{3+}{}_{0.02}$ phosphor. The insert in the figure shows a SEM image of the area that was used to conduct the elemental analysis.

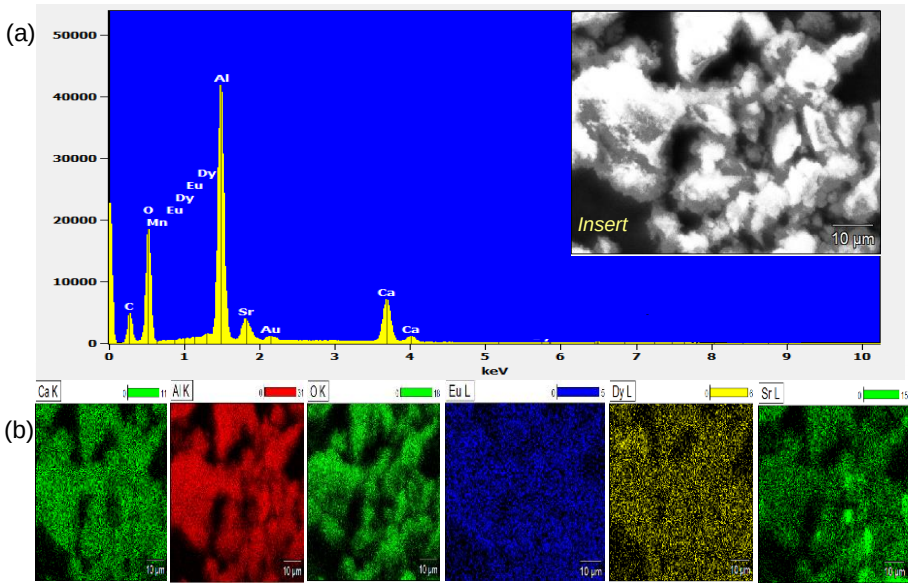

Figure 7.5:SEM image, EDS spectrum, and EDS mapping of $(Ca_{(1-x)}Sr_{0.3})_{0.97}Al_2O_4:Eu^{2+}{}_{0.01},Dy^{3+}{}_{0.02}$ phosphor.

7.3.3 Luminescent Properties

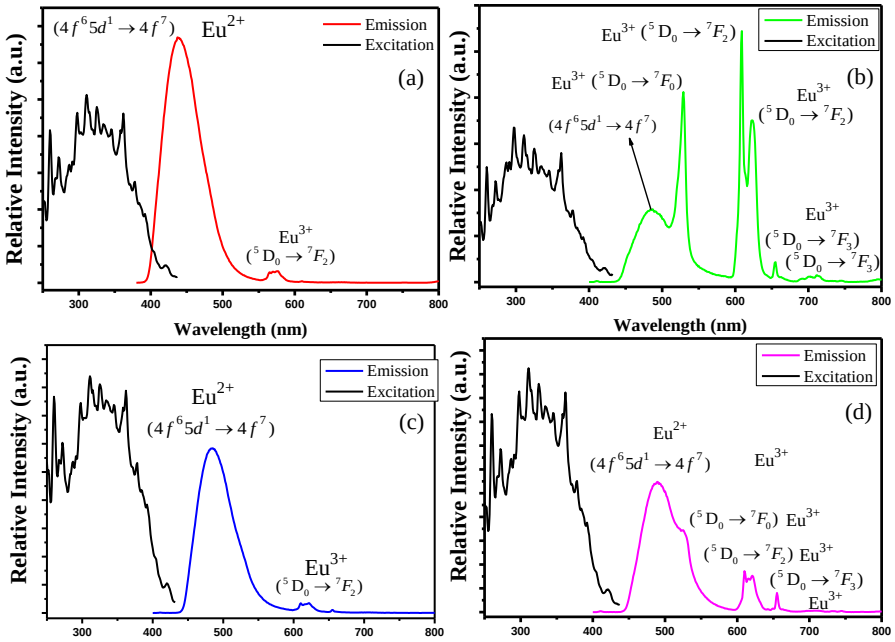

Figure7.6: Photoluminescence properties of (a): $CaAl_2O_4:Eu^{2+}{}_{0.01},Dy^{3+}{}_{0.02}$ (b): $(Ca_{(1-x)}Ba_{x=0.3})_{0.97}Al_2O_4:Eu^{2+}{}_{0.01},Dy^{3+}{}_{0.02}$,(c) $(Ca_{(1-x)}Sr_{x=0.3})_{0.97}Al_2O_4:Eu^{2+}{}_{0.01},Dy^{3+}{}_{0.02}$ and (d) $(Ca_{(1-x)}Mg_{x=0.3})_{0.97}Al_2O_4:Eu^{2+}{}_{0.01},Dy^{3+}{}_{0.02}$ phosphors under 364 nm excitation.

The effects of Ca^{2+} substitution by Ba^{2+}, Mg^{2+}, and Sr^{2+} ions on photoluminescence were studied. Each sample was excited using the xenon lamb at 364 nm to obtain the emission spectra shown in Figure 7.6. The excitation spectra of the unsubstituted, Ba^{2+} substituted, Sr^{2+} substituted, and Mg^{2+} substituted samples were monitored at their respective observed emission wavelengths, namely 436 nm, 485 nm, 490 nm, and 487 nm respectively. All these broad emission bands observed are common and are assigned to the $4f^65d^1 \rightarrow 4f^7$ transition of the Eu^{2+} ion [2].

A change in position of these emission peaks is ascribed to the alteration of the $CaAl_2O_4:Eu^{2+}{}_{0.01},Dy^{3+}{}_{0.02}$ structure by the introduction of Ba^{2+}, Sr^{2+}, and Mg^{2+} ions. The $4f^65d^1 \rightarrow 4f^7$ transition of the Eu^{2+} ion is generally known to be sensitive to the crystal field of the ions surrounding it, therefore Ca^{2+} substitution by Ba^{2+}, Sr^{2+}, and Mg^{2+} ions modifies the

crystal field in the parent host matrix ($CaAl_2O_4$) and consequently introduces the change in emission peak positions [7]. In other words, change of the emission peak position observed in Figure 7.6 due to Ca^{2+} ion substitution is attributed to the change in crystal filed induced by the substituting ions. The sharp emission lines due to the 4f-4f transitions of the Eu^{3+} ion were also observed as shown in Figure 7.6. The presence of Eu^{3+} ion suggest that the reducing atmosphere created during the combustion process by urea was not sufficient to convert it to Eu^{2+} ions in these samples.

A change in shape of the emission spectra was also observed as the substituting ions (Ba^{2+}, Mg^{2+}, and Sr^{2+}) occupied the place of the Ca^{2+} ions in the lattice, and this change may be due to the change in the extend of crystal lattice distortion as the substitutions took place. In this case, three different alkaline earth ions of different ionic radii (Ba^{2+} = 0.134 nm, Mg^{2+} = 0.078 nm, and Sr^{2+} = 0.127 nm) [8] are separately introduced in the same crystal lattice ($CaAl_2O_4 : Eu^{2+}, Dy^{3+}$), so different degrees of this lattice distortion is expected and therefore different optical properties should be expected [9].

Specifically, the Eu^{3+} emission peaks are more intense in the Ba^{2+} substituted sample, weak in the Mg^{2+} substituted sample, and even weaker in the Sr^{2+} substituted sample. This may be a result of Ba^{2+} ions inducing a more distortion (expansion) on the crystal lattice when they substitute the Ca^{2+} (radius = 0.106) [8] owing to its largest size compared to the Mg^{2+} and Sr^{2+} ions. Furthermore, because all the observed Eu^{3+} emission peaks are due to forbidden transitions according to the selection rule $\Delta J = 0$ [11], the Judd-Ofelt theory [12], suggests that the $(Ca_{(1-x)}Ba_{x=0.3})_{0.97}Al_2O_4 : Eu^{2+}{}_{0.01}, Dy^{3+}{}_{0.02}$ phosphor has a more distorted (lack inversion center) crystal lattice than the other two samples such that the 4f-4f forbidden transitions of the Eu^{3+} ion become more allowed and more intensified in this sample.

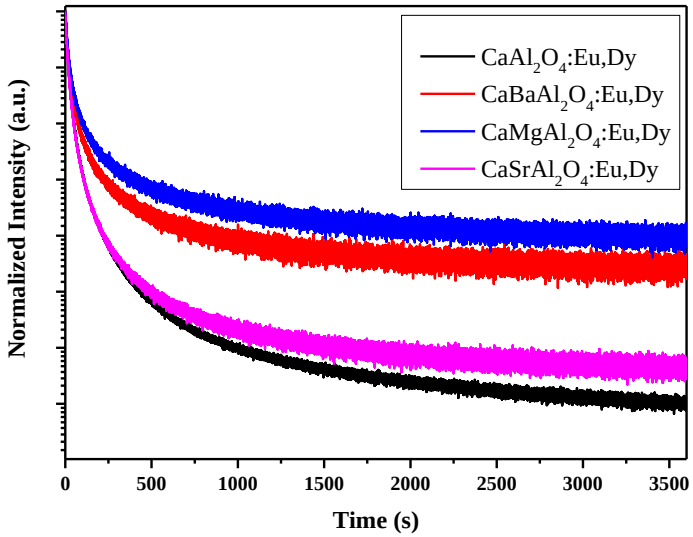

Figure 7.7: Decay curves of the as-prepared phosphors after 364 nm excitation.

The decay curves were recorded after irradiating the samples with the continuous xenon lamp at room temperature for 5 minutes at 364 nm, and the decay curves are shown in Figure 7.7. It can be seen that the four samples first show a rapid decay, followed by longer lasting phosphorescence. The rapid decay shown in all four samples can be associated with the intrinsic luminescence lifetime of the Eu^{2+} ion [13], and the longer lasting decays are associated with Dy^{3+} ion playing a hole trapping role in these materials [13], owing to the formation of hole trapping levels within the forbidden gap of the host after co-doping with Dy^{3+}. After excitation has stopped, recombination of trapped holes in these levels with previously excited electrons is slow and this is known to prolong the luminescence time of these phosphors [14]. The decay times of all the phosphors were found by fitting the decay curves in Figure 7.7 with a third order exponential equation and their values are shown in table 7.2.

Table 7.2: Decay parameters of the as-synthesized phosphors.

Phosphors	τ_1(s)	τ_2(s)	τ_3(s)
$CaAl_2O_4$: $Eu^{2+}_{0.01}$, $Dy^{3+}_{0.02}$	11.229	36.650	228.627
$Ca_{1-x}Ba_xAl_2O_4$: $Eu^{2+}_{0.01}$, $Dy^{3+}_{0.02}$	55.595	11.705	414.792
$Ca_{1-x}Mg_xAl_2O_4$: $Eu^{2+}_{0.01}$, $Dy^{3+}_{0.02}$	67.768	12.881	532.090
$Ca_{1-x}Sr_xAl_2O_4$: $Eu^{2+}_{0.01}$, $Dy^{3+}_{0.02}$	9.964	37.751	230.579

It is worth noting that the $Ca_{1-x}Mg_xAl_2O_4$: $Eu^{2+}_{0.01}$, $Dy^{3+}_{0.02}$ phosphor has a longer decay time, followed by $Ca_{1-x}Ba_xAl_2O_4$: $Eu^{2+}_{0.01}$, $Dy^{3+}_{0.02}$; $Ca_{1-x}Sr_xAl_2O_4$: $Eu^{2+}_{0.01}$, $Dy^{3+}_{0.02}$; and lastly the $CaAl_2O_4$: $Eu^{2+}_{0.01}$, $Dy^{3+}_{0.02}$ phosphor with the shortest decay time. Longer afterglows are generally associated with trap levels situated at depths where thermal release of trapped electrons at room temperature is dominant during luminescence process [15]. Now, because in the above phosphors Eu^{2+} is the luminescence center, while Dy^{3+} forms the trapping levels in the crystal lattices with different distortions [15], it is therefore expected that Dy^{3+} forms trap levels at different depths in crystal lattices with different distortions. From this, it can be deduced that the Dy^{3+} ion forms traps at appropriate levels that favors longer lasting luminescence in the $Ca_{1-x}Mg_xAl_2O_4$: $Eu^{2+}_{0.01}$, $Dy^{3+}_{0.02}$ phosphor than the other phosphors as shown in table 7.2.

7.4. Conclusion

All the emission spectra showed a broad blue-green emission that is attributed to the $4f^6 5d^1 \rightarrow 4f^7$ transition of the Eu^{2+} ion. The emission spectra also showed emission peaks of the 4f-4f transition of the Eu^{3+} ion. These peaks were more intense in the Ba^{2+} substituted sample, suggesting that the Eu^{3+} transitions are more allowed in this sample due to more local distortion than in other samples. The $Ca_{1-x}Mg_xAl_2O_4$: $Eu^{2+}_{0.01}$, $Dy^{3+}_{0.02}$ sample showed a longer afterglow than other samples and un-substituted sample showed the shortest decay time.

References

1. T. Wanjun, C. Donghua, W. Ming, *J. Opt. laser Techn.* **41** (2009) 81-84
2. H. Ryu, J.B. Lee, K.S. Bartwal, *Physica B*, Elsevier, (2008), 3822-3825
3. H. Wu, Y. Hun, B. Zeng, Z. Mou, L. Deng, *J. Phys. Chem. Solids.* **72** (2011) 1284-1289.
4. H. N. Luitel, T. Watari, R. Chand, T. Torikai, M. Yada, H. Mizukami, *J. Mater. Scie. Eng B.* **178** (2013) 834-842
5. S. K. Sharma, M. M. Malik, *J. Mater. lett.* **65** (2011), 1451-1453
6. B.M. Mothudi, O.M. Ntwaeaborwa, S. S. Pitale, H.C. Swart, *J. Alloys. Compd*. **508** (2010) 262-265
7. A. G. Baca, J. Brown, D. N. Buckley, P. Nam, C. O'Dwyer, A. Etcheberry, State-of-the-Art Program on Compound Semiconductors 50 (SOTAPOCS 50) -and- Processes at the Semiconductor Solution Interface 3, Electrochemical Society, 2009, pp 161
8. http://www.rsc.org/chemsoc/visualelements/pages/data/intro_groupii_data.html, 20 Feb 2014
9. R. Subasri, D. Matusch, H. Nafe, F. Aldinger, *J. Europ. Ceram. Society*. **24** (2004) 129–137
10. R. C. Ropp, Luminescence and The Solid State, 2nd edition, Elsevier, 2004, pp416
11. F. Clabau , A. Garcia, P. Bonville, D. Gonbeau, T. Le Mercier, P. Deniard, S. Jobic, *J. Solid State. Chem.***181** (2008) 1456-1461
12. TMS 142nd Annual Meeting and Exhibition Proceedings, John Wiley & Sons, New Jersey, 2013, pp121-122
13. Q. Xiao,L. Xiao,Y. Liu , X. Chen,Y. Li, *J. Phys. Chem. Solids.* **71** (2010) 1026-1030
14. P. Zhang, M. Xu, Z. Zheng, B. Sun, Y. Zhang, *J. Mater. Scie. Eng. B.* **136** (2007) 159-164
15. Y. Lin, C. Nan, X. Zhou, J. Wu, H. Wang, D. Chen, S. Xu, *J. Mater. Chem. Phys.* **82** (2003) 860-863

CHAPTER 8

Conclusions

The $SrAl_2O_4:Eu^{2+}$; $SrAl_2O_4:Dy^{3+}$; $SrAl_2O_4:Mn^{2+}$; $SrAl_2O_4:Eu^{2+}$, Dy^{3+}; $SrAl_2O_4:Eu^{2+}$, Mn^{2+}; $SrAl_2O_4:Dy^{3+}$, Mn^{2+}; and $SrAl_2O_4:Eu^{2+},Mn^{2+}$, Dy^{3+} powder phosphors were successfully synthesized by combustion method, and their PL properties were studied. It was found that the $SrAl_2O_4:Eu^{2+}$ sample had a broad emission at 500 nm which evidents that urea used during combustion successfully reduced Eu^{3+} into Eu^{2+} although there is still some fraction of Eu^{3+} still present in the sample. Also the decay analysis were also cried out and $SrAl_2O_4:Eu^{2+}$, Dy^{3+} and $SrAl_2O_4:Eu^{2+},Mn^{2+}$, Dy^{3+} showed longer afterglow with $SrAl_2O_4:Eu^{2+},Mn^{2+}$, Dy^{3+} phosphor showing the longest afterglow. The longest afterglow in the $SrAl_2O_4:Eu^{2+},Mn^{2+}$, Dy^{3+} phosphor was atributed to the incorporation of the Mn^{2+} ion into the phosphor and the mechanism was discussed.

PL of Eu^{2+}, Dy^{3+}, and Mn^{2+} ions in different host matrices were also studied, and Eu^{3+} emission from the hypersensitive transition was found to be more intense in $BaAl_2O_4$ than in Sr_2O_4 matrix, proving a low symmetry in $BaAl_2O_4$ compared to $SrAl_2O_4$. The Mn^{2+} ion was found to have two emissions in the $SrAl_2O_4$ host matrix and only one emmission in the $BaAl_2O_4$ host matrix, showing the Mn^{2+} optical properties to be sensitive to the surrounding environment.

PL intensity properties of the $BaAl_2O_4:Dy^{3+}$ phosphor at varying of Dy^{3+} doping concentrations was also studied. The three emission peaks at 482 nm, 575 nm, and 663 nm were observed for all concentrations. Also, the PL intensity was found to be dropping at 0.5 mol%, 16 mol%, and 20 mol% showing concentration quenching at these points. The band gap behavior of the $BaAl_2O_4:Dy^{3+}$ phosphor was also studied at varying concentrations of Dy^{3+}. It was found that

the band gap first decrease at low doping concentrations, and then increase at at higher doping concentrations, and this increase in band gap at higher doping concentrations of Dy^{3+} was explained using the Burstein-moss shift.

PL intensity of the $BaAl_2O_4:Dy^{3+}$ phosphor due to different excitation wavelengths was also studied. The highest emission intensity was found when the $BaAl_2O_4:Dy^{3+}$ phosphor was excited with the highest excitation peak i.e. 390 nm on the excitation spectrum of this sample, and the lowest emission intensity was found when the sample was excited with lowest excitation on the excitation spectrum i.e. 427 nm.

PL of the $Ca_{1-x}M_{0.3}Al_2O_4:Eu^{2+}$, Dy^{3+} (M = Ba^{2+}, Mg^{2+}, and Sr^{2+}) powder samples was also studied as the alkaline earth ions Ba^{2+}, Mg^{2+}, and Sr^{2+} replaced the Ca^{2+} ion. It was found that all the samples exhibited a blue-green emission from the Eu^{2+} ion but with different shapes showing that the Eu^{2+} ion is sensitive to the environment surrounding it. However, there were also emissions from the Eu^{3+} ion present in the samples, and these emissions were found to be more pronounced in the Ba^{2+} substituted sample. In other words the forbidden 4f-4f transitions were found to be more allowed in the Ba^{2+} substituted sample than all other samples. This behavior was according to Judd-Ofelt theory ascribed to the lack of symmetry in this sample compared to the others.

The decay analysis was also carried out, and it was found that the $CaAl_2O_4:Eu^{2+}$, Dy^{3+}sample had the shortest afterglow than all other samples.

Conferences

- Manaka M.C, B.M Mothudi, O.M.Ntwaeaborwa, A. Kumar, K. Sohn , H.C. Swart, Phosphorescence and thermoluminescence properties of $CaAl_2O_4:Eu^{2+}$, Dy^{3+} phosphors prepared by solid state reaction method. The 57th Annual Conference of the South African Institute of Physics (SAIP), hosted by the University of Pretoria. 2012
- Manaka M.C, Dhlamini M.S, Mothudi B.M, The Synthesis And Characterization of $SrAl_2O_4:Eu^{2+}$; $SrAl_2O_4: Dy^{3+}$; $SrAl_2O_4:Mn^{2+}$; $SrAl_2O_4: Eu^{2+}$, Dy^{3+} Phosphors Prepared by Combustion Method. The 58^{th} Annual Conference of the South African Institute of Physics (SAIP) by the University of Zululand 2013